Process-Induced Defects

in

Semiconductor Silicon

A thesis submitted to the University of Manchester Institute of Science and Technology for the degree of Doctor of Philosophy, 1996

By Jianqing Wen

Department of Electrical Engineering & Electronics

University of Manchester Institute of Science and Technology

Declaration

I declare that no portion of the work referred to in the thesis has been submitted in support of an application for another degree or qualification of this or any other university of other institution of learning

JianqingWen

To my husband, my mother, my sister. And my father in memory.

Acknowledgement

I would like to thank my supervisor Professor A. R. Peaker to whom I am deeply indebted for his encouraging me into this research, for his valuable help and guidance throughout my Ph.D study. His patience during the reviewing of this thesis is also greatly appreciated.

Special thanks must go to Dr. J. H. Evans for her continuing advice, support and inspiring discussions throughout my study.

I would like to thank my cooperators Dr. J. P. Zhang, Mr. F. Cristiano and Professor P. L. F. Hemment from University of Surrey for the Ion implantation, Rutherford Backscattering Spectrometry (RBS) measurements of samples studied in chapters 4 and 5, the Cross-sectional Transmission Electron Microspectroscopy (XTEM) and Secondary Ion Mass Spectroscopy (SIMS) measurements of samples studied in chapter 5, and their enthusiasm discussions and friendship throughout my study. I would also like to thank Dr. C. D. Marsh from Oxford University for the Transmission Electron Microspectroscopy (XTEM) measurements of samples studied in chapter 4.

Thanks must also go to Mr. J. H. Kay from GEC Plessey Semiconductors for providing me with samples studied in chapter 6, for the Open Circuit Voltage Decay (OCVD) lifetime measurements of those samples, and for the stimulating discussions throughout this project to solve production problems. Cascade Scientific is acknowledged for the Microwave Photoconductive Decay (μPCD) lifetime measurements of those samples.

I am very grateful to all the staff and students at Solid State Electronics group of the Department of Electrical Engineering and Electronics at UMIST for their stimulating discussions and friendship throughout my study. In particular, I would like to thank I. Hawkins, H. Efeoğlu, W. S. Truscott, M. R. Brozel, K. E. Singer, H. D. McKell, R. Wing, H. Coulson, S. O'Hagan, J. Davidson, C. H. Lin, M. F. McGowan, J. Gilmore, and all those I have come into contact with over the years.

I am greatly indebted to the Science and Engineering Research Council (UK) and GEC Plessey Semiconductors (UK) which have provided financial support to my study.

Very special thanks must go to my husband for his constant love, interest and support.

Abstract

This thesis describes a study of process-induced defects in silicon. Three processes have been studied in detail: Ge^+ preamorphisation (for shallow junction formation); high dose Ge^+ implantation (for SiGe alloy formation); and specific stages in silicon power device fabrication.

Deep states with activation energies of electron emission of 440 meV and 506 meV in Ge^+ preamorphised and annealed n-type Si have been correlated with the evolution of the end of range defects. These states have been found to be responsible for the excess donor concentrations and the high reverse leakage currents in device structures. An annealing study of these structures showed that 800°C was a crucial temperature in relation to the removal of the electrically active implant damage and hence the quality of the materials.

In the case of very high dose Ge^+ implantation to make SiGe alloys the effect of an additional carbon pre-implantation or an additional silicon post-amorphisation on the relaxation mechanism in SiGe alloys were studied. Strain reduction via defects can explain the improved quality of the SiGe alloys produced from these methods.

In the case of the power device study, deep states with activation energies of electron emission of 275 meV and 542 meV were detected and correlated to an abnormal short lifetime in power p-i-n diode materials and very high leakage currents/ short lifetimes in thyristor materials/structures respectively. Their origin and formation mechanism were investigated via a study of the effect of thermal cycles on neutron transmutation doped silicon materials and conventional doped float zone materials.

Table of Contents

List of Symbols

a	interatomic spacing
A	junction area
C	capacitance
C_i	interstitial carbon atom
C_s	substitutional carbon atom
C_s	solid solubility
c_n	electron capture cross section
c_p	hole capture cross section
d	sample thickness
D:	diffusivity
E	electron energy
E_s	heat of solution
E_c	conduction band edge
E_v	valence band edge
e_{maj}	majority carrier trap emission rate
e_{min}	minority carrier trap emission rate
e_n	electron thermal emission rate
e_p	hole thermal emission rate
E_{ex}	binding energy of exciton
E_g	energy of the bandgap
E_F	Fermi level

E_T energy position of deep level

g degeneracy factor

h Planck's constant

h critical thickness

I junction current

I_o junction reverse saturation current

k Boltzmann's constant

$\boldsymbol{k}$ wave vector

L_D Debye length

m^* effective mass

m^* measured lattice mismatch

M mass of implanted ions

N_A shallow acceptor concentration

N_D shallow donor concentration

N_C effective density of states of conduction band

N_V effective density of states of valence band

n electron density

n_o electron density of bulk material

n_m measured electron density

n_T concentration of defects occupied by electrons

N_T total deep level concentration

O_i interstitial oxygen atom

p hole density

p	probability that the state is occupied
p_n	hole concentration in n-type material
p_T	concentration of trapped holes
q	magnitude of electronic charge
Q	electric charge
R	reflectivity
R_P	ion implantation projected range
Si_I	interstitial silicon atom
T	absolute temperature
T	transmittance
T_H	hole trap
T_E	electron trap
t	time
<v>	average thermal velocity
V	applied bias voltage
V_{bi}	built-in voltage
V(r)	static potential
W	width of depletion region
y	cross point of deep level and Fermi level
α	absorption coefficient
β	electromagnetic radiation: emission of high energy electrons
γ	electromagnetic radiation: emission of high energy photons
ε	dielectric constant

θ	angle
λ	transition region
λ	wavelength
σ	carrier capture cross section
τ	time constant
υ:	Poisson ratio
Φ	dose of implanted ions
ω	frequency
$h\upsilon$	photo energy
$\hbar\Omega$:	phonon energy

Chapter 1 Introduction

The potential of crystal defects to cause device failure has been recognized from the beginning of silicon device technology. One of the first reports on correlation between a device property (leakage currents) and the presence of defects (metal precipitates) was published by Goetzberger and Shockley [Goetzberger 60] in 1960. Undesirable defects present in the starting material or introduced anywhere in the manufacturing process leading to device failure are still a major concern for stable yields and for the reliability of semiconductor devices today [Bergholz 91]. For each new generation of integrated circuits (IC), large scale integrated (LSI) circuits, very large scale integrated (VLSI) circuits and ultra large scale integrated (ULSI) circuits, some progress is made, yet the problems have never been completely solved. Meantime the relationship between material properties, device processing and circuit performance has become more pronounced with greater packing density, increased chip size and often the introduction of novel devices [Kolbesen 91]. As a result the susceptibility of devices to defects has increased (for example, the maximum tolerable physical defect size is roughly one order of magnitude lower than the minimum feature size in an integrated circuit [Claeys 91]). In the field of silicon power devices the demand for increases in voltage and current ratings and for more complicated device structures also establish demanding requirements for stringent control of point defects. These factors raise questions about the nature of those defects and the conditions for their formation, evolution and eventually their prevention in device fabrication.

The quality of the incoming silicon material is a crucial factor influencing the development of defects during the manufacturing process. Process-induced defects, normally defined as those generated during device fabrication, also play a crucial role in determining the functionality of devices. They can develop to such an extent that they may dominate the properties of a material or a device, as in the following three processing situations which have been investigated in this thesis.

(1) Defects in Ge^+ preamorphized and annealed silicon.

In order to avoid axial channeling of boron during low-energy ion implantation for the formation of ultrashallow junctions in submicron integrated circuits, a technique is used in which a high dose of group IV atoms (Si, Ge or Sn) is implanted in order to amorphize the silicon substrate surface region prior to dopant implantation. This method can be used to achieve a very high percentage of electrically active dopants. The process of solid phase epitaxy regrowth of the amorphous layer can be achieved by furnace annealing or rapid thermal annealing. Annealing of the amorphous layer can leave behind defects which may deteriorate the properties of the materials or cause undesirable changes of the dopant distribution [Servidori 87][Cowern 94], and, as such, are a cause of device degradation [Brotherton 89]. Understanding the formation of the defects is very limited at the present time. There are three main factors affecting the generation and evolution of these defects which in turn determine the final characteristics of the material. The first factor is related to the ion implantation conditions [Laanab 95]. The second is dependent on the annealing conditions and the third factor is related to the impurities present in the starting materials (e.g. the concentrations of oxygen, carbon and 3d transition metals etc.).

(2) Defects related to silicon-germanium alloys synthesized by Ge^+ ion implantation.

SiGe alloys on silicon substrates have brought Si technology a step towards new age. Many devices have derived great benefit from SiGe-based heterostructures, examples are: double Heterostructure Bipolar Transistors (DHBTs), high performance optical detectors for optical communication (in the 1.3 to 1.5 μm range), high mobility MODFETs [Stoneham 95] etc.. The foundation of modern SiGe strained-layer devices were laid several decades ago [Shockley 48] with concepts which only have been exploited in recent years. The most plausible technique for growing strained layers is Molecular Beam Epitaxy (MBE) [Bean 84]. Several other methods have also been developed among them are Low Temperature Ultra High Vacuum CVD (LT-UHVCVD) [Meyerson 86], low pressure chemical vapor deposition (LPCVD) [Meyerson 88], Chemical Beam Epitaxy [Kramer 92] etc. A possible alternative for the formation of SiGe alloys is ion implantation. It is highly compatible with modern silicon processing and has been shown to be suitable for fabricating SiGe alloys [Hart 81][Paine 90]. But ion implantation of high doses of Ge^+ and subsequent thermal annealing of the alloy introduces a high concentration of defects which could lead to a material with very poor quality that is not usable. The main defects are: strain relief defects introduced when the alloys exceed the critical layer thickness and start to relax [Berti 91], and the end of range (EOR) defects commonly observed in ion implanted and annealed silicon. However, a reduction in the density of these defects and a improvement of the quality of the material has been achieved by using carbon co-implantation [Fukami 90] or a silicon post amorphization [Zhang 94]. We have adapted these two methods and the defects are studied and compared among the three SiGe alloy systems (Ge^+ implant only, C^+ co-implant, Si post amorphization) in order to understand how the relaxation mechanism

via the strain relief defects work in the three situations. The ultimate aim is to develop an optimum condition which is applicable for device fabrication.

(3) Defects related to silicon power devices.

The field of power electronics has experienced a large growth due to many factors including the continuous advances in microelectronics methods and the advances in fabrication technology which have made it possible to significantly improve the voltage and current ratings of power semiconductor devices and to increase their switching speed. In power electronic applications, the power to be converted in a controlled manner ranges from a few watts to several hundred megawatts. All these application requires tight control of the material quality, for example, resistivity fluctuation can lead to weak spots in the device area where premature avalanche and hot spots may form leading to a complete failure of the device. Deep level defects are known to directly affect the electrical properties of the power devices. When they behavior as donor- or acceptor-type centers they may contribute to or compensate the free carrier concentrations. When they act as recombination or generation centers they would reduce the lifetimes of the material which affect the electrical properties of the device by increasing the forward voltage drop during current conduction or a high leakage current in the blocking state respectively. These issues were investigated in power p-i-n diode materials and thyristor materials which had an abnormally short lifetime and high leakage current/short lifetimes. Deep level defects detected in "bad device materials" were characterized and correlated with the observed macroscopic properties. In order to trace the origin of these deep level states we have thermally simulated some process stages via laboratory controlled heating and quenching

of the "as delivered" materials. The results then provided a insight into the formation mechanism and explained their often unforeseeable behavior in a real production line: a product dependent on the interaction between the defects inherent in the "as delivered" materials and defects "activated' by reactions involving thermal treatments and impurities present in the processing.

Investigations of process-induced defects in the above three categories will be presented in chapters 4, 5 and 6 respectively, their brief descriptions together with the rest of the arrangement of this thesis will be given as following:

Chapter 2 provides the background relating to defects in semiconductor silicon in terms of their structural, electrical/electronic and optical properties. It forms the foundation of the material characterization techniques discussed in chapter 3 and the studies of the defects reported in chapters 4, 5 and 6. A literature survey on the common defects seen in semiconductor silicon is also given in this chapter.

Chapter 3 describes characterization techniques used in the present study which covers the following three main areas:

Electrical: Deep Level Transient Spectroscopy (DLTS) and related techniques, Capacitance-Voltage (C-V) technique etc.

Structural: Double Crystal X-ray Diffraction (DCD), Transmission Electron Microscopy (TEM), Rutherford Backscattering Spectrometry (RBS) etc.

Optical: Photoluminescence (PL), Fourier Transform Infrared Spectroscopy (FTIR)

etc.

Detailed experimental configurations of them used in the present study are also provided in this chapter.

Chapter 4 presents the results from the study of the defects introduced by Ge^+ ion implantation and subsequent annealing processes. This chapter consists of two parts. Firstly it deals with the evolution of defects in the Ge^+ implanted and furnace annealed silicon (CVD epitaxy Si on CZ substrate) as a function of the annealing temperature. The evolution of various types of defects and their correlation with the macroscopic observation of the electrical and optical properties of the materials is proposed. In the second part it deals with the effect of oxygen in the starting materials (p-type CZ Si) on the residual defects introduced by Ge^+ implantation and subsequent rapid thermal annealing. Transmission Electron Microscopy (TEM), Photoluminescence (PL), Voltage-Current (V-I), Capacitance-Voltage (C-V) and Deep Level Transient Spectroscope (DLTS) techniques are used for this part of the study.

Chapter 5 discusses the SiGe alloy systems synthesized by implanting high doses of Ge^+ ions into silicon. By using either a carbon co-implantation or a silicon post amorphization in addition to the Ge^+ ion implantation the quality of the alloy materials is improved greatly. These improvements are explained using a model concerning the reduction of strain and the strain relief defects resulted from the respective processing. Rutherford Backscattering Spectrometry (RBS) and channelling analysis, Transmission Electron

Microscopy (TEM), Double Crystal X-ray Diffraction (DCD), Fourier Transfer Infrared Spectrometer (FTIR) etc. are used to characterize the materials.

Chapter 6 consists of two parts. The first part reports the characterization of deep level states in two types of silicon materials used in the manufacture of high power devices. The second part reports the study of deep level defects produced in the "as delivered" materials after thermal simulation of some aspects of production processing in order to find the origin of the deep states which have caused the degradation of the electrical properties of the power devices. Open Circuit Voltage Decay (OCVD) and Microwave Photoconductive Decay (μPCD) methods are used to measure the lifetimes, Deep Level Transient Spectroscope (DLTS) and Minority Carrier Transient Spectroscopy (MCTS) techniques are used to assess the characteristics of the deep level states.

Chapter 7 concludes this thesis by summarizing the results from chapters 4, 5 and 6. It also provides the suggestions for future work.

References

[Bean 84] Bean J. C., Feldman L. C., Fiory A. T., Nakahara S. and Robinson I. K., *J. Vac. Sci. Technol., A 2*, 1984, pp 436

[Bergholz 91] Bergholz W., Zoth G., Gelsdorf F. and Kolbesen, in *Defects in Silicon II*, eds., Bullis W. M., Gösele and Shimura F. (Electrochem. Soc., Pennington), 1991, pp 21

[Berti 91] Berti M., Mazzi G., Calcagnile L., Drigo A. V., *J. Mater. Res., Vol.6, no.10*, 1991, pp 2120

[Brotherton 89] Brotherton S. D., Ayres J. R., Clegg J. B. and Gowers G. P., *J. Electron Mater., 18*, 1989, pp 173

[Claeys 91] Claeys C., Vanhellemont J. and Simoen E., *Diffusion and Defect Data: Solid State Phenomena vol. 19&20*, 1991, pp 95

[Cowern 94] Cowern N. E. B., Vandewalle G. F. A., Zalm P. C. and Vandenhoudt D. W. E., *Appl. Phys. Lett., 65(23)*, 1994, pp 2981

[Fukami 90] Fukami A., Shuji Ken-ichi, Nagano T. and Yang C. Y., *Appl. Phys. Lett., 5(22)*, 1990, pp 2345

[Goetzberger 60] Goetzberger A. and Shockley W., *J. Appl. Phys.*, 1960, pp 1821

[Hart 81] Hart R. R., Hunsperger R. G., Dunlap H. L., and Marsh O. J., *Nucl. Instru. Meth. in Phys. Research B 191*, 1981, pp 70

[Kolbesen 91] Kolbesen B. O., Bergholz W., Cerua H., Fiegl B., Gelsdorf F. and Zoth G., *Nucl. Instru. Meth. in Phys. Research B 55*, 1991, pp 124

[Kramer 92] Kramer K., Talwar S., Sigmon T. W., Weiner K. H., *Appl. Phys. Lett., 61(7)*, 1992, pp 769

[Laanab 95] Laanab L., Bergaud C., Bonafos C., Martinez A. and Claverie A, *Nucl. Instrum. Methods in Phys. Research B 96*, 1995, pp 236

[Meyerson 86] Meyerson B. S., *Appl. Phys. Lett., 48*, 1986, pp 797

[Meyerson 88] Meyerson B.S., Uram K. J. and Legoues F. K., *Appl. Phys. Lett., 53*, 1988, pp 2555

[Paine 90] Paine D. C., Howard D. J., Stoffed N. G., and Horton J. A., *J. Mater. Res., 5,* 1990, pp 1023

[Servidori 87] Servidori M., Angelucci R., Cembali F., Negrini P., Solmi S., Zaumsei P. and Winter U., *J. Appl. Phys., 61,* 1987, pp 1834

[Shockley 48] Shockley W. in *Claim 2 of U. S. Patent 2 569 347,* Filed 26 June 1948

[Stoneham 95] *GeSi Strained Layers and their Applications* (Institute of Physics Publishing Bristol and Philadelphia, 1995), eds. Stoneham A. M. and Jain S. C.

[Zhang 94] Zhang J. P., Wilson R. J., Hemment P. L. F., Claverrie A., Cristiano F., Salles P., Wen J. Q., Evans J. H., Peaker A. R., Parker G. J., *Nucl. Instrum. Methods in Phys. Research B 84,* 1994, pp 222

Chapter 2 General Properties of Defects in Silicon

Semiconductor silicon is used for fabricating a galaxy of electronic devices. The performance and yield of these devices are closely related to the presence of defects and impurities in them. In this chapter we will first introduce the general properties of defects in semiconductor silicon followed by a brief literature review on some of the common defects in silicon.

2.1 Structural Properties of Defects in Silicon

2.1.1 Introduction

A perfect crystal consists of a three-dimensional array of atoms arranged on a periodic lattice. Any local or extended interruption in the periodicity of the lattice is a crystal defect. They are classified into four families according to the spread of the defect:

1 point-defects : correspond to one or a very few atoms (e.g. a vacancy)

2 line-defects : correspond to a line of atoms (e.g. an edge dislocation)

3 planar-defects: correspond to a plane of atoms (e.g. a stacking fault)

4 volume-defects: correspond to a volume of atoms (e.g. a precipitate)

Line-defects, planar-defects and volume-defects are classified as extended defects to

distinguish from point defects. Extended defects are also called non-equilibrium defects because they cannot be introduced at thermal equilibrium conditions whereas point defects is a thermodynamic requirement of the system [Kimerling 85] and so called equilibrium defects.

The defects can also be broadly classified into intrinsic defects which consist merely of lattice defects (physical imperfections) and extrinsic defects which involve foreign atoms (impurities).

2.1.2 Point Defects

2.1.2.1 Intrinsic and Extrinsic Point Defects

Point defects can be classified into intrinsic and extrinsic point defects.

Intrinsic point defects: Intrinsic point defects only involve lattice defects of the ordering of one or a few atoms, such as lattice vacancies and self-interstitials. Their concentrations and stability depend on the thermal and mechanical history, process history, impurities present in the crystal and sources at which they are generated or sinks at which they disappear. For example, ion-implantation is an effective source for the creation of intrinsic point defects [Ravi 88a].

Extrinsic point defects: Extrinsic point defects involve the incorporation of foreign impurity atoms, such as dopants, impurities introduced during crystal growth and

subsequent processing, for example oxygen, carbon and transition metals. Unlike metals and insulators, the electrical properties of a semiconductor is mainly controlled by the shallow donors and acceptors intentionally introduced through doping.

Figure 2.1 is a schematic diagram showing various types of point defects in silicon.

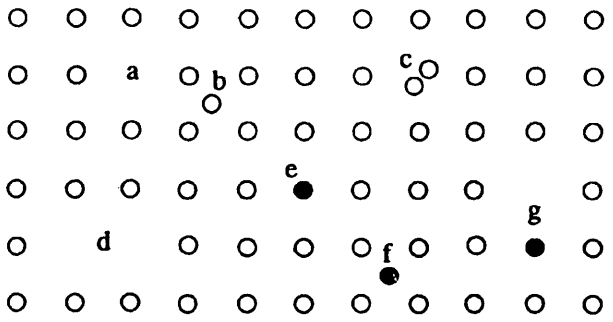

Figure 2.1 Schematic diagram showing various types of point defects in silicon
(a) vacancy (or Schottky defect when the created self-interstitial diffuses to the surface)
(b) self-interstitial
(a-b) Frenkel-pair: a vacancy close to a self-interstitial
(c) di-interstitial
(d) divacancy
(e) substitutional impurity
(f) interstitial impurity
(g) vacancy-substitutional impurity complex

2.1.2.2 Self-Interstitials and Vacancies in Silicon

Vacancies and silicon self-interstitials may be created thermally or by irradiation. Both defects are mobile at room temperature and the interstitials are mobile even at temperatures as low as 4 K in the presence of ionizing radiation [Watkins 64a]. Point defects tend to agglomerate and precipitate in the form of secondary defects. When the concentration of intrinsic point defects in the growing crystal exceeds the equilibrium value at any given temperature, the excess point defects will condense to form point defect clusters, dislocation loops and stacking faults. In dislocation-free crystals point defect agglomeration leads to discrete defects termed 'swirl defects'. There are three types of defects that comprise the swirl defects, they are often referred to as microdefects A, B and C. The A defects are small, micron sized dislocation loops. They are found to be interstitial in nature and they show several complex shapes and are often decorated by an impurity. The B defects are considerably smaller than the A defects. They are suggested to be small clusters of silicon atoms heterogeneously nucleated by an impurity with carbon being the most common suggested. The A defects are considered to be the by-products of the growth and transformation of the B defects. The D defects are tentatively suggested to be vacancy agglomerates. Wafers containing microdefects are found to give rise to stacking faults when subjected to oxidation [Ravi 81]. This is because oxidation generates interstitials and cause some of the microdefects to grow. They then collapse on to close packed planes to form stacking faults. Surface mechanical damage can also act as nucleation sites for the formation of stacking faults. Self-interstitials or vacancies can assist impurity diffusion, for example antimony diffuses through the vacancy mechanism [Frank 84] while the phosphorus diffuses via an interstitialcy mechanism.

2.1.3 Line Defects

2.1.3.1 Definition

A line defect is also called a dislocation. It is characterized by Burgers vector. Refer to Figure 2.2 (a), a closed circuit of arbitrary shape can be drawn from atom to atom through "good" crystal regions around the dislocation in the real crystal. Figure 2.2 (b) shows an analogous circuit between the corresponding atoms in a perfect crystal. The close failure vector, AB, in the latter circuit is defined as Burgers vector [Burgers 39]. Any dislocation can be decomposed into two basic types of dislocations, namely, edge dislocation (the line of dislocation is perpendicular to the Burgers vector) and screw dislocation (the line of dislocation is parallel to the Burgers vector).

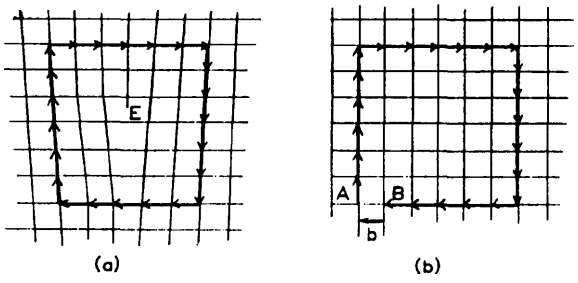

Figure 2.2 (a) the Burgers circuit around an edge dislocation E
(b) the analogous circuit between the corresponding atoms in a perfect lattice.

2.1.3.2 Dislocations in Silicon

Dislocations can be generated from point defect condensation, chemical impurity effects, thermomechanical stresses, irradiation damages and so on. For example, when the concentration of point defects in a growing/regrowing crystal exceeds the equilibrium value at a given temperature, the excess point defects will agglomerate and condense in the form of dislocation loops. These loops can either be faulted or occur as perfect prismatic loops. Ion implantation generates a high concentration of point defects which may agglomerate into dislocation loops during subsequent annealing processes. The chemical effect on dislocation formation can be demonstrated using phosphorus diffusion. The diffusion of a high concentration of phosphorus to make a p-n junction can generate a network of dislocations close to the surface. The mechanism involved in the defects formation is related to the misfit stresses between the silicon and the phosphorus atoms.

Hornstra [Hornstra 58] gives a complete description of the possible dislocations occurring in single crystal silicon. The most likely Burgers vectors for dislocations in the face-centered cubic (FCC) structure are of the type 1/2 <110>. This is because they have the shortest lattice vectors and the smallest energy. Of them the so called 60° dislocations are the most commonly observed in silicon. They lie on the {111} planes in the <110> directions with their Burgers vectors 60° to the dislocation lines. It is energetically favorable for them to dissociate into two sets of partial dislocations, namely 30° and 90° partial dislocations with a stacking fault in between. It has been demonstrated that most dislocations in silicon are dissociated, that is, they consist of partial dislocations separated from each other with the dissociation distances being of

the order of 50 Å [Cockayne 69].

There exist two sets of dislocations in silicon: the glide set (glissile) and the shuffle set [Hirth 68].The glissile dislocations glide on close packed glide planes and can dissociate into a pair of Shockley partial dislocations which are also glissile. The shuffle set of dislocations is formed by the insertion of extra planes of atoms between layers of atoms.

2.1.4 Planar Defects

A planar defect is a two dimensional defect where the regular sequence of stacked layers in the crystal is interrupted. They are also called stacking faults. Figure 2.3 (a) shows the stacking sequences of close-packed (111) planes in a perfect crystal of FCC structure. There are three types of stacking faults present in a FCC structure, namely, (1) an intrinsic stacking fault, shown in Figure 2.3 (b), which can be thought of as a part of C layer being removed, (2) an extrinsic stacking fault, shown in Figure 2.3 (c), as a part of an extra A layer has been inserted into between a B and an A layer and (3) a twin stacking fault (not shown), which is produced by imposing reflection symmetry through a plane midway between a neighboring pair. The silicon structure, however, consists of two interpenetrating FCC lattices, one with origin at (0,0,0) and the other at (1/4,1/4,1/4)a, the {111} layers are AA'BB'CC'AA'BB'CC' instead of ABCABC. Twin stacking faults are rarely seen in silicon, they are usually introduced by improper crystal growth [Shimura 89]. Intrinsic stacking faults are observed in epitaxial layers [Zulehner 82]. The most commonly observed stacking faults are oxidation-induced stacking faults (OISFs) which are extrinsic in nature.

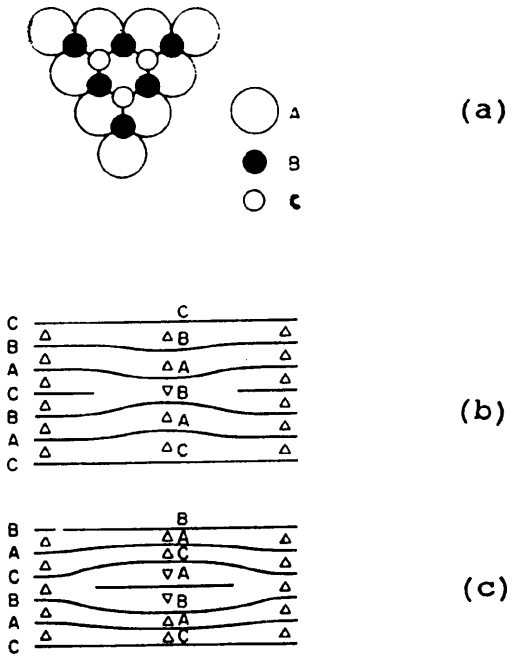

Figure 2.3 (a) stacking sequence of (111) planes in FCC structure
(b) an intrinsic stacking fault
(c) an extrinsic stacking fault

2.1.5 Volume Defects

Volume defects are three dimensional defects, they may be defect clusters, agglomerates, precipitates, voids etc.. Sometimes the distinction between a point defect and a volume defect is not well defined.

2.2 Electronic Properties of Defects in Silicon

2.2.1 Electronic Properties of Perfect Silicon Crystal

The crystal structure of Silicon is of the diamond lattice form in which each atom lies in the centre of a tetrahedron formed by the four nearest neighbors. The binding is of the covalent type. The valence electrons are relatively mobile and may contribute to the optical and electrical transport in the crystal. In the band structure theory the actual crystal is represented by a perfect periodic lattice, neglecting defects and lattice vibrations and assuming the electron moves independently of other electrons in a static potential **V(r)** having the periodicity of the lattice. In the model, the electrons in the solid are characterized by Bloch functions of the form:

$$\Psi(r)=u_k(r)\exp(ik\bullet r) \tag{2.1}$$

where k is the wave vector and $u_k(r)$ is a function with the periodicity of the lattice. The Bloch functions are plane waves modulated by $u_k(r)$ which is related to the potential **V(r)**. The periodic lattice is described by a set of vectors R_i so that a translation by R_i reproduces the potential at the origin:

$$R_i=M_{i1}a_1+M_{i2}a_2+M_{i3}a_3 \tag{2.2}$$

where a_1, a_2 and a_3 are the shortest possible independent periodic translations of the

lattice and the M_i are integers. We define another set of points called the *reciprocal* lattice, using the vectors K_j :

$$K_j \bullet R_i = 2\pi n_{ij} \tag{2.3}$$

where n_{ij} is an integer. K_j is expressed in terms of elementary translations:

$$K_j = N_{j1} b_1 + N_{j2} b_2 + N_{j3} b_3 \tag{2.4}$$

Where N_j are integers and these elementary translations in the reciprocal lattice are related to those in the real lattice by:

$$b_1 = 2\pi \frac{a_2 X a_3}{a_1 \cdot a_2 X a_3} \quad b_2 = 2\pi \frac{a_3 X a_1}{a_1 \cdot a_2 X a_3} \quad b_3 = 2\pi \frac{a_1 X a_2}{a_1 \cdot a_2 X a_3} \tag{2.5}$$

After the reciprocal lattice is defined the electron energy $E(k) = E(k + K_j)$ becomes periodic in it. Therefore to define the electron energy dependence on momentum uniquely it is sufficient to use the k values within the unit cell of the reciprocal lattice which is called the first *Brillouin zone*. Figure 2.4 (a) shows the first Brillouin zone of the diamond lattice and Figure 2.4 (b) shows the band structure of silicon. Note the centre of the Brillouin zone is denoted Γ. The intersections of the <111>, <100> and <110> axes with the zone edges are denoted L, X and K respectively [Long 68]. In the silicon band diagram, the forbidden energy ranges are indicated as well as the variation of the electron energy with direction. Silicon is an indirect bandgap semiconductor in which the conduction band minima and the valence band maximum does not occur at the same k value.

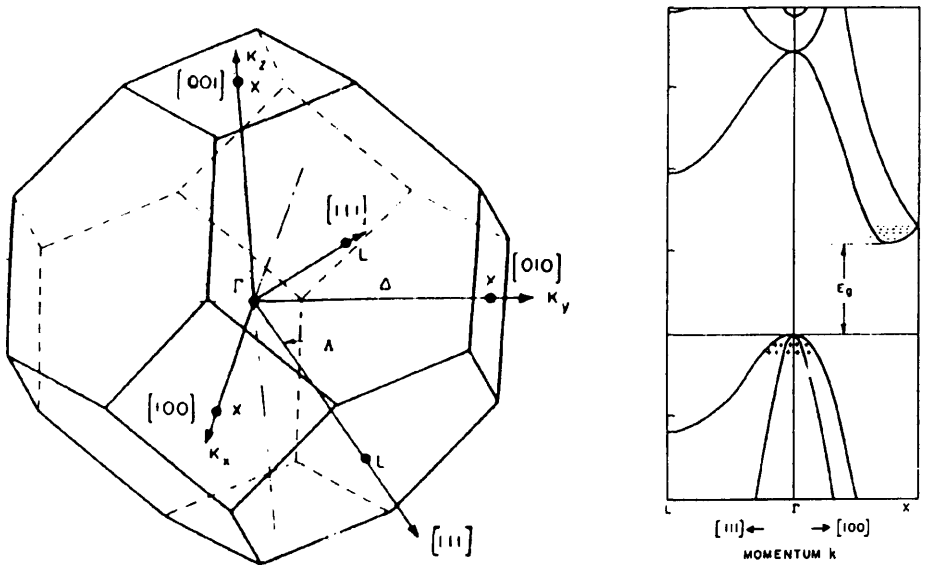

(a) (b)

Figure 2.4 (a) first Brillouin zone of the diamond lattice with the most important symmetry points and lines indicated (b) energy band structure of Si

The concept of effective mass is used because the carriers in semiconductors can be characterized by properties in many ways comparable to those of free electrons under vacuum, replacing the carrier mass by effective mass takes into account the averaged interaction of the carrier with the periodic lattice potential. It is reflected in the E(***k***) versus ***k*** curve, the steeper the curve the smaller the effective carrier mass.

2.2.2 Electronic Properties of Silicon with Shallow Impurities

When atoms from the columns of the periodic table adjacent to the host crystal atoms

are introduced substitionally, the valence electrons are either in excess or fewer than those from the host atoms, for example in the case where phosphorus (P) is introduced into silicon we have one more electron than is needed for covalent bonding to the nearest neighbors. The excess electron is relatively weekly bounded to the P atom and therefore the energy needed to free this electron is much less than the bandgap energy. A donor is introduced if the number of valence electrons exceeds that in the host crystal, whereas an acceptor, has fewer electrons than the host crystal. The binding energy of electrons or holes for these "shallow" donors or acceptors is obtained using "hydrogenic model". In the model the impurity is treated as a hydrogen atom using the static dielectric constant of the material and the effective mass m_c^* for electrons and m_v^* for holes of the relevant crystal. Furthermore the extent of the wave function of electrons or holes can be estimated using the first Bohr radius and it is found that it is considerably in excess of the lattice parameter. Hence the necessity to involving general properties of the host crystal such as the static dielectric constant and the effective mass. The calculation indicates that most of the shallow donors or acceptors are ionized at room temperature (hence the name shallow impurity), which means that the extra electron or hole is no longer bound to the impurity. Consequently in a crystal that contains only shallow donors or only shallow acceptors, the free carrier concentration is almost equal to the impurity concentration. The crystal is said to be compensated when both donors and acceptors present. The crystal is n-type when donors are in excess otherwise it is p-type. However there will be always both types of carriers present because the product of the electrons and holes in a nondegenerate crystal in thermal equilibrium is a constant at a given temperature. Doping of shallow impurities is widely used in semiconductor technology for modifying the amount and type of electrical conductivity.

2.2.3 Electronic Properties of Silicon with Deep Levels

When the impurities are not "shallow" impurities, that is when the wave function associated with an electron bound to the impurity is highly localized and the short range part of the atomic potential is important, the hydrogenic description no longer fits. These 'non-hydrogenic' impurities can produce energy levels anywhere in the bandgap or even in the bands themselves and are known generally as deep levels [Jaros 82]. The interaction of free carriers with such defects generally causes a degradation of device performance. For example, defects can be inadvertently introduced by contamination during device fabrication. If such defects have energy levels near the midgap, they can be very efficient carrier generation centers and they can cause high leakage currents in devices. Defects are also intentionally incorporated to controllably modify the electrical or optical properties of semiconductors. For example gold is introduced in silicon as efficient recombination centers for high speed switching purpose and indium in silicon for extrinsic optical absorption in the far infrared region. There is no general formalism to predict the physical properties of these centers. Characterization of these deep levels are through parameters describing the electrical and optical properties. They include: energy position of the impurity level within the bandgap, the probabilities of capture and emission processes and the concentrations of deep state levels.

The Shokley-Read-Hall (SRH) model [Shockley 52] is used to describe the kinetics of charge transfer between a deep level and the bands. It is assumed that a deep level changes its electron occupancy only through carrier transitions between the level and the bands. Electron transfer between deep levels is neglected, lattice interactions and multi-electron states are ignored for the moment. The deep levels are assumed not to

influence the motion of the electron or holes, they are ballistic. This kinetic model is based on the point defect theory and a capture mechanism state, using electron capture as an example, any electron falling within a capture radius r_o ($\sigma_n=\pi r_o^2$ is called the capture cross section) of the defect (electron empty) is captured with a probability of one. For a detailed analysis refer to Chapter 3.

2.3 Brief Literature Review on Some Common Defects in silicon

2.3.1 Radiation Damage Induced Defects in Silicon

Radiation damage of a semiconductor material is caused by nuclear radiation impinging on the semiconductor material as a result of, for example, doping the semiconductor using ion implantation or neutron transmutation technology. There are two main basic aspects of the interaction between an incident nuclear particle and a target atom. (1) the collision between the incident energetic particle and the electrons in the target material (2) the collision between the nuclei of the incident particle and that of the target material atom. It is this latter reaction causes radiation damage. When the energy transferred from the incident particle to the lattice atom exceeds the displacement threshold energy, which is 10 to 25 eV for most semiconductors, the lattice atom will be displaced to an interstitial position. Under the radiation conditions we are concerned with here it is easy to free an atom from its position and make it travel through the target as a second projectile. Now both the incident particle and the displaced atom travel and can make further displacements causing cascade collisions. As a result,

regions of localized damage occur and they usually consist of vacancies and self-interstitials. Lattice vacancies and self interstitials are quite mobile at room temperature. They can migrate through the lattice and recombine with each other or come to a surface where they are annihilated. They can also be trapped by lattice defects and impurities. The resulting defects are quite complicated consisting of vacancy/interstitial complexes and/or clusters and dislocation loops. Furthermore these defects will change or evolve during the subsequent processes. Electron irradiation studies have produced a great deal of information about such defects. In particular, defect identification resulting from Electron Paramagnetic Resonance (EPR) and Infrared (IR) spectroscopy studies have been directly used to provide detailed descriptions of some of these simple lattice defects. Such information can then be used as a starting point in the identification of damage produced by more complicated processes such as ion implantation and neutron transmutation doping.

2.3.2 Vacancy Related Defects in Silicon

Vacancy and vacancy-related defects in silicon are generally introduced during crystal growth and radiation processes such as ion implantation and neutron transmutation doping. Knowledge of their properties is very important and fundamental in understanding defect interaction, diffusion and annealing in silicon. The isolated vacancy is extremely mobile and reacts very easily with other impurities generating vacancy related complexes and introducing deep electronic levels into the bandgap. There are four commonly observed vacancy related defects in silicon [Peaker 87]: The isolated vacancy, the divacancy, the oxygen-vacancy pair (A center) and the

phosphorus-vacancy pair (E center).

The **isolated vacancy** defect has double positively charged state V(++), single positively charged state V(+) and a neutral state V(0). In the lower half of the band gap a deep level with an activation energy of 130 meV measured by Deep Level Transient Spectroscope (DLTS) technique corresponds to the hole emission resulting from V(++) state to V(+) state transition but the magnitude represents transition from V(++) to V(+) and from V(+) to V(0), giving a DLTS signal of twice the expected amplitude. This is because the removal of the second hole requires less energy than the first one. This behavior was predicted in Baraff 's work [Baraff 80]. There are two charged states V(--) and V(-) giving two levels in the upper half of the band gap. But they are not observable from DLTS measurement. The V(-) level is measured from EPR technique and V(--) from IR technique. The isolated vacancy is quite mobile at -23°C and starts to react with impurities to create vacancy complexes.

The **Divancancy** is an intrinsic defect in silicon produced by high energy particle irradiation. It consists of two vacant nearest-neighbor lattice sites each surrounded by three occupied lattice sites [Watkins 65]. It introduces three deep levels in the bandgap with four possible charged states. They are the double negatively charged state di-V(--), single negatively charged state di-V(-), single positively charged state di-V(+) and neutral state di-V(0). Two electron emission peaks from DLTS measurements are observed for the transition from the di-V(--) state to the di-V(-) state (with an activation energy ~ 230 meV) and from the di-V(-) state to the di-V(0) state (with an activation energy ~ 410 meV) respectively [Brotherton 82]. The 410 meV level has a DLTS peak coincides in temperature with the phosphorus-vacancy (E center) center and so care

must be taken to distinguish between them by a choice of material or by annealing studies. The state at 210 meV [Kimerling 77] has been linked to the emission of a hole from the di-V(+) state. The divacancy is stable in silicon up to ~ 280°C. The type of divacancy produced during low temperature irradiation of n-type silicon are quite different from that produced at room temperature. It is called non-reorientable divacancy [Watkins 75] which has two silicon interstitials trapped nearby.

The **A center** (oxygen-vacancy center) is formed when a mobile lattice vacancy is trapped by an interstitial oxygen atom. The oxygen atom bonds to two of its four nearest silicon neighbors, with the remaining two silicon neighbor atoms pulling together to form a covalent bond. An additional electron can be trapped in an antibonding orbital of this Si-Si molecule and it is this additional electron which is observed in the ESR measurements [Watkins 61] and gives an electron activation energy of 170-180 meV in the DLTS measurements [Brotherton 82]. It is an acceptor-like electron trap. The A center is characterized optically by vibrational absorption lines at 836 and 884 cm^{-1} [Whan 67].

The **E center** (phosphorus-vacancy center) introduces an acceptor-like deep level located at 440 meV below the conduction band edge. The electron capture cross section is found to be 3.7×10^{-15} cm^2 [Brotherton 82]. An early EPR study shows that this defect is formed by the trapping of a mobile lattice vacancy next to a substitutional phosphorus atom [Watkins 64b]. However complications arise when it is shown that the DLTS peak has two components, one being the 440 meV state and the other being associated with a substitutional phosphorus-interstitial carbon ($P\text{-}C_i$) pair defect [Asom 87] which displays a number of metastable configurations [Kimerling 80].

Photoluminescence is also a very useful tool in studying radiation damage induced radiative centers. For example the 1018 meV ('W' line) PL line is created by bombardment of silicon with neutrons or ions. It is frequently observed in the studies of the effects of radiation damage in silicon [Tkachev 77], recombination radiation from ion implanted silicon [Kirkpatrick 76], neutron transmutation of silicon [Rostoworoski 81] and laser annealing of ion implanted silicon [Skolnick 81]. Most of the optical centers have been shown to be associated with carbon but oxygen is also involved in some of the optical centers created by radiation damage.

2.3.3 Deep Levels Associated with Dislocations in Silicon

Dislocations and the point defect clouds surrounding them are extended multi-electron defects. They have a long range electric and elastic potential which modifies capture and emission of electrons at these defects. Due to the interaction among charge carriers occupying the extended defect an electrostatic potential is built up around the defect which limits the successive charge capture. The DLTS lines which exhibit a logarithmic filling law [Schröter 89] show also symmetric, or asymmetric broadening effect connected with non-exponential transient of electron emission from this type of defect.

There has been a considerable amount of work on the deep level characterization in silicon associated with dislocations introduced by plastic deformation, followed by annealing at temperatures in the range 600-900°C [Omling 85]. In n-type silicon it is proposed that the deep levels detected in plastically deformed silicon can be classified into four groups labelled as A to D. It is suggested that B group deep levels, with an

activation energy for electron emission of 0.27-0.29 eV, and the D group, 0.54-0.68 eV, are related to point defects located within, or very close to, the dislocation core. At low electron occupancy the electron capture cross sections of the D and B levels are found to be 6 x 10^{-16} cm^2 and 7 x10^{-16} cm^2 respectively. Comparison with EPR spectra suggests [Weber 83a] that the B level is a shallow dopant located in or around dislocations. The group of levels referred to as A, with electron emission activation energies of 0.18-0.19 eV is believed to be related to impurities in or around the dislocation core. The group of levels C, C_1 (0.37-0.52 eV), and C_2 (0.48-0.51 eV) are related to dislocation dangling bonds or kinks in the dislocations. D and B groups are annealed out at 800°C but C and A groups are stable at this temperature. In dislocated p-type silicon Kimerling [Kimerling 79] reports eight hole traps. One of the level with hole emission activation energy of 0.35 eV remains after a 900°C anneal. Kveder [Kveder 82] reports a similar result though the defect energy levels are different and there is a large discrepancy in the annealing behavior. Both believe that the change in the defect spectrum upon annealing is due to reconstruction of dangling bonds at the dislocation core. Ono [Ono 85] reports a similar level compared to the 0.35 eV level but it disappears after a 900°C anneal. A model based on kinks or jogs along the dislocations and a model based on agglomerations of point defects which are the debris resulting from dislocation formations are proposed.

It has been suggested that the deep levels in Group A to D may relate to impurities decorating the dislocations. Studies of the electrical effects of the decoration of the Frank partial dislocations bounding oxidation induced stacking faults show that below the impurity concentration at which precipitation occurs, decoration of a stacking fault moves the associated deep levels in the bandgap towards mid-gap, irrespective of the

species of transition metal used for decoration [Peaker 89][Berg 92] and the carrier capture changes from point defect-like to dislocation defect-like. Kaniewski [Kaniewski 92] studies the electrical activity of oxidation induced stacking faults in silicon and finds that if the entire stacking fault is examined, a broad, almost featureless DLTS spectrum is observed. If the fault is spatially profiled, the spectrum deconvolutes into DLTS peaks usually associated with point defects. One peak is observed to change its activation energy according to its position along the Frank partial dislocation bounding the stacking fault. These results suggest that band bending resulting from the charge (which can be influenced by the degree of impurity decoration) on the dislocation may explain the electron emission behavior from these deep states.

2.3.4 Oxygen Related Defects in Silicon

2.3.4.1 Oxygen Incorporation and Its Fundamental Properties in Silicon

Oxygen is a key impurity in silicon. Oxygen is incorporated when a silicon crystal is pulled from molten Si held in a silica crucible in the Czochralski (CZ) growth process. At its melting point silicon reacts with quartz resulting in the dissolution of oxygen to saturation levels in the crystal. The equilibrium solid solubility C_s of oxygen in silicon can be expressed as [Mikkelsen 86]:

$$C_s(T)=C_{so}\exp\frac{-E_s}{kT} \tag{2.6}$$

where $E_s = 1.52 \pm 0.3$ eV is the heat of solution and $C_{so} = 9 \times 10^{22}$ cm^{-3} is a constant. Consequently the equilibrium concentration at the melt temperature is ~ 2×10^{18} cm^{-3}. This concentration is largely frozen in during cooling, leaving the silicon crystal grossly supersaturated in oxygen. The oxygen is incorporated as isolated interstitial atoms, with preferential bonding to two adjacent Si atoms, giving rise to the well known infrared absorption band at 1106 cm^{-1} (at room temperature). The oxygen concentration is normally determined from the strength of this absorption. The concentration [O] in CZ silicon ranges from 2×10^{17} cm^{-3} to 2×10^{18} cm^{-3}. In float-zoned (FZ) silicon the oxygen concentration is from 2×10^{15} cm^{-3} to 2×10^{16} cm^{-3}. The source of oxygen in FZ silicon is not as clear. Diffusion of the oxygen atom occurs by an elementary step in which it jumps from one <111> bond to an adjacent one. The diffusivity of interstitial oxygen in silicon is expressed as [Mikkelsen 86]:

$$D = 0.13 \exp^{\frac{-2.53}{kT}} cm^2 s^{-1} \qquad (2.7)$$

The isolated interstitial oxygen atoms do not produce photoluminescence (PL). But it introduces a broadening effect on the PL lines associated with other transitions because interstitial oxygen expands the lattice linearly with its concentration [Takano 73]. There have been no reports of the electrical activity of the interstitial oxygen.

2.3.4.2 Oxygen Precipitation

Annealing oxygen containing crystals results in the formation of the oxygen precipitates

(OP's) and related extended defects. In some cases these bulk defects can be beneficial if their distribution can be carefully controlled. This is the basis of the intrinsic gettering (IG) technique which is usually achieved by a three step "high-low-high" thermal cycle [Matlock 83]. During the first high-temperature anneal (about 1100°C), the oxygen near the surface diffuses out, forming a denuded zone of typically 10-20 μm. The subsequent low-(650°C- 750°C) and high-(about 1000°C) temperature anneals are for the nucleation and growth of OP's, respectively, in the bulk region where a high supersaturation of oxygen is maintained. The strain field and dislocations associated with the precipitates attract metallic impurities leading to a removal of harmful contamination from the device active layer. Oxygen precipitates appear to have different features/stages depending on the annealing temperature. Annealing at 650°C introduces rod-like defects [Bourret 84] which are formed by aggregation of silicon self-interstitials [Reiche 88] and will transform to precipitates at a later stage. Near 800°C, square-shaped precipitates on the (100) planes with <110> edges are predominant [Wada 80]. And finally, at temperatures above 1000°C octahedral precipitates bound by (111) planes are observed. There are many factors affecting the precipitation process in terms of nucleation, growth, morphology and chemical composition [Inoue 86], such as: oxygen concentration, annealing temperature, time and ambient, thermal history of the specimens, intrinsic point defects and impurities, wafer damage, etc..

NUCLEATION

There are two nucleation mechanisms, homogeneous and heterogeneous.

Nucleation during annealing: The classical nucleation theory supports the homogeneous nucleation model during annealing. It is assumed that an equilibrium distribution of cluster sites ("embryo") exists. However, the existence of a heterogeneous nucleation

mechanism is also reported [Oehrlein 82] where carbon atoms are assigned as heterogeneous nucleation sites.

Nucleation during cooling after crystal growth: It is found that there are two types of precipitates. Microprecipitates, about 10 Å in size, are related to homogeneous nucleation during cooling below 950°C [Inoue 82]. Large precipitates, about 1000 Å in size, are related to heterogeneous nucleation [Wada 82] since at the cooling temperature near 1200°C homogeneous nucleation is negligible. So the nucleation mechanism is not unique but changes with temperature. Therefore it is widely accepted that the heterogeneous nucleation of oxide precipitates dominates at high temperature and the homogeneous nucleation dominates at low temperature (during cooling).

Influences from thermal donors, thermal history of specimens and impurities

One of the model suggests that thermal donors are a series of SiO_x clusters including 3 to 5 oxygen atoms. They are introduced into CZ silicon by annealing at temperatures near 450°C [Fuller 54]. They disappear during annealing at above 650°C. This is thought to be due to the absorption of an additional oxygen atom, or a change into precipitates including more than 5 oxygen atoms [Kaiser 58]. The influence of the specimens' thermal history is clearly demonstrated from the fact that a low temperature preannealing enhances precipitation in the following high temperature annealing [Takaoka 79], and high temperature preannealing retards precipitation [Kishino 82]. Oxygen precipitation is enhanced by the presence of subsidiary impurities such as carbon [Kishino 82], nitrogen and hydrogen and acceptor impurities such as boron. This is because they can either provide heterogeneous nucleation centers or enhance oxygen diffusion. On the other hand oxygen precipitation is retarded by dissolved self-interstitials and donor impurities such as P, As and Sb [Fair 85].

Oxidizing annealing ambient is reported [Hu 80] to retard oxygen precipitation.

Specimen backside damage is reported [Takano 81] to enhance oxygen precipitation. Finally it should be emphasized that oxygen precipitation does not occur when the $[O_i]_o$ is less than a certain threshold/critical concentration $[O_i]_c$ (~14 ppma in a general case) but this condition varies depending on many factors such as intrinsic point defects and impurities.

GROWTH MECHANISM

Growth of small octahedral precipitates formed by annealing at 1100°C is found to follow nearly a parabolic relationship which is characteristic of diffusion limited growth [Yang 78]. The growth of platelet oxide precipitates in the range of 750°C-1050°C is found to follow a $t^{3/4}$ relationship [Wada 80]. A similar mechanism applies to smaller precipitates down to 20 Å formed at temperatures 650°C and 870°C with preheating at 450°C. These experimental results combined with the standard equation for diffusion limited growth of precipitates (Johnson-Mehl equation) make precise oxide precipitate size control possible.

DEFECTS FORMATION DUE TO OXYGEN PRECIPITATION

The formation of oxygen precipitates in the bulk is accompanied by a local volume expansion that results in a compressive stress at the Si/OP interface. Such a stress inside the crystal can be released by generating dislocation loops, absorbing vacancies, and/or emitting Si self-interstitials. Extrinsic stacking faults that are often observed in oxygen precipitated silicon are strong evidence for the emission of self-interstitials because they are a condensed precipitate form of supersaturated self-interstitials. The question of when and how point defects are formed is still a problem. It is found that oxygen precipitation at 750°C does not generate dislocation loops, but precipitation at 850°C

frequently does [Wada 80].

ELECTRICAL AND OPTICAL PROPERTIES OF PRECIPITATES

Electrical: It is found that precipitates larger than 100Å are electrically active [Miyagi 82]. The degradation of the carrier lifetime due to oxygen precipitation has been reported by Yang [Yang 78]. A model of carrier recombination at oxygen precipitates is proposed by Hwang [Hwang 86] that the carrier recombination at OP's takes place through Si/OP interface states similar to conventional Si/SiO_2 interface states. These interface states are detected by DLTS measurements as a broad peak indicating a continuous distribution of energy states in the band gap. The density distribution of Si/OP interface states behaviors in a similar way as in the Si/SiO_2 interface states in MOS structures. Furthermore the so called P_b center, often observed in as-oxidized MOS devices, known to be a trivalent silicon dangling bond state [Johnson 79] has a donor state with activation energy of hole emission of 0.3 eV and an acceptor state with electron emission activation energy of 0.25 eV which are in close agreement with two of the density peaks from the Si/OP's interface states [Hwang 86]. Kaniava suggests that two deep levels with activation energies of electron emission of 0.17 eV and 0.43 eV related to oxygen precipitates are responsible for causing the leakage current in p-type silicon [Kaniava 94].

Optical: Gaworzewski [Gaworzewski 84] and Hu [Hu 80] have undertaken a systematic study of the precipitates in relation to observed infrared absorption bands and classified them. They attribute the broad infrared absorption at 1100 cm^{-1} to small, globular precipitates produced at lower temperatures. The two absorption bands that appear at 1250 and 1100 cm^{-1} are attributed to platelike precipitates produced by medium

temperature heat treatment. Higher temperature heat treatment produces precipitates exhibiting bulk silicate properties, when these precipitates have octahedral coordination, they lead to infrared absorbance at 1106 and 470 cm^{-1}. The same authors have also shown that an amorphous, platelet-like precipitate is responsible for an absorption band around 1225 cm^{-1}. Most of the observed bands in the spectra of the various precipitates have been assigned to the various phonon modes in the silicon-defect lattice by the above authors.

The relationship between PL signals and oxygen precipitates implies in its introduction of dislocations and the impurities gettered around it. Tajima [Tajima 83] reports a photoluminescence line at 0.903 eV which coincides with the concentration dependence expected for Si self-interstitials emitted during the oxygen precipitation process and hence suggests that this PL line is associated with microdefects and Si self-interstitials resulting from oxygen precipitation. In the same paper the author finds that the disappearance of the 0.903 eV line is accompanied by the appearance of the D1 and D2 dislocation lines. Therefore the author concludes that the 0.903 eV line involves Si self-interstitials either as single self-interstitials or in the form of small clusters. This line is suggested by Lightowlers [Lightowlers 94] to be related to rod-like defects.

The D-line (D1: 812 meV; D2: 875 meV; D3: 934 meV and D4: 1.00 ev) luminescence has been commonly observed when oxygen precipitation occurs although the exact origin of them is still unknown. There are many other ways that are known to introduce D lines, for example, plastic deformation of silicon [Drozdov 76], silicon ion implantation and subsequent annealing [Uebbing 80]. Two models have emerged regarding the origin of the PL features observed from dislocated Si. Either the radiative

electronic transition involves capture into a strain field potential associated with the dislocation, or it involves excitonic collapse onto impurities residing at dislocations and possibly interacting with point defect clusters present in dislocated samples [Kimerling 79]. Evidence of the involvement of defects other than dislocations is the absence of the D line luminescence in plastically deformed silicon without a deliberate contamination with Cu [Higgs 90].

2.3.4.3 Oxygen Thermal Donors (TDs) and "New Donors"(NDs)

Thermal donors (TDs)

Structural: Though there have been more than 30 years's study of thermal donors there still remains the question: what are the donor's constituents? Many models have been suggested. Initial attempts to define a structure for the center are based on formation kinetics during heat treatment. The initial rate of increase in electron concentration exhibits an isothermal proportionality to the fourth power of the oxygen concentration [Kaiser 58]. This concentration dependence is presented as evidence for a cluster of four oxygen atoms in the center. However it can not explain why the measured rates of donor formation require a diffusivity which is a factor of 10-100 times higher than accepted values. The other model is that the centre is an effective mass, helium-like center. This effective mass nature of the electronic state results in a delocalized electron wave function. But this does not provide a good probe of the thermal donor's detailed atomic structure.

Electrical: The thermal donor acts as a double donor defect which introduces two defect states in the silicon energy gap: 0.07 and 0.15 eV below the conduction band. The

presence of the two states has been confirmed by Hall effect [Wruck 79], DLTS [Kimerling 81], infrared absorption [Suezawa 84] and formation kinetics [Wada 84] data.

Optical: It appears that many photoluminescence lines are produced under conditions similar to those used for thermal donor production [Robbins 85]. Two sets of iso-valent centers are tentatively assigned to the cores (and modified cores) of thermal donors [Thewalt 86][Steele 87] but no photoluminescence complex has yet been unambiguously related to thermal donors. Deep level luminescence at 0.767 eV has been related to thermal donors [Tajima 81].

"New donors"(NDs):

Thermal oxygen donors which are formed above 600°C are called 'new donors' in order to be distinguished from thermal donors (TDs). Their structures remain unanswered. They have donor characteristics which can be terminated by high temperature annealing above 900°C. The electrical activity of the (old) TDs can be terminated by short time annealing above 550°C. But the TDs complexes are not destroyed completely [Ourmazd 84]. The remaining complexes grow further by absorbing oxygen atoms forming larger oxygen silicon complexes and later on small needles of coesite (rod-like defects sometimes [Tempelhoff 79]). DLTS measurements reveal a continuous spectrum in silicon with NDs [Hölzlein 86]. Admittance spectroscopy measurements on n-type silicon reveal a low temperature peak of activation energy 28 meV. This shallow level is suggested to be responsible for the change in resistivity in the same sample [Peaker 83]. Electron Spin Resonance (ESR) measurements show both crystalline and amorphous SiO_x precipitates [Wörner 86]. TEM, Resistivity, IR absorption and luminescence measurements show NDs are oxygen clusters nucleated at TDs,

dislocation dipoles and carbon atoms [Yasutake 82].

2.3.4.4 Oxygen Induced Stacking Faults (OSIFs)

Structural: The stable OISFs are always found to lie on {111} planes, bounded on one side by a surface or near the surface and the other side by a nearly semicircular (1/3)a <111> Frank dislocation loop [Hsieh 73]. OISFs can be introduced into silicon crystals as a result of oxidation, impurity and dopant diffusion and ion implantation. In the case of oxidation, generation of stacking faults near the wafer surface can be considered in two stages. The first stage is the generation of nucleating centers. The second stage is the growth of stacking faults, which occurs during the oxidation. Two events are observed during oxidation: (1) an excess concentration of silicon self-interstitials (or other impurity atoms) are produced (2) these excess atoms condense to form the localized extra planes of atoms between close packed planes. It is modelled that preexisting dislocations are dissociated to form a Shockley partial and a Frank partial bounding a stacking fault. These are the two important partial dislocations in FCC structure. The Shockley partial can move by glide and the Frank partial can move by climb only. Under some conditions, the Shockley partial glides out of the crystal, leaving behind the fault and the bounding Frank partial. Figure 2.5 is the schematic process of this event. The same principle applies to other situations but the detailed process differs according to the particular physical environment. For example in the ion implantation case the self-interstitials are generated by the implantation process and the damage at the original crystalline and amorphous interface may act as nucleating centers.

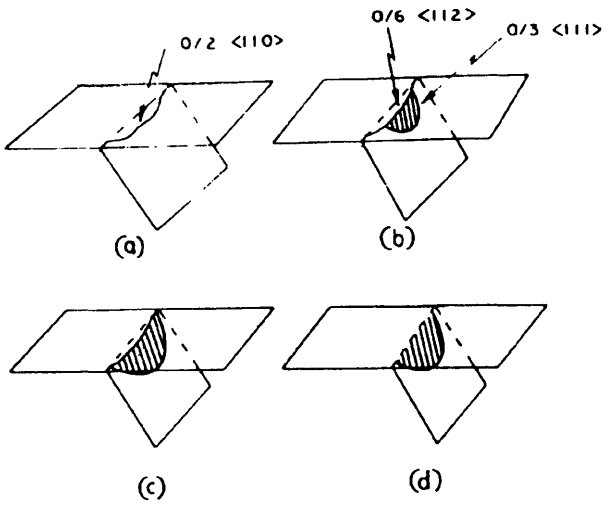

Figure 2.5 Schematic depiction of the generation of an extrinsic stacking fault from a dislocation **(a)** the a/2 <110> dislocation **(b)** the reaction: a/2 <110> → a/6 <112>(Schockley partial) + a/3 <111>(Frank partial) **(c) and (d)** show the Schockley partial glides to the surface and Frank partial climbs down

Electrical: OISFs in the active region of silicon p-n junctions cause an increased reverse leakage current [Huff 85] and increased forward voltage drop [Liang 80]. OISFs in MOS capacitors can cause refresh failures in memory cells [Ravi 88b]. Studies of the origin of the electrical activity of stacking faults indicate that the impurity atmosphere that surrounds the fault is the most essential parameter. Increased decoration within a certain limit has shown increased electrical activity of stacking faults [Peaker 89]. DLTS measurements show that the activation energy of the stacking faults related deep level increases when either Au or Pt is diffused into the sample, tending to move the state towards midgap where it acts as a more powerful generation center. The capture properties of the deep level are also changed from point defect-like towards logarithmic behavior. Reported electrical effects of OISFs on devices are often similar to those reported for dislocations. This is reasonable because every stacking fault is associated with a dislocation loop which bounds the fault plane. Kawado has studied the Electron

Beam Induced Current (EBIC) contrast around OSIFs and concludes that the recombination is associated primarily with the Frank partial [Kawado 80][Ourmazd 84].

Optical: D lines (D1 and D2 lines) are observed from materials containing oxidation induced stacking faults [Evans 92]. Lightowlers [Lightowlers 89] suggests that transitions associated with dislocations decorated with transition metals are responsible for the D-band luminescence. Peaker [Peaker 89] reports a PL spectrum dominated by the D1 line with a weak D2 emission. Diffusion of Au or Pt has modified the D1 line making it broadened on the low energy side and an additional broad feature appears approximately 50 meV below the D1 peak.

2.3.5 Carbon Related Defects in Silicon

Isolated carbon in silicon occupies substitutional site. It gives an infrared absorption band at 16.5 μm [Newman 65] but this band is superimposed on the strongest intrinsic two-phonon band of Si [Johnson 59]. Typical carbon concentration measured from the 16.5 μm band in CZ and FZ silicon is 10^{16} cm^{-3} and 5 x 10^{16} cm^{-3} respectively. Due to its substitutional position, the diffusion of carbon requires intrinsic point defects, i.e, silicon interstitials and vacancies. Since the carbon atom is smaller than silicon atom, it contracts the silicon lattice.

2.3.5.1 Defects Related to High Energy Irradiation

Irradiation (1-2 MeV electron) of silicon will produce self-interstitials and vacancies.

Both primary defects are mobile at 100°K in intrinsic material. There is no evidence that carbon atoms interact with mobile vacancies. But a self-interstitial may displace a substitutional carbon atom resulting in the carbon being ejected into a bonded interstitialcy configuration C_i [Watkins 76]. It gives rise to local vibrational modes (LVM) absorption lines at 921 and 930 cm^{-1}. In photoluminescence or absorption measurement C_i is identified by the electronic transition at 856 meV [Woolley 87]. This C_i is observed in DLTS measurements [Kimerling 78], to act as a donor-like hole trap with the activation energy of hole emission of 0.28eV and an acceptor level with the activation energy of electron emission of 0.12 eV. The isolated interstitial carbon atom C_i is thermally stable up to about 300K in both FZ and CZ silicon, but after this it is different in the two materials. ***In oxygen free FZ*** silicon it then will be trapped by a substitutional carbon forming C_iC_s complex center that produces electronic absorption [Newman 71] and photoluminescence at 969 meV but no LVM absorption. The structure of this defect is suggested to be C_s-Si_i-C_s [O'Donnell 83]. ***In oxygen rich CZ*** silicon the interstitial carbon atom can be trapped by an oxygen atom and its complexes. The most prominent defect gives rise to absorption lines at 865 cm^{-1}, 1115 cm^{-1}, 529 cm^{-1}, 550 cm^{-1}, and 742 cm^{-1} [Newman 71]. The G15 paramagnetic resonance [Lee 77] and the 790 meV vibronic band [Noonan 76] are also ascribed to this complex. The defect is suggested to be interstitial carbon complexing with oxygen atom at distorted substitutional sites C_i - O_i [Deleo 84]. This defect also shows IR electronic absorption and Photoluminescence at 790 meV [Robbins 85]. When the dose of the 2 MeV electron irradiation is increased, this defect increases, reaching a maximum and then falls with the observation of a new defect involving capturing silicon interstitials [Oates 85]. As the total fluence is increased a wealth of PL and electronic absorption spectra from a whole range of defects involving both oxygen and carbon forms [Davies 84]. In

the very heavy irradiation condition the C_s line totally disappears without any SiC precipitate related absorption appearing [Brozel 74]. A similar effect is observed in C implanted into silicon samples prior to annealing [Stein 71]. Newman suggests that the irradiation-induced high concentrations of carbon interstitials promote clustering into graphitic inclusions that do not produce infrared absorption [Newman 81].

2.3.5.2 Defects Related to Heat Treatments

At high temperatures (>1000°C) in CZ silicon when interstitial oxygen atoms precipitate, SiC particles form around dislocation lines where SiO_2 particles have nucleated. Oxygen precipitation leads to the generation of self-interstitials and they may be trapped by carbon atoms and could diffuse at a very high rate [Newman 60]. The precipitated silicon carbide is detected by IR absorption at 12.2 μm rather than 12.6 μm of the bulk βSiC and is very much broadened. These effects are due to the small size of the βSiC particles and the fact that they are embedded in the silicon matrix [Bean 71]. In FZ silicon, high temperature treatments appear to have little effect unless dislocations are present, or nucleation sites are provided by a prior heat treatment or irradiation [Newman 83].

Thermal donor formation (450°C) is found inhibited when a high concentration of carbon is present because the self interstitials are trapped by carbon atoms [Helmreich 77]. But neither the TDs nor the effect of the carbon on their formation rate is clearly understood.

2.3.5.3 Carbon Related Microdefects

High concentration of carbon can have remarkable effect on the formation of microdefects during the growth of crystals. Carbon can trap silicon self-interstitials during solidification of the crystal to form a defect termed B defect. The aggregation of B defects and the larger A defects have been termed 'swirl defects' [Ravi 81] as mentioned earlier. Carbon containing sites can also function as a preferential nucleating agent for secondary defects such as dislocations, stacking faults and precipitates when subjected to heat treatment.

2.3.5.4 Influence of Carbon on Gold Diffusion

It is found that in FZ silicon the gold concentration is about twice as high in the regions of the maxima of carbon fluctuations as compared to the regions of minimal carbon concentration [Hill 77]. This effect is explained in terms of the kick-out diffusion mechanism of gold in silicon [Frank 84]. Within this mechanism gold on substitutional sites (Au_s) is incorporated via the kicking-out of a self interstitial (I) by the fast diffusing interstitial gold (Au_i). In carbon-rich silicon a high concentration of microdefects is present [Foll 81]. These microdefects act as sinks for self interstitials and lead to an increased rate of Au_s incorporation through: $Au_s \rightleftharpoons Au_i + I$.

2.3.6 Transition Metal Related Defects in Silicon

Transition metal impurities represent a class of defect whose properties are markedly

different from the rest of the family of deep impurities. Self consistent calculations of the deep levels introduced by interstitial, substitutional transition metals and small, well defined complexes show the energy levels are generally host-like electron states shifted into the gap by the impurity atom [Zunger 86]. However no deep levels are found from large transition metal clusters or precipitates because the valence electrons of them are too dissimilar from the host states. Heavy metals such as Au and Pt have predominant substitutional solubility and they are generally observed in supersaturated condition. Transition metals of the 3d series prefer interstitial lattice sites among which the fastest diffusing interstitial transition metals Co, Ni and Cu can not be retained in the interstitial site at room temperature, so that no energy levels can be determined for the dominant interstitial atoms. All transition metals in silicon analyzed so far have donor levels, so that they experience Coulomb attraction from acceptors in p-type silicon resulting in the formation of donor-acceptor complexes whose energy levels may be confused with those of isolated species. However the situation is improved with the help of EPR measurements [Weber 83b]. Table 2.1 lists those deep levels which are ascribed to specific species [Weber 88]. Energy levels for Co, Ni and Cu have not been included in Weber's review because of uncontrolled contamination which may confuse the issue. However there is some evidence that the levels at "E_c- 0.41 eV" and "E_v + 0.21 eV" might be due to substitutional Co [Kitagawa 85] and the levels at "E_c- 0.43 eV" and "E_v + 0.16 eV" [Kitagawa 87] might be due to substitutional Ni. Brotherton [Brotherton 87] reports four Cu related deep levels at "E_v+0.09 eV", "E_v+0.23 eV", "E_v+0.42 eV" and "E_c- 0.16 eV". Photoluminescence band at 1014 meV is assigned to Cu. Actually the best established PL from a transition metal is that from Cu [Watkins 82].

Metal	level type	E: activation energy	T: eg K (e=100/s)
Ti(i)	-/o	0.08	
	o/+	0.26	152
	+/++	0.290	182
V(i)	-/o	0.16	109
	o/+	0.45	148
	+/++	0.47	246
Cr(i)	o/+	0.22	
Mn(i)	-/o	0.11	
	o/+	0.43	201
	+/++	0.32	200
Mn(s)	o/+	0.35	202
Fe(i)	o/+	0.425	244
Au(s)	-/o	0.553	272
	o/+	0.345	160
Pt(s)	-/o	0.231	122
	o/+	0.321	170

Table 2.1 List of DLTS parameters of transition metals *After Weber [Weber 88]*

References

[Asom 87] Asom M. T., Benton J. L., Sauer R. and Kimerling L. C., *Appl. Phys. Lett. 51*, 1987, pp 25

[Baraff 80] Baraff G. A., Kane E. O. and Schluter S., *Phys. Rev. B(USA) 21*, 1980, pp 3563

[Bean 71] Bean A. R. and Newman R. C., *J. Phys. Chem. Solids, 32*, 1971, pp 1211

[Berg 92] Berg A., Brough I., Evans J. H., Lorimer G. and Peaker A. R., *Semicond. Sci. and Technol., 7*, 1992, pp A263

[Brozel 74] Brozel M. R., Newman R. C., Totterdell D. H. J., *J. Phys. C(GB), vol 7*, 1974, pp 243

[Bourret 84] Bourret A., Thibault-Desseaux J. and Seidmann D. N., *J. Appl. Phys., 55*, 1984, pp 825

[Brotherton 82] Brotherton S. D. and Bradley P., *J. Appl. Phys., vol. 3 no. 8*, 1982, pp 5720

[Brotherton 87] Brotherton S. D., Ayres J. R. and Gill A., *J. Appl. Phys., 62 (5)*, 1987, pp 1826

[Burgers 39] Burgers, *J. M., Proc. Kon. Ned. Akad. Wet.42* (Amsterdam, 1939), pp 293,

[Cockayne 69] Cockayne D. J. H., Ray I. L. F., Whelan M. J., *Philos. Mag. (GB), 20*, 1969, pp 1265

[Davies 84] Davies G., Lightowlers E. C., Wooley R., Newman R. C. and Oates A. S., *J. Phys. C: Solid St. Phys., 17*, 1984, pp L499

[Deleo 84] Deleo G. G., Fowler W. B. and Watins G. D., *Phys. Rev., B29*, 1984, pp 3193

[Drozdov 76] Drozdov N. A., Patrin A. A. and Tkachev V. D., *Sov. Phys. JETP Lett., 23*, 1976, pp 597

[Evans 9?] Evans J. H., Kaniewski J. and Kaniewska M., *Semi. Sci. Tech., 7(1A)*, 1992, pp A41

[Fair 85] Fair R. B., Pearce C. W. and Washburn J., *Impurity Diffusion and Gettering in Silicon*, Materials Research Society, 1985

[Foll 81] Foll H., Gosele U. and Kolbesen B. O., *J. Cryst. Growth*, 40, 1977, pp 90

[Frank 84] Frank W., Gosele U., Mehrer H. and Seeger A., *Diffusion in Crystalline Solids*, Murch G. E. and Norwich A. S., eds. (Academic Press, New York, 1984), pp 63

[Fuller 54] Fuller C. S., Ditzenberger J. A., Hanney N. B. and Buehler E., *Phys. Rev. 96*, 1954, pp 833

[Gaworzewski 84] Gaworzewski P., Hill E., Kirochi F. G. and Vecserny'es L., *Phys. Status Solidi 85*, 1984 pp 133

[Helmreich 77] Helmreich D. and Sirtl E., Semiconductor Silicon 1977, Proc. 3rd Int. Sym. on silicon Mat. Sci. and Tech. eds. Huff H. R. and Sirtl (New York: Electrochem. Soc.) 1977, pp L967

[Higgs 90] Higgs V., Lightowlers E. C. and Kightley P., in *Impurities, Defects and Diffusion in Semiconductors*: Bulk and Layered Structures, edited by Wolford J., Bernholc J. and Haller E. E. (Materials Research Society, Pittsburgh, PA), 1990, pp 57

[Hill 77] Hill M. J. and van Isegam P. M., *Semiconductor Silicon*, eds. Huff H. R. and Sirtl E., 1977, pp 715

[Hirth 68] Hirth J. P. and Lothe J., *Theory of Dislocations* (McGraw-Hill, New York, USA, 1968, pp 356

[Hölzlein 86] Hölzlein K., Pensl G. Schulz M., and Johnson N. M., *Appl. Phys. Lett., 48*, 1986, pp 916

[Hornstra 58] Hornstra J., *J. Phys. Chem. Solids, 5*, 1958, pp 129

[Hsieh 73] Hsieh, C. M., and D. M. Maber, *J.Appl.Phys., vol. 44, no.3*, 1973, pp 1302

[Hu 80] Hu S. M., *Appl. Phys. Lett.* 36, 1980, pp 561

[Huff 85] Huff H. R. and Shimura F., *Solid State Technol.*, March 1985, pp 103

[Hwang 86] Hwang J. M., *J. Appl. Phys., 59(7)*, 1986, pp 2476

[Inoue 82] Inoue N., Osaka J. and Wada K., *J. Electrochem. Soc. 129*, 1982, pp 2780

[Inoue 86] Inoue N., Wada K. and Osaka J. in oxygen in silicon ed. by Chikawa J., Sumino K., and Wada K. in *Defects and Properties of Semiconductors: Defect Engineering*, (Scientific Publishers,

1986), KTK pp 197

[Jaros 82] Jaros, M., *Deep Levels in Semiconductors,* Adam Hilger, Bristol, 1982

[Johnson 59] Johnson F. A., *Proc. Phys. Soc., London (GB), 73,* 1959, pp 265

[Johnson 79] Johnson N. M., Bartelink D. J. and McVittie J. P., *J. Vac. Sci. Technol., 16,* 1979, pp 1407

[Kaiser 58] Kaiser W., Frisch H. L. and Reiss H., *Phys. Rev. 112,* 1958, pp 1546

[Kaniava 94] Kaniava A., Vanhellemont J., Simoen E. and Claeys C., *Semi. Sci. Tech., 9(8),* 1994, pp 1474

[Kaniewski 92] Kaniewski J., Kaniewska M. and Peaker A. R., *Appl. Phys. Lett. 60(3),* 1992, pp 359

[Kawado 80] Kawado S., *Jpn. J. Appl. Phys., 19,* 1980 pp 1591

[Kimerling 77] Kimerling L. C., *Inst. Phys. Conf. Ser. (GB) no. 31* Eds. Urli N. B. and Corbett J. W., London, 1977, pp 221

[Kimerling 78] Kimerling L. C., Blood P. and Gibson W. M., *Defects and Radiation Effects in Semiconductors, 1978, Inst. Phys. Conf. Ser., 46,* pp 273

[Kimerling 79] Kimerling L. C. and Patel J. R., *Appl. Phys. Lett., 34,* 1979, pp 73

[Kimerling 80] Kimerling L. C. and Chantre A., *Appl. Phys. Lett. 48,* 1980, pp 1000

[Kimerling 81] Kimerling L. C. and Benton J. L., *Appl. Phys. Lett. 39,* 1981, pp 410

[Kimerling 85] Kimerling, L. C. and Patel, J. R in *VLSI Electronics vol.12: Microstructure and Science* (Academic Press Inc., Orlando, 1985), pp 223

[Kirkpatrick 76] Kirkpatrick C. G. and Noonan J. R., *Rad Effects 30,* 1976, pp 97

[Kishino 82] Kishino S., Matsushita Y., Kanamori M. and Iizuka T., *Jpn. J. Appl. Phys. 21,* 1982, pp 1

[Kitagawa 85] Kitagawa H., Nakashima H. and Hashimoto K., *Jpn. J. Appl. Phys. Part 1, vol 24 no. 3,* 1985, pp 373

[Kitagawa 87] Kitagawa H. and Nakashima H., *Phys. Status Solidi a (Germany) vol. 102 no. 1*, 1987, pp K238

[Kveder 82] Kveder V. V., Osipyan A. Yu., Schröter W. and Zoth G., *Phys. Stat. Sol. (a) 72*, 1982, pp 701

[Lee 77] Lee Y-H, Corbett J. W. and Brower K. L., *Phys. Status Solidi a 41a*, 1977, pp 637

[Liang 80] Liang A. Y. and Varker C. J., in Lifetime factors in Silicon, *ASTM, STP 712*, 1980, pp 73

[Lightowlers 89] Lightowlers E. C., Higgs V., Gregson M. J., Davies G., Davey S. T., Gibbings C. J., Tupper C. G., Schaffler F. and kasper, *Thin Solid Films*, 183, 1989, pp 235

[Lightowlers 94] Lightowlers E. C., Jeyanathan L., Safonov A. N., Higgs V. and Davies G., *Mater. Sci. Eng. B, vol. 24, no. 1-3*, 1994, pp 144

[Long 68] Long, D., Energy Bands in Semiconductors, Wiley (Interscience), New York, 1968

[Matlock 83] Matlock J. H., *Defects in Silicon*, edited by Bullis W. M. and Kimerling L. C. (Electrochemical Society, Pennington, NJ), 1983, pp 3

[Mikkelsen 86] Mikkelsen J. C., *Mater. Res. Soc. Symp. Proc. (USA), vol. 59*, 1986, pp 19

[Miyagi 82] Miyagi M., Wada K., Osaka J. and Inoue N., *Appl. Phys. Lett. 40*, 1982, pp 719

[Newman 60] Newman R. C., *Proc. Phys. Soc. London, 76*, 1960, pp 993

[Newman 65] Newman R.C. and Willis J. B., *J. Phys.& Chem. Solids (GB), 26*, 1965, pp 133

[Newman 71] Newman R. C. and Bean A. R., *Rad. Effects, 8*, 1971, pp 189

[Newman 81] Newman R. C. in Neutron Transmutation Doped Si, Ed. Guldberg J., 1981, pp 83

[Newman 83] Newman R. C., Oates A. S. and Livingston F. M., *J. Phys. C: Solid St. Phys., 16*, 1983, pp L667

[Noonan 76] Noonan J. R., Kirkpatrick C. G. and Streetman B. G., *J. Appl. Phys. 47*, 1976, pp 3010

[Oates 85] Oates A. S., Newman R. C., Woolley R., Davies G., Lightowlers E. C., Binns M. J. and Wilkes J. G., *Appl. Phys. Lett., 47*,1985, pp 705

[O'Donnell 83] O'Donnell K. P., Lee K. M. and Watkins G. D., *Physica 116B*, 1983, pp 258

[Oehrlein 82] Oehrlein G. S., Lindstrom J. L., and Corbett J. W., *Appl. Phys. Lett. 40,* 1982, pp 241

[Omling 85] Omling P., Weber E. R., Montelious L. and Alexander H. M., *Phys. Rev. B, vol. 32,* 1985, pp 6571

[Ono 85] Ono H. and Sumino K., *J. Appl. Phys. 57 (2)*, 1985, pp 87

[Ourmazd 84] Ourmazd A., Schroter W., Bourret A., *J. Appl. Phys. 56,* 1984, pp 1670

[Peaker 83] Peaker A. R., Craven R. A. and Shaw R. W., *J. Electrochem. Soci., 13(8)*, 1983, pp C328

[Peaker 87] Peaker A. R. and Guimaries S., in *Properties of Silicon, EMIS Datareviews Series No.4* (INSPEC, London), *RN=17835*, 1987, pp 225

[Peaker 89] Peaker A. R., Hamilton B., Lahiji G. R., Ture I. E. and Lorimer G., *Mater. Sci. Eng. B 4*, 1989, pp 123

[Ravi 81] Ravi K. V., *Imperfections and Impurities in Semiconductor Silicon* (John Wiley & Sons, New York, USA, 1981) pp 62

[Ravi 88a] Ravi, K. V., N. Hecking, W. Fengmei, Z. Xiangqing and L. N. Aleksandrov, in *Properties of Silicon, EMIS Datareviews Series No. 4* (INSPEC, London, 1988), pp 245

[Ravi 88b] Ravi K. V., in *Properties of Silicon, EMIS Datareviews Series No.4* (INSPEC, London), 1988, pp 1060

[Reiche 88] Reiche M., Reichel J. and Nitzsche W., *Phys. Status Solidi A 107*, 1988, pp 851

[Robbins 85] Robbins D. J., Gasson D. B., Hardeman R. W. and Pitt A. D., *Proc. Symp. on Reduced Temperature Processing for VLSI (Electrochem. Soc., Las Vegas)*, 1985, pp159

[Rostoworoski 81] Rostoworoski J. A. and Parsons R. R., *Can. J. Phys., 59*, 1981, pp 496

[Shockley 52] Shockley W., Read W. T. *Phys. Rev. 87*, 1952, pp 835

[Schröter 89] Schröter W., Queisser I. and Kronewitz J., *Inst. Phys. Conf. Ser. no. 104*, 1989, pp 75

[Shimura 89]] Shimura, F., *Semiconductor Silicon Crystal Technology* (Academic Press Inc., San Diego, 1989)

[Skolnick 81] Skolnick M. S., Collis A. G. and Weber H. C., *J. Lumin., 24/25*, 1981, pp 39

[Steele 87] Steele A. G., Thewalt M. L. W. and Watkins S. P., *Solid State Commun. 63*,1987, pp 81

[Stein 71] Stein H. J. in Proc. 2nd Int. Conf. *Ion Implantation in Semiconductors* (Springer Verlag), 1971 pp 2

[Suezawa 84] Suezawa M. and Sumino K., *Phys. Stat. Sol. a83*, 1984, pp 235

[Tajima 81] Tajima M., Matsui T. Abe T. and Iizuka T., *Semiconductor Silicon*, 1981, pp 72

[Tajima 83] Tajima M., Gösele U., Weber J. and Sauer R., *Appl. Phys. Lett.*, 43(3), 1983, pp 270

[Takano 73] Takano Y. and Malei M., in *Semicon. Silicon* eds. Huff H. R. and Burgess R. B. (Electrochem. Soc., Princeton, 1973), pp 469

[Takano 81] Takano Y., Kozuka H., Ogirima M. and Maki M., *Semiconductor Silicon*, 1981, pp 743

[Takaoka 79] Takaoka H., Oosaka J. and Inoue N., *Jpn. J. Appl. Phys. Suppl. 18-1*, 1979, pp 179

[Tempelhoff 79] Tempelhoff K., Spiegelberg F., Gleichmann R. and Wruck D., *Phys. Status Solidi a(56)*, 1979, pp 213

[Thewalt 86] Thewalt M. L. W., Steele A. G., Watkins S. P. and Lightowlers E.C., *Phys. Rev. Lett., 57* 1986, pp 5695

[Tkachev 77] Tkachev V. D. and Mudryi A. V., *Inst. Phys. Conf. Ser., 31*, 1977, pp 231

[Uebbing 80] Uebbing R. H., Wagner P., Buamgart H. and Quiesser H. J., *Appl. Phys. Lett., 37*, 1980, pp 1078

[Wada 80] Wada K., Inoue N. and Kohra K., *J. Cryst. Growth, 49*, 1980, pp 749

[Wada 82] Wada K., Nakanishi H., Takaoka H. and Inoue H., *J. Cryst. Growth 57*, 1982, pp 1535

[Wada 84] Wada K., *Phys. Rev.,B30*, 1984, pp 5884

[Watkins 61] Watkins G. D. and Corbett J. W., *Phys. Rev. vol. 121 no. 4*, 1961, pp 1001

[Watkins 65] Watkins G. D. and Corbett J. W., *Phys. Rev., 138*, 1965, pp A543

[Watkins 64a] Watkins G. D., *Radiation Damage in Semiconductors* (Dunod, Paris, 1964), pp 67

[Watkins 64b] Watkins G. D. and Corbett J.W., *Phys. Rev., vol. A134*, 1964, pp1359

[Watkins 75] Watkins G. D., *Lattice Defects in Semiconductors (Inst. Phys. Conf. Ser., 23*, London), 1975, pp 1

[Watkins 76] Watkins G. D. and Brower K.L., *Phys. Rev. Lett., 36*, 1976, pp 1329

[Watkins 82] Watkins S. P., Ziemelis U. O. and Thewalt M. L. W., *Solid State Commun. 43*, 1982, pp 687

[Weber 83a] Weber E. R. and Alexander H., *J. Phys. Colloq. (France) vol. 44 no. C-4*, 1983, pp 319

[Weber 83b] Weber E. R., *Appl. Phys. A (Germany) vol. 30 no. 1*, 1983, pp 1

[Weber 88] Weber E. R., *in Properties of Silicon, EMIS Datareviews Series No.4* (INSPEC, London), RN=17890, 1988, pp 236

[Whan 67] Whan R. E. and Vook F. L., *Phys. Rev., 153*, 1967, pp 814

[Woolley 87] Woolley R. A., Lightowlers E. C., Tipping A. K., Claybourn M. and Newman R. C., *Mater. Sci. Forum 10-12*, 1987, pp 929

[Wörner 86] Wörner R. and Schirmer O. F., *Phys. Rev. B34*, 1986, pp 1381

[Wruck 79] Wruck D. and Gaworzewski P., *Phys. Stat. Sol. a56*, 1979, pp 557

[Yang 78] Yang K. H., Kappert H. F. and Schwuttke G. H., *Phys. Stat. Sol., A50*, 1978, pp 221

[Yasutake 82] Yasutake K., Umeno M., Kawabe H., Nakayama H., Nishino T. and Hamakawa Y., *Jpn. J. Appl. Phys., 21*, 1982, pp 28

[Zulehner 82] Zulehner, W., and D. Huber, in *Crystals 8: Silicon-Chemical*

Etching, ed. J.Grabmaier (Springer-Verlay, Berlin, 1982), pp 1

[Zunger 86] Zunger A., *Solid State Phys.* (USA), 39, 1986, pp 275

Chapter 3 Characterization Techniques of Defects

3.1 Deep Level Transient Spectroscopy (DLTS) and Related Techniques

3.1.1 Introduction

The principal use of semiconductors is in devices which rely on their electronic properties for operation. Probing impurities and defects directly by electrical techniques can provide the primary information for the design, development and manufacture of devices. Electronic effects of defects are determined not only by their chemical identity but also by a variety of other factors such as their site location and bonding in the crystal lattice, by interaction with other defects and with impurities and by other electrical effects such as their charge state and local electric fields. One good example is given in the review by Peaker [Peaker 89a] showing when boron doped p-type silicon is irradiated with 1 MeV electrons at reduced temperature the boron is displaced from its substitutional site and located interstitially. It is no longer a shallow acceptor but is a deep electron trap with donor-like properties. If the sample is then heat treated at different temperatures different complexes form resulting from defect reactions. These defects have electronic states deep in the silicon band gap and can be detected using electronic methods but the changes are not observed in chemical analysis techniques, for example Secondary ion mass spectroscopy (SIMS). In materials where carrier generation or recombination have significant influence on device functionality, for example, the speed of response of certain devices, deep state levels should be tightly

controlled. The best known technique which can measure the electrical activity of deep defects and impurities of low density is deep level transient spectroscopy (DLTS) [Lang 74]. It utilizes a space-charge region of a p-n junction or a Schottky barrier which is essentially depleted of mobile carriers to examine the emission and capture of carriers from deep states in terms of their concentrations, energy levels and capture rates. The capacitance version of this technique is able to distinguish between majority and minority carrier traps and present the results spectroscopically. Furthermore since the measurements can be done on as-grown slices or on materials and devices at various stages of processing, it provides a very convenient in-line check for degradation in device performance as a result of processing variations or contamination and can often be done on an actual production device. In this section before we concentrate on DLTS technique we will first study the capacitance associated with the depletion region of a Schottky barrier or an abrupt p-n junction. This is because not only itself can provide extensive information about shallow dopants as well as deep states but also it is the basis of DLTS technique.

3.1.2 Capacitance-Voltage Measurement

3.1.2.1 Properties of p^+n junctions/Schottky barriers in the Absence of Deep Defect States

Consider an abrupt p^+n junction (or a n-type Schottky barrier) under reverse bias. For such structures the depletion region is predominantly in the low-doped material (in the semiconductor for the Schottky barrier case). The width W of this depletion region is

obtained using Poisson's equation. For uniformly doped material we have:

$$W=\sqrt{\frac{2\varepsilon(V_{bi}+V-\frac{kT}{q})}{q(N_D-N_A)}} \tag{3.1}$$

where ε is the dielectric constant of the (depleted) semiconductor material, V_{bi} is the built-in voltage of the junction, V is the externally applied bias voltage, k is Boltzmann's constant, T is the absolute temperature, q is the charge on the electron and $(N_D - N_A)$ is the net ionized impurity concentration in the lightly doped material. Under the depletion approximation the small signal capacitance associated with the depletion region is given by:

$$C=\frac{\varepsilon A}{W} \tag{3.2}$$

here A is the area of the junction. This expression is identical to the expression for a parallel plate capacitor, comprising a layer of dielectric of thickness W and dielectric constant ε between two conducting electrodes. The capacitance of this voltage-variable capacitor decreases monotonically with increasing bias voltage before electrical breakdown. From equations (3.1) and (3.2) we obtain (for uniformly doped material):

$$C=A\sqrt{\frac{\varepsilon q(N_D-N_A)}{2(V_{bi}+V-kT/q)}} \tag{3.3}$$

A plot of C^{-2} versus reverse bias V is linear in this case and has a slope proportional to $(N_D - N_A)$. V_{bi} can be found from the intercept. For non-uniformly doped material, still assuming depletion approximation, using Poisson's equation and Gauss' law we can derive the expression for the local doping density $(N_D - N_A)$ as a function of depth:

$$(N_D - N_A) = \frac{-C^3}{q\varepsilon A^2}\left(\frac{\Delta C}{\Delta V}\right)^{-1} \tag{3.4}$$

This equation, in conjunction with equation (3.2) forms the basis for junction profiling measurements. For a practical material, the depletion edge is not abrupt and there exists a natural limitation to the spatial resolution characterized by local Debye length L_D:

$$L_D = \sqrt{\frac{\varepsilon kT}{q^2(N_D - N_A)}} \tag{3.5}$$

here $(N_D - N_A)$ represents the free carrier density at the location of interest. The Debye length is also indicative of the abruptness of charge distribution near the depletion edge. The free carrier density n(x) which falls off at distance x from the depletion edge is given by:

$$n(x) \approx n_o e^{-x^2/2L_D^2} \tag{3.6}$$

Here n_o is the free carrier density of the bulk material. It is this tail of free carriers that gives a finite equilibrium population probability for deep traps in that portion of the

depleted region.

3.1.2.2 Effects of Deep Defect States on p^+n Junctions/Schottky Barriers

3.1.2.2.1 Influence on Junction Structures

The energy band diagrams for a p^+n junction under reverse bias containing N_D shallow donors and N_T deep levels with thermal emission rate e_n and energy level E_T are shown in Figure 3.1, (a) for donor-like traps and (b) for acceptor-like traps [Kimerling 74]. y is the crossing point of E_T and the Fermi level E_F. E_C and E_V are conduction and valence band edge respectively. The structure contains three regions in the depletion layer. $y < x < W$ region and is often referred to as the transition region λ, in which generation-recombination processes are active in determining the equilibrium occupation of defect states. For uniformly doped material the transition region is expressed as:

$$\lambda = W - y = \sqrt{\frac{2\varepsilon(E_F - E_T)}{qN_D}} \tag{3.7}$$

The region $0 < x < y$ is totally depleted of mobile carriers in which defect state occupation is controlled only through emission processes. The region $x > W$ is neutral material.

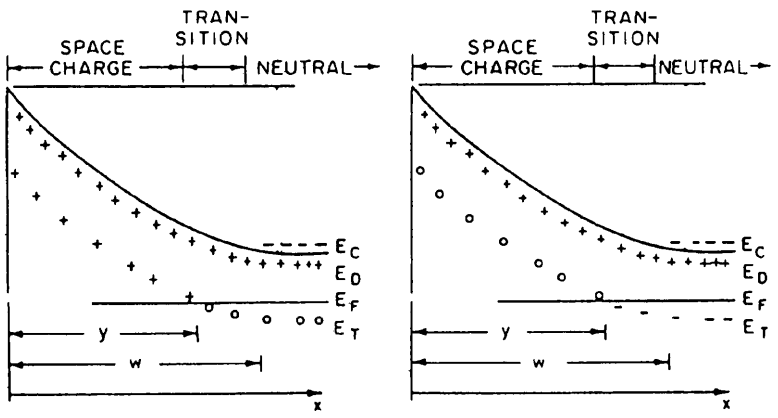

Figure 3.1 Electronic structure of a reverse biased p^+n junction with one deep trap (a) deep donor traps (b) deep acceptor traps

3.1.2.2.2 Influence on Measured Capacitance in Relation to Temperature/Frequency

The capacitance C is normally measured at a fixed voltage V by superimposing a small oscillating voltage ΔV_{osc} on the applied bias. This small signal capacitance is obtained by measuring the current induced by the oscillating voltage. Two localized components of the charge fluctuation should be considered, refer to Figure 3.1, one at the depletion layer edge W due to the shallow donors which always follow the test signal, and another at y due to the deep states which may or may not follow the test signal, depending on the relative magnitude of the defect emission rate e_n and the measurement frequency ω. This frequency effect can be used to detect defect states by observing steps in capacitance versus frequency behavior. Because the capture rates (c_n) and emission rates of defect states are temperature dependent, monitoring the junction capacitance while vary the temperature at a constant frequency can provide the similar

information (bearing in mind that temperature variation also affects the equilibrium Fermi level). Detailed discussions can be found in reference [Miller 77]. Figure 3.2 is a diagram taken from this reference showing the junction (containing a deep defect state) capacitance change as a function of temperature at two measurement frequencies. Two capacitance steps are observed for a given set of conditions corresponding to processes in the space charge region (low temperature) and transition region (higher temperature):

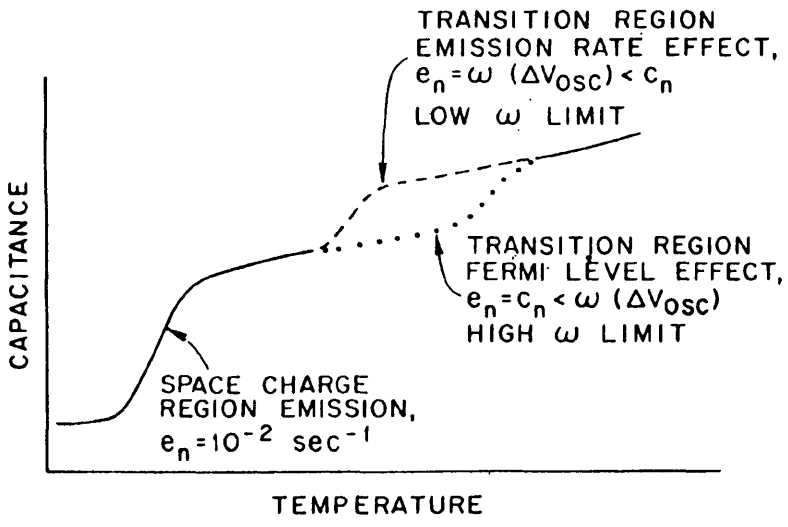

Figure 3.2 Capacitance versus temperature behavior of a p^+n junction containing a deep defect state in the upper half of the energy gap.
After Miller [Miller 77]

3.1.2.2.3 Influence on Free Carrier Distributions

Refer to equation (3 4) the free carrier depth distribution is determined by measuring the junction capacitance C as a function of the reverse bias V. When we measure the free carrier density at depletion edge W we have assumed no contributions from the deep levels. However complication arises dependent on the relative magnitude of the change frequency of the applied voltage ($\omega(\Delta V)$) and the emission rate of the defects (e_n). Assuming a measurement frequency $\omega(\Delta V_{osc})$ higher than both of them (which are the common cases), there exists two situations to be considered [Kimerling 74] (assuming uniform material):

$\omega(\Delta V_{osc}) > \omega(\Delta V) > e_n$: In this case the measured result corresponds to the true bulk free carrier distribution.

$\omega(\Delta V_{osc}) > e_n > \omega(\Delta V)$: Refer to Figure 3.1(a) with deep donors, assume $n_m(W)$ is the measured free carrier density at W, according to Gauss's law:

$$\Delta E = \frac{\Delta Q}{\varepsilon} = \frac{q n_m(W) \Delta W}{\varepsilon} \tag{3.8}$$

and we have:

$$\Delta E = \frac{\Delta V}{W} \tag{3.9}$$

from equations (3.8) and (3.9) we have:

$$n_m(W)=\frac{\varepsilon \Delta V}{qW\Delta W} \tag{3.10}$$

From the definition of small signal capacitance:

$$C=\frac{\Delta Q}{\Delta V} \tag{3.11}$$

and combine with equation (3.2) we obtain:

$$\Delta V=\frac{\Delta Q(y)}{C(y)}+\frac{\Delta Q(W)}{C(W)}=\frac{q}{\varepsilon}[N_T(y)y\Delta y+n(W)W\Delta W] \tag{3.12}$$

where n(W) is the actual free carrier concentration at W. From equations (3.10) and (3.12) and for a homogeneous background doping $\Delta W = \Delta y$, we have:

$$n_m(W)=N_T(y)\frac{y}{W}+n(W) \tag{3.13}$$

As an example Figure 3.3 shows the measured free carrier profiles for an actual (a) homogeneous (b) inhomogeneous distributions of deep donors, based on equations (3.13).

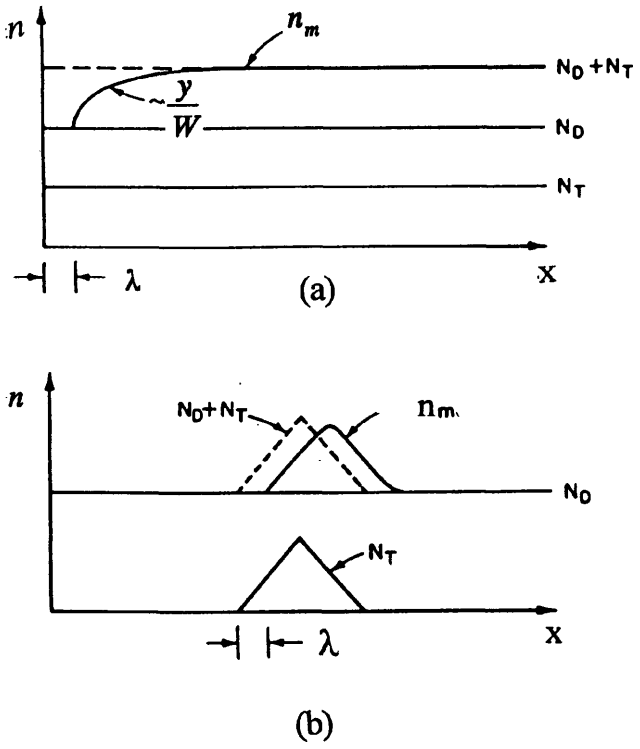

Figure 3.3 Measured free-carrier profiles of an actual
(a) homogeneous
(b) inhomogeneous distribution of deep donor traps. *After Kimerling [kimerling 74]*

Similarly, refer to Figure 3.2 (b) for deep acceptor level case we have:

$$n_m(W)=N_T(y)\frac{y}{W}+n(W)-N_T(W) \tag{3.14}$$

This situation is illustrated in Figure 3.4 of an actual (a) homogeneous (b) inhomogeneous distributions of deep acceptors, based on equations (3.14).

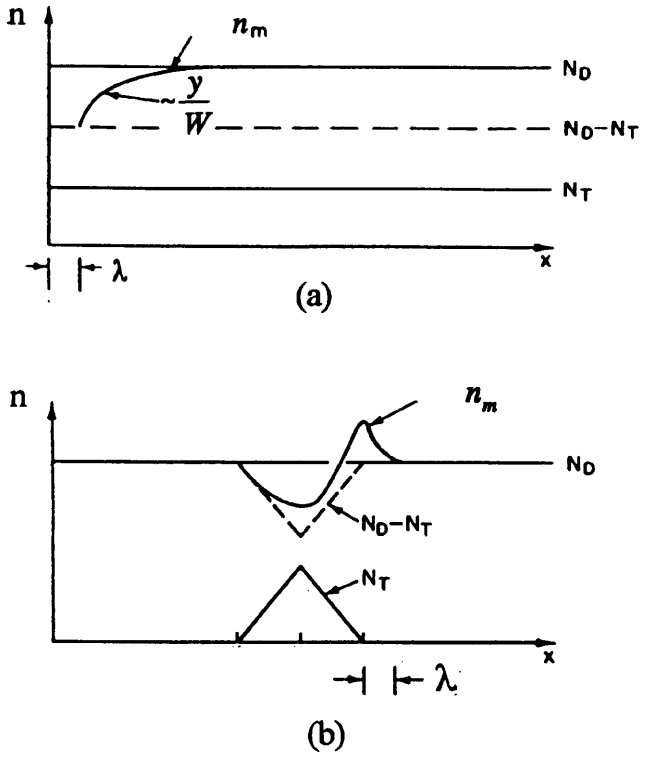

Figure 3.4 Measured free-carrier profiles for
(a) homogeneous
(b) inhomogeneous distribution of deep acceptor traps. *After Kimerling [Kimerling 74]*

3.1.3 DLTS Technique

3.1.3.1 Theoretical Background of DLTS Technique

3.1.3.1.1 Introduction

Deep states are those which are positioned deeper than the corresponding hydrogenic

states in the band gap. The carrier wave function near the defect site is localized in real space but is extended in k-space. This allows the defect to couple to a large variety of phonons and enhances the throughput of excess carriers in indirect gap materials. Deep states tend to be nonradiative recombination centers. There are four processes which define the dynamic electronic behavior of a deep state, namely the individual emission and capture processes for electrons and holes. These processes are closely related to two different physical environments: the neutral (undepleted) material regime and the depletion region regime.

Neutral material regime: The main process happens in this regime is carrier capture. The electron capture rates (per unoccupied state) and hole capture rates are given by the respective expressions:

$$c_n = \sigma_n \langle v_n \rangle n \tag{3.15}$$

$$c_p = \sigma_p \langle v_p \rangle p \tag{3.16}$$

where σ_n and σ_p are capture cross sections for capturing electrons and holes respectively. n and p are the concentrations of electrons and holes respectively. $\langle v_n \rangle$ and $\langle v_p \rangle$ are the average thermal velocities of electrons and holes respectively, for the electrons it is given by:

$$\langle v_n \rangle \propto \sqrt{\frac{3kT}{m_e^*}} \tag{3.17}$$

where m_e^* is electron effective mass, k is Boltzmann's constant, and T is the absolute temperature. An analogous expression holds for holes. In the situation $c_n \gg c_p$ we say it is an **electron trap**, when $c_n \ll c_p$ it is a **hole trap**. We define a **recombination center** as a defect for which both the electron and hole capture rates are significant. However a deep state with a given capture cross section might be either a trap or a recombination center depending on the specific system it is in. For example, in a truly depleted region where there is no free carriers recombination can not occur so the deep states are traps and not recombination centers.

Depleted material regime: In this regime classification of deep states are defined in terms of their thermal emission properties. A **majority carrier trap** is defined as a deep state where the rate for thermal emission of a majority carrier e_{maj} is much larger than the corresponding rate for thermal emission of a minority carrier e_{min}. A **minority carrier trap** has the definition: $e_{min} \gg e_{maj}$. An electron trap is a majority carrier trap in n-type material and a minority carrier trap in p-type material. A **generation center** can be defined as the case where both e_n and e_p are significant so that it thermally emits both electrons and holes and thus can generate a steady state current in a depletion region. A generation center tends to be in the middle of the gap. The relationship between the emission and capture rate is obtained from the consideration of the occupancy of the trap in thermal equilibrium. Thermal emission rates for electrons are given by:

$$e_n = A_n \exp(-\Delta E/kT) \tag{3.18}$$

where ΔE is the activation energy of electron emission and A_n is a property of the particular defect, and may be evaluated by using the detailed balance principle which states that in equilibrium the carrier capture and emission for each electron state must be equal. Thus:

$$e_n p = c_n(1-p) \tag{3.19}$$

here p is the probability that the state is occupied. The electron concentration is given by:

$$n = N_c \exp[-(E_c - E_F)/kT] \tag{3.20}$$

where N_C is given by:

$$N_c = 2M_c\left(\frac{2\pi m_e^* kT}{h^2}\right)^{3/2} \tag{3.21}$$

h is Planck's constant and M_c is the number of equivalent conduction band minima. From equations (3.15), (3.18), (3.19) and (3.20) we obtain:

$$e_n = \frac{\sigma_n \langle v_n \rangle N_c}{g} \exp(-\Delta E/kT) \tag{3.22}$$

where g is the degeneracy factor. An analogous expression holds for hole emission with

the n subscripts replaced by p, N_C replaced by N_V (effective density of states of valence band) and ΔE is the activation energy of hole emission.

Figure 3.5 summaries the capture and emission processes at a deep state.

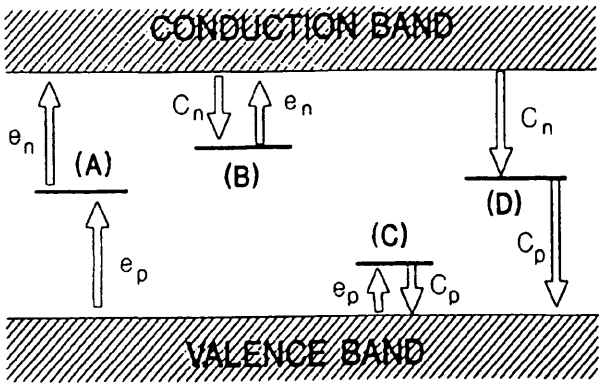

Figure 3.5 Summary of the capture and emission processes at a deep state

Unlike shallow hydrogenic levels, deep state centers may be occupied by more than one electron, therefore one deep state can have different energy levels according to its charge state. A donor-like state is defined as positive when not occupied and an acceptor-like state, neutral, when not occupied. The rate equation governing the occupation of a defect state of total concentration N_T is (exclude optically remove carriers):

$$\frac{dn_T}{dt} = a(N_T - n_T) - bn_T \tag{3.23}$$

where n_T is the concentration of defects occupied by electrons. And:

a = Σ rates of "electron gain" (e.g. c_n+e_p)

b = Σ rates of "electron loss" (e.g. c_p+e_n)

If we denote $n_T(0)$ as when t=0, then the general solution of equation (3.23) is:

$$n_T(t)=\frac{a}{a+b}N_T-[\frac{a}{a+b}N_T-n_T(0)]e^{-(a+b)t} \tag{3.24}$$

The general formula for the steady state occupation of a trap $n_T(\infty)$ is given by setting equation (3.23) to zero and we have:

$$n_T(\infty)=\frac{a}{a+b}N_T \tag{3.25}$$

we can rewrite equation (3.24) as:

$$n_T(t)=n_T(\infty)-[n_T(\infty)-n_T(0)]e^{-t/\tau} \tag{3.26}$$

where τ is the time constant given by:

$$\tau^{-1}=a+b=e_n+c_n+e_p+c_p \tag{3.27}$$

Consider the trap being initially filled at t=0, i.e. $n_T(0)=N_T$, we have the following solution:

$$n_T(t)=\frac{a}{a+b}N_T+\frac{b}{a+b}N_Te^{-(a+b)t} \tag{3.28}$$

For the case the trap is initially empty at t=0, i.e. n_T=0, we have:

$$n_T(t)=\frac{a}{a+b}N_T[1-e^{-(a+b)t}] \tag{3.29}$$

These two solutions are illustrated in Figure 3.6

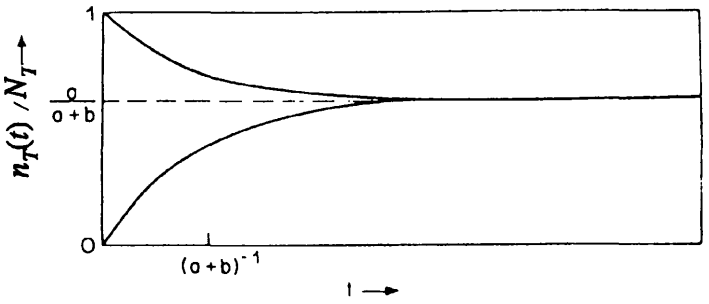

Figure 3.6 Schematic illustration of the solutions to equations (3.28) and (3.29)

3.1.3.1.2 Thermal Emission from Majority and Minority carrier Traps

Electronic transitions within the space charge region consist almost entirely of emission processes. Refer to Figure 3.7, initially the p^+n junction is under reverse bias (1). A bias pulse towards zero will momentarily collapse the space charge region, making majority carriers available for capture (2). When the pulse is turned off and reverse bias condition re-established, the junction capacitance is reduced because compensating majority carrier charge has been trapped in the space charge region (3). This charge can

subsequently be excited to the band and swept from the space charge region by the applied junction potential ④.

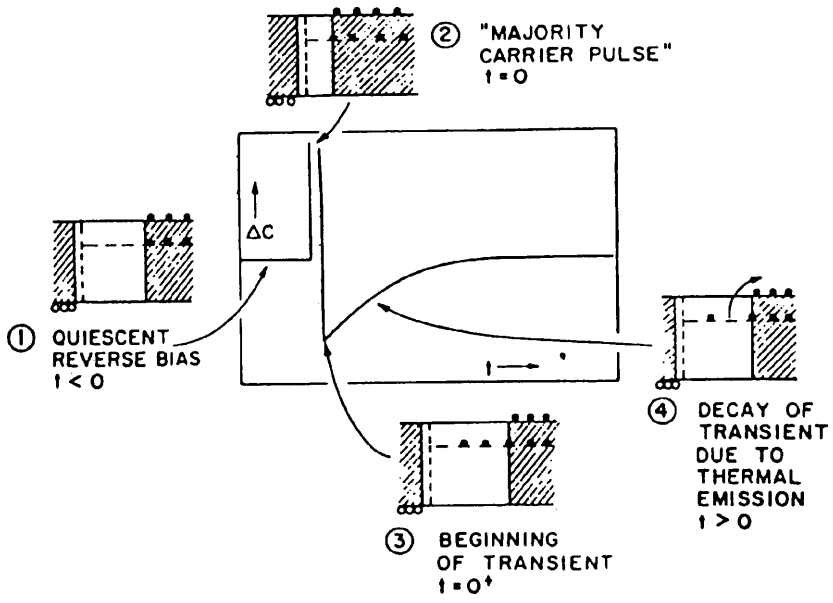

Figure 3.7 Capacitance transient due to a majority carrier trap emission in a p^+n diode.

Figure 3.8 illustrate the case for minority carrier trap emission. A pulse into forward bias is used to inject minority carriers. If a Schottky barrier structure is used, minority carrier injection should be introduced by a photon with energy $h\upsilon > E_g$ (bandgap energy) pulse (see section 3.1.3.1.3.3 MCTS technique).

Emission to both bands may occur when the states are near the middle of the band gap. Defect states which are filled during the pulse period will return to their initial state if sufficient excitation energy, thermal or optical, is present to stimulate a bound-to-band

transition. The release of the carriers can be detected by the current they produce in an external circuit or by the change in the space charge which can be monitored by observing the depletion capacitance, as shown in Figure 3.7 and Figure 3.8. This latter method enables a distinction to be made between electron emission and hole emission.

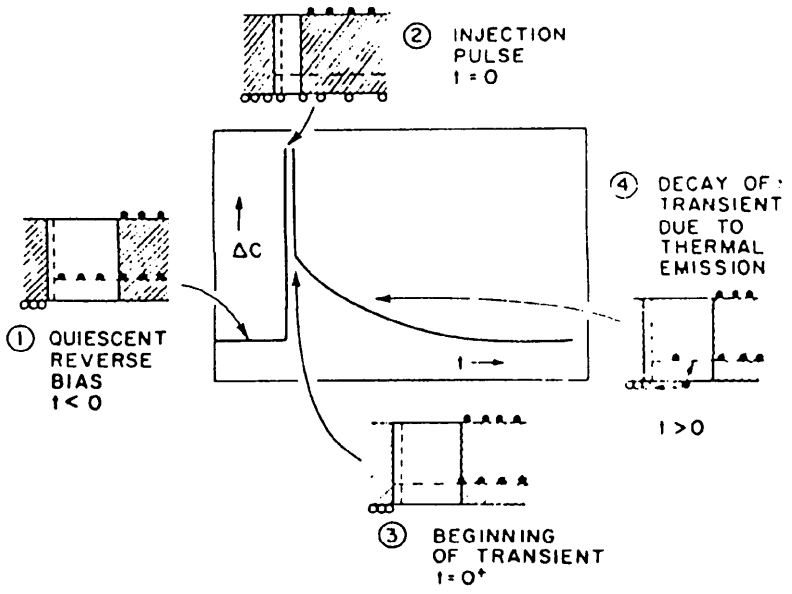

Figure 3.8 Capacitance transient due to a minority carrier trap emission in a p^+n diode

The temperature dependence of emission rate: The characteristic time constant of the transient shown in Figure 3.7 is e_n^{-1} given by equation (3.22). ΔE in equation (3.22) is referred to as the activation energy and is obtained from the slope of $\log(e_n/T^2)$ plotted against 1/T. The T^2 in $\log(e_n/T^2)$ takes into account the temperature dependence of $\langle v_n \rangle N_C$. The temperature dependence of the capture cross section and the real trap energy depth E_T (meaning its energetic displacement from the band) is unknown and usually neglected. We can obtain the temperature dependence of the capture cross section via the measurement of capture cross section at different temperatures directly. There are two capture mechanisms which are well documented as giving rise to

temperature dependence: *multiphonon capture* and *cascade capture*. For a neutral center only multiphonon emission is possible, but for a deep attractive or repulsive Coulomb center both mechanisms will be effective.

Electric field-enhanced emission: In addition to the temperature dependence effect mentioned above, the energy determination is also complicated by the electric field dependence of the thermal emission rate. The Poole-Frenkel effect has been suggested as been responsible for this phenomena. The electric field distorts the electrostatic potential binding the carrier to the center such that the barrier height for thermal emission is reduced. Alternatively it is suggested that the carrier may escape by tunnelling through the triangular barrier which is created by the combination of the potential of the center and the applied field [Vincent 79].

Influence from local environment: extended defects/impurity decoration: The value of e_n at a particular trap site may change in correspondence to the local environment in the crystal. It is demonstrated that electron emission behavior from states associated with extended defects can be modified by the degree of impurity decoration which may be associated with band bending resulting from the charge on the dislocation [Peaker 89b]. As another example increase in thermal activation energy and the pre-exponential factor was found in the deep state associated with the oxidation induced stacking faults in silicon when the stacking fault was spatially profiled [Kaniewski 92]. It was suggested that this deep state has an activation energy which depends on its position along the Frank partial dislocation bounding the stacking fault.

3.1.3.1.3 Carrier Capture at Majority and Minority Traps

3.1.3.1.3.1 Introduction

As illustrated in Figure 3.9, there are four possible combinations of two types of free carrier capture at two types of traps.

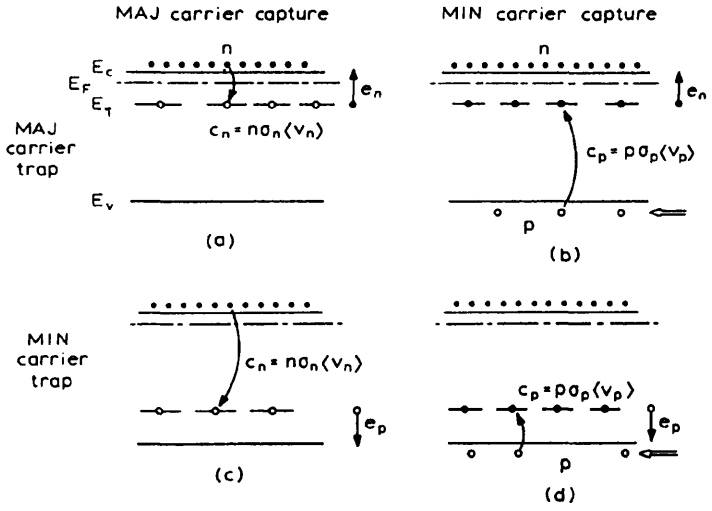

Figure 3.9 Band diagrams indicating the process of capture of majority and minority carriers at majority and minority carrier traps in an n-type semiconductor

The general principle of capture cross section measurements is to expose the traps (initially empty of carriers) to a known density of free carriers for a specified time, and then to use the depletion capacitance to monitor the change in net space charge density due to the capture of some of these carriers at the deep state. For the situation shown in Figure 3.9 (a) and (d), the trap is located in energy near to the band containing the carriers to be captured. Therefore the trap can be emptied prior to capture by thermal

emission. The occupancy requirement prior to each capture process illustrated in Figure 3.9 (b) and (c), however, calls for experiment arrangements that can first fill the traps with the opposite carriers. They are usually achieved using the double pulse techniques, that is, capture of minority carriers at a majority carrier trap (Figure 3.9 (b)) can be studied using a zero bias pulse followed by forward bias minority carrier pluses of various duration. The capture of majority carriers at a minority carrier trap (Figure 3.9 (c)) can be observed using a minority carrier forward bias injection pulse followed by zero bias majority carrier pulses of various lengths.

3.1.3.1.3.2 Majority Carrier Capture at a Majority Carrier Trap

Refer to Figure 3.9 (a). The most common method is to perform a DLTS emission transient experiment and stabilize the diode temperature at that of the DLTS peak of the trap of interest, then to measure the DLTS emission signal as a function of the trap filling time. For emission in a depletion region c_n=0 so the DLTS signal is proportional to the trapped electron concentration at the beginning of the emission transient which corresponds to the value of the trapped electron concentration at the end of the filling time. According to equation (3.29) the trapped electron concentration due to electron capture process into an initially empty electron trap is given by:

$$n_T(t_p)=N_T(1-e^{-c_n t_p}) \tag{3.32}$$

where c_n is the capture rate given by equation (3.15). Now consider the subsequent

emission process for the trapped electrons in the depletion layer. According to equation (3.28) and substitute N_T with the right-hand side of equation (3.32) we obtain:

$$n_T(t)=N_T(1-e^{-c_n t_f})e^{-e_n t}\approx N_T(1-e^{-c_n t_f}) \tag{3.33}$$

here t is the emission time which is usually taken as at least several times of e_n^{-1}. As will be discussed in detail in section 3.1.3.3 the DLTS signal heights ΔC obeys:

$$\frac{\Delta C}{C}\propto\frac{n_T(t)}{N_D} \tag{3.34}$$

here C represents the junction capacitance at the condition of DLTS measurement. For a very long (saturating) fill pulse we have:

$$\frac{\Delta C_{sat}}{C}\propto\frac{N_T}{N_D} \tag{3.35}$$

The constant of proportionality in the above two inequalities must be the same and therefore we have:

$$\frac{\Delta C}{\Delta C_{sat}}=\frac{n_T(t)}{N_T} \tag{3.36}$$

using equation (3.33) we obtain:

$$1-\frac{\Delta C}{\Delta C_{sat}}=1-(1-e^{-c_n t_f})e^{-e_n t}\approx e^{-c_n t_f} \tag{3.37}$$

Plotting the experiment data ($1-\Delta C/\Delta C_{sat}$) against filling time duration t_f the capture rate c_n can be derived.

3.1.3.1.3.3 Minority Carrier Capture at a Minority Carrier Trap

This situation is shown in Figure 3.9 (d), the thermal emission process for minority carriers can be used to study minority carrier capture in an analogous way to the study of majority carrier capture. Bipolar devices such as p^+n junctions can provide minority carriers through injection. Single carrier devices such as Schottky diodes can supply minority carriers through external excitation, for example optical pumping using above bandgap energy light. Initially the traps are full of electrons $n_T(0)=N_T$ and during the process of hole capture, the electron concentration on the trap is given by equation (3.26) as:

$$n_T(t_f)=n_T(\infty)-[n_T(\infty)-n_T(0)]e^{-(c_n+c_p+e_p)t_f} \tag{3.38}$$

where:

$$n_T(\infty)=\frac{c_n+e_p}{c_n+e_p+c_p}N_T \tag{3.39}$$

Let $p_T(t_f)=N_T - n_T(t_f)$ be the concentration of trapped holes equation (3.38) becomes:

$$p_T(t_f)=p_T(\infty)[1-e^{-(c_n+c_p+e_p)t_f}] \tag{3.40}$$

This equation has the same form as equation (3.32) of majority carrier capture at a majority carrier trap. Following the same principle as for the majority case, but bearing in mind that here we observe the minority carrier emission which is reflected in the sign of the capacitance transient, we can derive the capture time constant. This capture time constant may or may not include the majority carrier capture depending on which method we choose to supply the minority carriers.

Junction Injection: In this case holes are introduced by forward biasing a p^+n junction. Both electrons and holes are captured using this method. We have:

$$c_p=\sigma_p\langle v_p\rangle p_n(V_f) \tag{3.41}$$

for hole capture, where p_n is the hole concentration in n-type material and V_f, the forward bias. For majority carrier capture it is $c_n=\sigma_n\langle v_n\rangle N_D$, assuming low injection condition. The trap occupancy is changed from its equilibrium value during the injection provided that $c_p>c_n$. The capture time constant $(c_n+c_p+e_p)^{-1}$ can be derived, c_n can be measured using a majority carrier pulse and e_p is known from the rate-window. σ_p can then be calculated using the injected carrier density $p_n(V_f)$ estimated from the forward current density [Henry 73]. Previously we described obtaining the capture cross section by plotting the DLTS related signal against filling time, in practice it is more convenient to vary the injected carrier density and plot the DLTS related signal against injection current.

MCTS: Illumination with photons of energy greater than the band gap generate electron-hole pairs within the semiconductor. When we illuminate the semiconductor from the **front** through a semitransparent Schottky barrier, in the depletion region, the hole current is made up of drift and diffusion components whereas the electron current is only made up of drift current. If we can arrange that $p\sigma_p > n\sigma_n$, in reality we often make the minority carrier current exceed the majority carrier current so that the steady state hole concentration exceeds the electron concentration then the traps are more likely filled by minority carrier capture from this hole current. In the real experiment we must make sure that the diffusion length is greater than the absorption distance, and that the absorption distance should be greater than the depletion depth [Blood 92] so that holes are generated beyond the depletion depth and most of these are collected by the barrier. In this case the capture time constant in equation (3.40) reduces to include only c_p and e_p. And the hole concentration can be obtained from the photocurrent [Blood 92] assuming the hole diffusion current exceeds the drift current and ignoring the electron current. In materials with a long minority carrier diffusion length we can illuminate through the **back** of the sample. Carriers generated outside the depletion region (it is important for ensuring there is no electron drift current) diffuse down their concentration gradient towards the depletion region there they are immediately drawn into the depletion region by the depletion field whereas the same field excludes electrons. Again the hole concentraion in the depletion is assumed constant and can be calculated from the measured photocurrent as for the front illumination case. This rear illumination emthod requires the thickness of undepleted material to be greater than the optical absorption distande but not significantly greater than the minority carrier diffusion length. Figure 3.10 shows the band diagram of (a) front and (b) back illumination cases respectively.

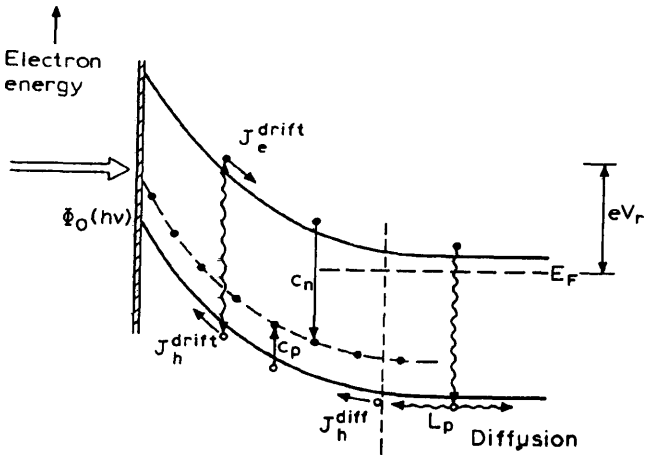

(a)

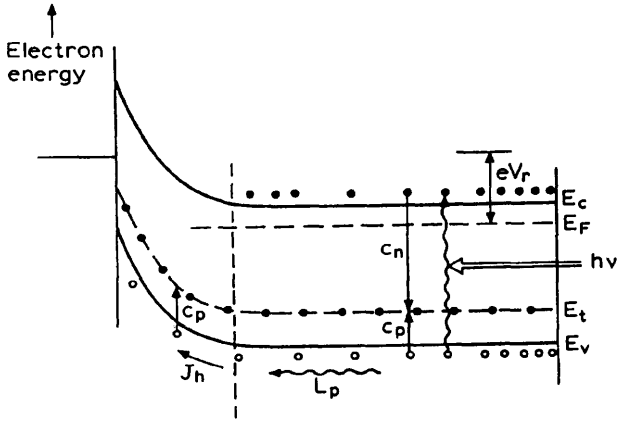

(b)

Figure 3.10 Band diagram of a reverse biased n-type semiconductor containing a minority carrier trap. Minority carriers are injected by:
(a) Front illumination through a semi-transparent Schottky barrier
(b) illumination through the back of a Schottky barrier

3.1.3.1.3.4 Minority Carrier Capture at a Majority Carrier Trap

Refer to Figure 3.9 (b). Both majority and minority carrier injections are required in measuring the capture cross section. As illustrated in Figure 3.11 (a), still using p^+n as an example, with the first pulse A of duration greater than c_n^{-1} all the traps are occupied with majority carriers (electrons). Then within a time much shorter than e_n^{-1} minority carriers (holes), are introduced by the second pulse B provided that $c_n < c_p$, or alternatively by rear illumination as described previously. When the diode is returned to its reverse bias the traps which are not occupied with holes empty electrons by thermal emission. The amplitude of this thermal emission transient provides a measure of the number of traps not filled with minority carriers at the end of the injection pulse B. The process of hole capture transient and electron emission transient is illustrated in Figure 3.11 (b).

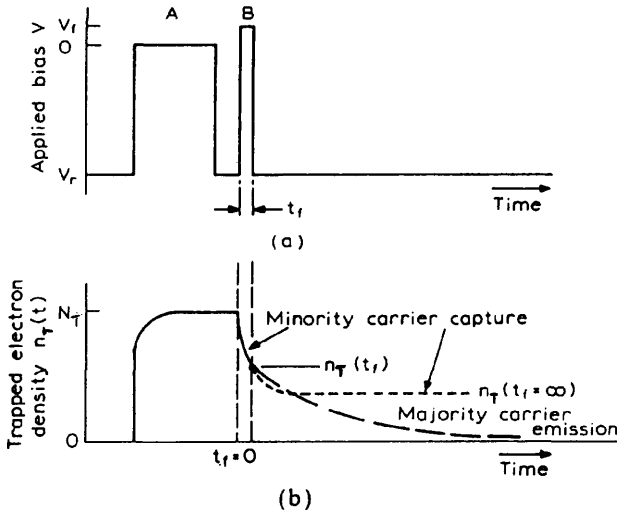

Figure 3.11 Hole capture at an electron trap in n-type semiconductor
(a)the voltage pulse sequence (double pulse technique)
(b)the processes involved in the observation of hole capture transient and electron emission transient

At the start of the minority carrier filling pulse B (at the end of pulse A) all the traps are filled with electrons and so $n_T(0)=N_T$. And at a saturated injection pulse B $n_T(\infty)=N_T c_n/(c_n+c_p)$. Use these two conditions and equation (3.26) we can express the concentration of the traps not filled with holes which is related to the amplitude of the subsequent DLTS majority carrier emission signal, assuming all the electrons are emptied at the end of emission period, as:

$$n_T(t_f)=N_T[\frac{c_n}{c_p}-\frac{c_p-c_n}{c_p}e^{-(c_n+c_p)t_f}]\approx N_T e^{-(c_n+c_p)t_f} \qquad (3.42)$$

Whereas N_T is proportional to the DLTS signal in the absence of pulse B.

3.1.3.1.3.5 Majority Carrier Capture at a Minority Carrier Trap

This situation is shown in Figure 3.9 (c). In order to observe the majority carrier capture at the minority carrier trap, injection pulse of minority carriers should be applied prior to the majority pulse. Figure 3.12 illustrates the pulse sequence (a) and the time dependence of the trapped electron density (b). At the end of pulse A (beginning of pulse B): $n_T(0)=N_T c_n/(c_n+c_p)$ $(c_n<c_p)$, at the end of pulse B $n_T(\infty)=N_T$, according to equation (3.26) that after a pulse of majority carrier of duration t_f we obtain:

$$n_T(t_f)=N_T(1-\frac{c_p}{c_n+c_p}e^{-c_n t_f}) \qquad (3.43)$$

The amplitude of the subsequent DLTS minority carrier emission signal following pulse B is proportional to $p_T(t_f)$ which could be expressed as:

$$p_T(t_f)=N_T-n_T(t_f)\approx N_T\frac{c_p}{c_n+c_p}e^{-c_n t_f}\approx p_T(0)e^{-c_n t_f} \tag{3.44}$$

where $p_T(0)$ is the signal measured in the absence of pulse B.

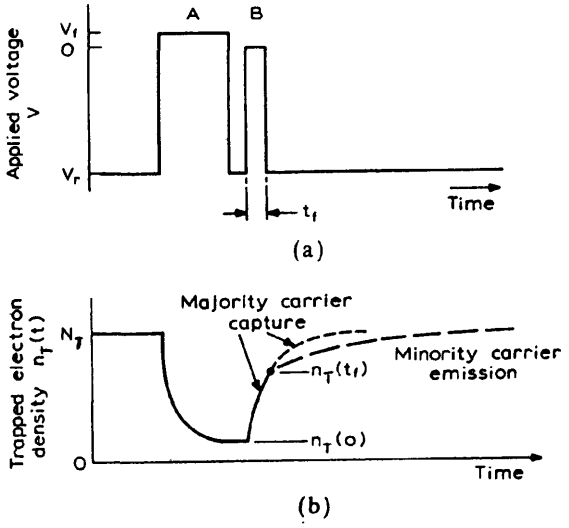

Figure 3.12 Electron capture at a hole trap in n-type semiconductor
(a) the applied voltage pulse sequence
(b) the time dependence of the trapped electron density

3.1.3.1.3.6 Precautions

Slow carrier capture in the transition region: The capture measurements described so far assumed that the capture process is the same for all the traps within the reverse biased

depletion region. This is not strictly so because during the capture period the free carrier density decreases at the edge of the collapsed depletion edge, reducing the capture rate. In this case the capture transient is actually made up of a fast component representing the uniform region and a slow component determined by the free carrier tail. In real experiments this process of slow carrier capture in the transition region can obscure the simple exponential capture process of the "bulk" material.

Large trap concentration: We also assumed that the carriers are captured from a source of free carriers of constant density. However when the trap concentration is large free carriers available for capture may decrease with time. The capture transient then becomes non-exponential.

3.1.3.1.4 Deep State Depth Profiles

There are a number of experimental schemes which can be used to derive deep level concentration profiles [Hawkins 89]. One method which we use in this work is varying both the filling and reverse bias but keeping a fixed small difference between them. Refer to Figure 3.13, W_1 and W_2 are the depletion region widths at filling and reverse bias respectively, y_1 and y_2 are the crossing points where the deep state E_T meets the Fermi level E_F at filling and reverse bias respectively. The average trap concentration between y_1 and y_2 will be derived as follows. For a reverse-bias voltage increment ΔV, a charge density of $qN_T(x)\Delta x$ is uncovered, according to Gauss's law:

$$\Delta E=\frac{\Delta V}{x}=(\frac{q}{\epsilon})N_T(x)\Delta x \qquad (3.45)$$

the voltage drop across the region between y_1 and y_2 is given by:

$$\Delta V=\frac{q}{\epsilon}\int_{y_1}^{y_2} xN_T(x)dx \tag{3.46}$$

Assume uniform concentration over the region between y_1 and y_2 we have:

$$\Delta V=\frac{qN_T(y)}{\epsilon}\frac{y_2^2-y_1^2}{2} \tag{3.47}$$

and we know [Kimerling 74]:

$$y_1=W_1-[\frac{2\epsilon(E_F-E_T)}{qN_D}]^{1/2} \tag{3.48}$$

where N_D is the shallow donor concentration. A similar equation can be derived for y_2. We now return to the fundamental equation:

$$\Delta C=\Delta V(\frac{dC}{dV}) \tag{3.49}$$

From equations (3.47) and (3.49) we obtain:

$$N_T(y)=\frac{2\epsilon}{q}\frac{\Delta C}{y_2^2-y_1^2}(\frac{dC}{dV})^{-1} \tag{3.50}$$

ΔC can be measured from the DLTS peak height and dC/dV from the high frequency capacitance voltage measurement. This technique is restricted to low trap concentrations so that we have an exponential transient appropriate for DLTS analysis.

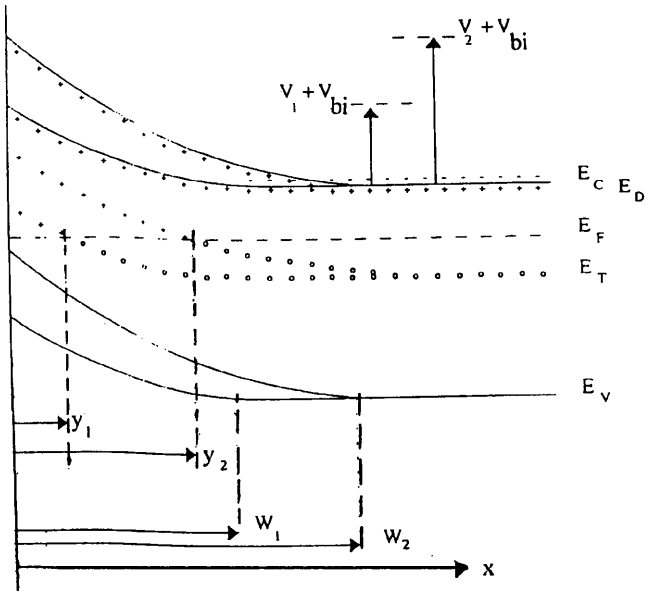

Figure 3.13 Band diagram of a p^+n (or a Schottky barrier) at bias V_1 (filling voltage) and V_2 (reverse voltage)

3.1.3.2 Deep Level Transient Spectroscopy (DLTS)

3.1.3.2.1 Principle

Deep Level Transient Spectroscopy (DLTS) [Lang 74] is used to obtain information about a deep level state in the depletion region of a Schottky barrier or a p^+n junction by observing the capacitance transient associated with the carrier emission in order to return to thermal equilibrium of the occupation of the deep state following an initial nonequilibrium condition. For convenience we draw the pulse sequence and the

emission transient again here. Refer to Figure 3.14.

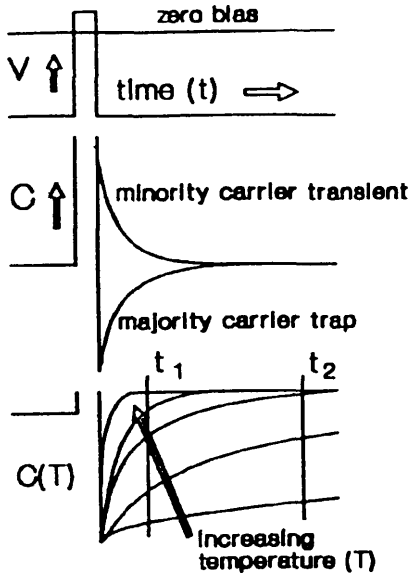

Figure 3.14 Capacitance transients resulting from applying a voltage pulse to a diode containing deep states. *After Peaker [Peaker 89a]*
(a) bias sequence on the diode
(b) capacitance transients from deep state levels
(c) capacitance transient as a function of temperature

The initial nonequilibrium condition is set by applying a zero or forward bias pulse (Figure 3.14 (a)) to the device to fill the traps with carriers and then observe the capacitance transient (Figure 3.14 (b)) after the device is switched into reverse bias again. One measures the time constant of this transient as a function of temperature (Figure 3.14(c)). The time constant changes rapidly with temperature because of the Boltzmann's factor in equation (3.22). t_1 and t_2 in Figure 3.14 (c) are two sampling pulses after the end of the fill bias pulse. At low temperature the exponential transient

is very slow and at high temperatures it is very quick. At one intermediate temperature the transient between t_1 and t_2 reaches a maximum output. This happens when the defect emission rate e_n equals the reciprocal of the preset time constant of the system τ_{ref} , it is illustrated in Figure 3.15.

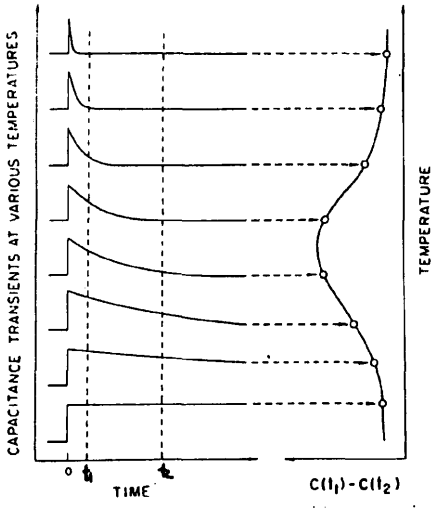

Figure 3.15 Implementation of a rate window by means of a double-boxcar integrator. The left-hand side shows capacitance transients at various temperatures, while the right-hand side shows the corresponding DLTS signal. *After Lang [Lang 74]*

Now define the normalized DLTS signal S(T) as:

$$S(T)=[C(t_1)-C(t_2)]/\Delta C(0) \tag{3.51}$$

where $\Delta C(0)$ is the capacitance change due to the saturated filling of the deep state. Assume exponential transients (practically it is fulfilled using $N_T \leq 0.1N_D$) we have:

$$S(T)=\exp^{-t_1/\tau_{ref}}-\exp^{-t_2/\tau_{ref}} \tag{3.52}$$

by differentiating S(T) with respect to τ_{ref} and setting the result to zero, we obtain the system time constant, τ_{max} , corresponding to the maximum output of the transient.

$$\tau_{max}=(t_1-t_2)/\ln(t_1/t_2) \tag{3.53}$$

The reciprocal of this present time constant is often referred to as the **rate window.** If we want to produce an Arrhenius plot for the activation energy of the trap we need to choose different rate windows to scan the sample. If there exist more than one trap within the material we will observe more than one DLTS peaks at different temperatures at which the emission rate of this particular trap matches the rate window. When we apply a fill pulse with forward bias to inject minority carriers, provided $c_{min} \geq c_{maj}$ we may observe a transient of the opposite sign of the majority trap which is associated with minority carriers captured at the deep defect.

3.1.3.2.2 Experiment Set Up

Figure 3.16 is the block diagram of the DLTS system used at UMIST in this work. The sample is situated in a variable temperature cryostat with the temperature monitored by a platinum resistor sensor. The temperature scan rate can be selected from 0.2 to 0.01 K s^{-1}. The cooling is provided by liquid nitrogen flow (a liquid helium system will be used when temperatures are required lower than 77 K). This is controlled by the

temperature controller. A modified BOONTON 72B capacitance meter is used either alone or in the differential mode connected with a fixed back-off capacitor to improve the measurement sensitivity. The POLARON DL4600 system generates a repetitive pulse sequence which provides the filling bias, reverse bias and three sampling pulses for establishing two rate windows at one scan. A pulse generator is applied directly to the sample via a fast pulse interface when a very short filling pulse is required to measure the capture cross section.

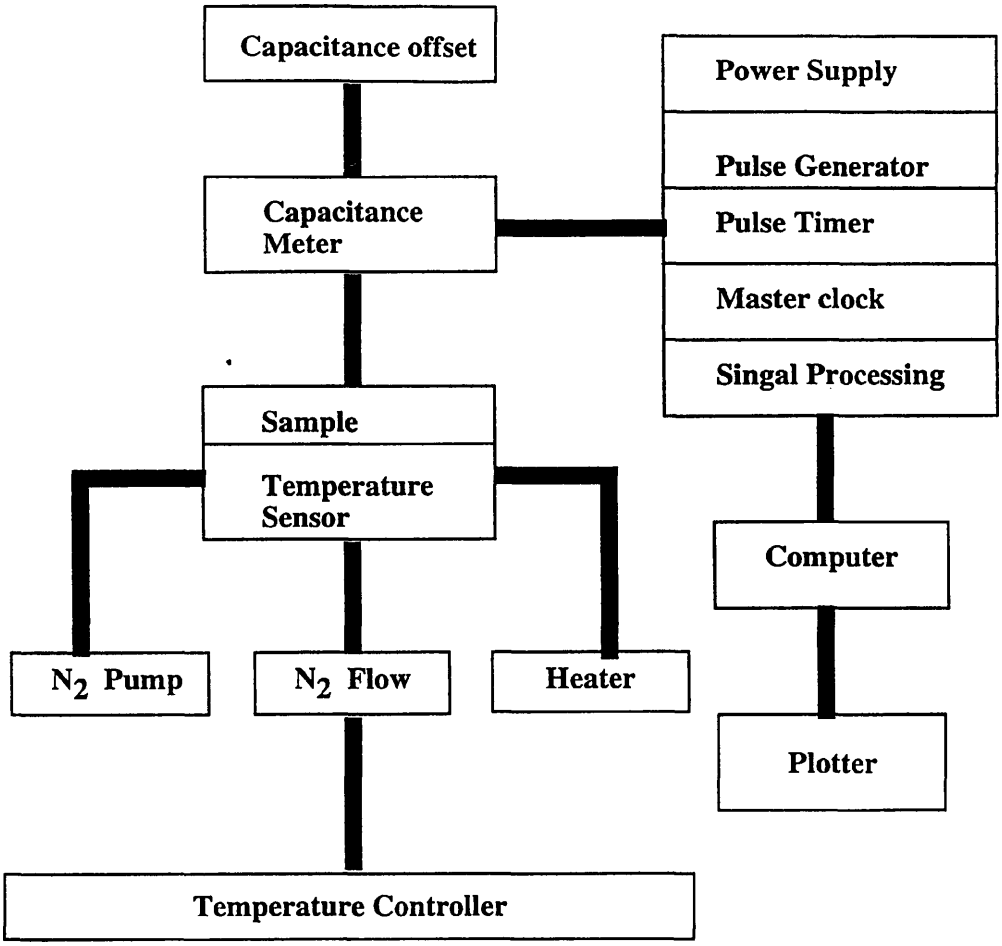

Figure 3.16 Block diagram of DLTS system

3.1.3.2.3 Practical Considerations

The current-voltage characteristics of a diode is expressed as $I = I_o (e^{qV/nkT} - 1)$, here I is the junction current, I_o the reverse saturation current and n is a semiempririal parameter that usually lies in the range $1 \leq n \leq 2$ for most junctions. Under forward bias condition this current can introduce minority carriers for trap to capture. This is considered as an advantage. Under reverse bias condition the leakage current can cause competition between carrier capture and thermal emission resulting in a decrease in the DLTS peak amplitude which becomes more obvious at lower rate windows. Another problem is caused by series resistance of the diode which mainly consists of contact resistance and the resistance of the undepleted material. An increase in series resistance causes a decrease in the measured capacitance and phase shifts and can lead to potential measurement errors such as a majority trap can produce a minority trap emission peak. In reality before we carry out DLTS measurements we first measure the I-V curve of the diode to check the leakage current and then have the phase angle checked through the C-V measurement to monitor the series resistance.

3.2 Photoluminescence (PL)

3.2.1 Basic Theory

Photoluminescence is a non-destructive optical technique which relies upon returning the semiconductor to its equilibrium condition after exciting it to a non-equilibrium

state. The emission results from this. Applications include measurement of the concentrations of shallow impurities in silicon, identification of some point defects and detection of dislocations, indicating material quality. Additionally observation of quantum confinement effects in low dimensional structures can be carried out. In photoluminescence we use a laser as the energy source that pumps electrons into higher states. When the photon energy equals or exceeds the bandgap they can excite valence electrons across the bandgap. The excited electrons will recombine with holes upon returing to equilibrium. If this process is radiative, it emits a photon whose energy gives the difference between the excited electron-hole state and the state after recombination. The emission spectrum shows a fingerprint peak related to this energy emission.

Band to band recombination is the fundamental radiative recombination the probability of which is strongly affected by whether the bandgap is direct or indirect since both absorption and emission probabilities depend upon the bandstructure. Because a photon carries negligible momentum compared to that of the electron, a vertical transition from conduction band minimum to valence band maximum occurs with a high probability in direct bandgap materials to conserve the momentum. Energy is conserved according to:

$$h\upsilon = E_f - E_i \tag{3.54}$$

Where E_f and E_i are the final and initial state energies respectively, and $h\upsilon$ is the photon energy. For indirect bandgap materials such as silicon, because the valence band maximum occurs at $k = 0$ and the conduction band minimum locates at $k_m = 0.8$ of the zone boundary along 001 axes from $k = 0$, the band to band transition needs the

participation of a phonon of wavector - k_m to be absorbed or k_m to be created. The energy conservation leads to the general formula:

$$h\upsilon = E_f - E_i \pm \hbar\Omega \tag{3.55}$$

where $\hbar\Omega$ is the energy of the phonon. The plus and minus signs correspond to phonon absorption and emission, respectively. Phonon emission dominates at low temperatures. Current values of the energy of the k_m phonon in silicon are [Vouk 77]:

18.4 $\pm$ 0.2 meV, TA mode,

56.2 $\pm$ 1 meV, LO mode,

58.0$\pm$ 1 meV, TO mode.

These were obtained initially by comparing the absorption and emission of phonons at high temperature [Macfarlane 59]. The relative ratios of the phonon-assisted peaks are temperature dependent in silicon. At temperatures T $\geq$ 15 K the relative intensities are [Vouk 77]: TA:LO:TO = 0.03:0.1:1, and measurements made in this thesis are at or above this temperature. The need for an additional third body interaction with the phonon makes indirect material band to band transition far less probable than direct material.

Free exciton (FE) transitions are very likely at low temperatures (below 4K) in high quality pure semiconductors. Coulombic attraction between the photon generated electron and hole can bind them into the quasi-hydrogenic exciton and the energy levels of the e-h combination can be expressed as:

$$E_{ex} = -[\frac{m_r^*}{m}][\frac{\epsilon_o}{\epsilon}]\frac{1}{n^2}13.6eV \tag{3.56}$$

where E_{ex} is the binding energy of the exciton and m_r^* is the reduced effective mass. n are positive integers. The binding energy in its ground 1s state for silicon is calculated to be 14.3 $\pm$ 0.5 meV [Shaklee 70]. The exciton can move as a whole through the crystal, but with a net charge of zero carrying no current. An exciton supports a set of bound energy levels like those in a hydrogen atom. In a direct gap semiconductor, with the bandgap energy E_g, the energy of the photon emitted when the exciton collapses radiatively is:

$$h\upsilon = E_g - E_{ex} \tag{3.57}$$

For an indirect semiconductor, the emitted photon energy is:

$$h\upsilon = E_g - E_{ex} \pm \hbar\Omega \tag{3.58}$$

The reason that the phonon is the same as in the band to band transition case is that the electron and hole momentum states are essentially the same. Free exciton transitions can be identified in two ways when a laser power dependence study is carried out. Firstly, they tend to have weak and broad lineshape features of the order of kT. Secondly, the signal intensity has a super linear dependence upon laser power, as it depends upon both the hole and electron concentrations. The exact dependence is affected by non-radiative competition, which varies from sample to sample, and between material systems. This

is in contrast to the signal due to recombination from an impurity bound e-h pair which saturates at high laser power because there is a finite number of impurities.

Bound exciton (BE) recombination: Because the free exciton consists of electron and hole states widely separated in ***k*** space, their probability of recombination is low. In the case when the sample is not very pure, during the lifetime of the free exciton there is therefore a significant probability of the exciton being trapped at a donor, an acceptor, neutral impurities or crystal defects to form bound excitons due to the Coulomb forces. Bound exciton recombination occurs in the similar way as the free exciton recombination but the emitted photon energy is lower since the binding to the impurity/defect is stronger. The energy difference is determined by the particular impurity which binds the exciton.

Free to bound (FB) and ***bound to bound*** transitions: Radiative transitions can also take place between donor/acceptor states and the valence and conduction bands. These includes: donor-bound electron to valence band, conduction band to acceptor-bound hole, they are called free to bound transitions. Donor-bound electron to acceptor-bound hole transitions can also occur, if they are physically close to each other (DAP). The DAP transition energy is given by:

$$h\upsilon = E_g - (E_A + E_D) + \frac{e^2}{\epsilon R} + J(R) \tag{3.59}$$

where the E_A and E_D are the acceptor and donor ionization (binding) energies, respectively. R is the spatial separation of the donor and acceptor pair involved in the

recombination, and J(R) is a correction term which describes the deviation of the luminescence energy from a simple Coulomb law because of the interaction of the donor and acceptor wave functions [Efeoğlu 93].

There exist many other transitions like transitions at impurities trapped in dislocation strain fields (e.g.D-lines in silicon), excitons bound to isoelectronic impurities and internal transitions within excited impurities (e.g.rare earths transition metals).

One key area of interest is the evaluation of impurity concentrations from PL spectra. It is not possible to draw a correlation between the intensity of a given line and the concentration of that impurity owing to the different non-radiative effects. A novel approach to this problem has been presented by Tajima [Tajima 77] using the ratio technique. By taking the ratio of the free exciton and the bound exciton peaks in silicon it is possible to obtain a reasonable estimate of the impurity concentrations. This technique will only work well at low impurity concentrations, where the intrinsic peak is not obscured by the impurity peak.

Figure 3.17 is a PL spectrum of a high purity float zone silicon. The TA, LO and TO phonon replicas of the free exciton luminescence and bound exciton peaks (both no phonon and phonon replicas) associated with very low concentrations of aluminum, phosphorus and boron can be seen [Colley 87].

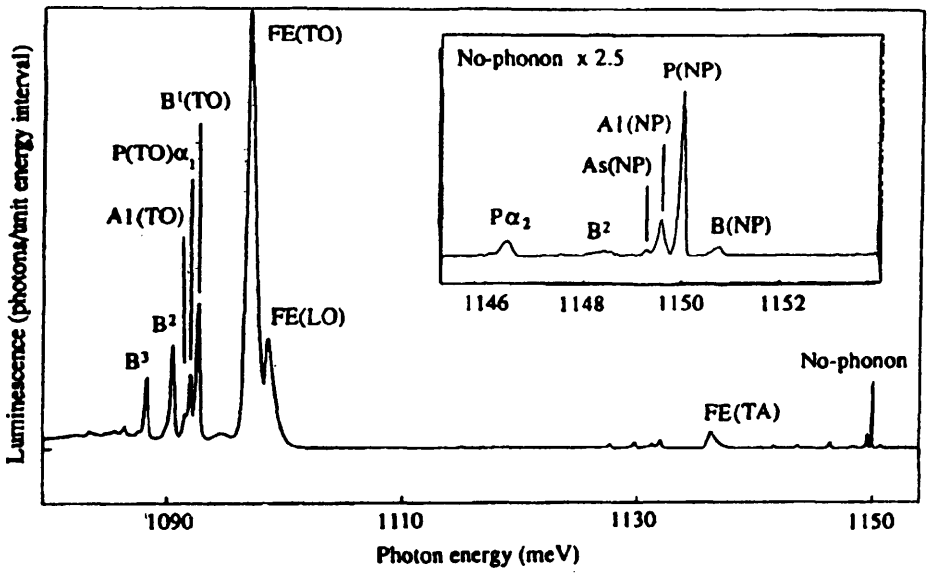

Figure 3.17 PL spectra of a high purity float zone silicon. The TA, LO and TO phonon replicas of the free exciton luminescence can be seen and so are bound exciton peaks associated with very low concentrations of different impurities. *After Colley [Colley 87].*

3.2.2 Experiment Set Up

Figure 3.18 is a block diagram of the photoluminescence system used in this work. The cryostat is a CTI Cryogenics refrigeration cryostat with a minimum coldhead temperature of 10K. The optical excitation is performed by an argon ion laser of wave length 514nm (extinction length is 1μm in silicon). The beam is mechanically chopped at a suitable frequency for good detector response (typically 300 Hz for a cooled germanium detector). A liquid nitrogen cooled North Coast germanium detector is used for signal detection. The signal from the detector is processed by a SR5 10 model lock-in amplifier. The emitted light is collected from the front face of the sample and is

focused onto the entrance slit of a grating spectrometer. A suitable long-pass filter allows only the PL to pass and blocks the scattered laser light. The software controls the temperature via a Lakeshore DRC 91C model temperature controller and also sets the spectrometer to the required wavelength position and records the signal from the lock-in amplifier.

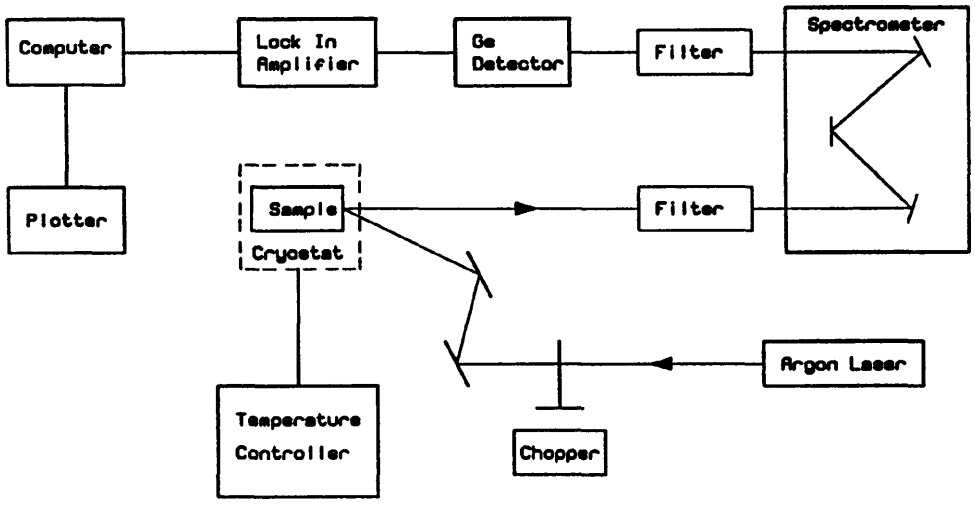

Figure 3.18 Block diagram of the photoluminescence system used in this work

3.3 Double Crystal X-ray Diffraction

3.3.1 Principle of the Technique

X-ray diffraction is a non-destructive technique which can be used to directly measure the lattice mismatch between epitaxial layers and the substrate. Information such as crystal quality, layer thickness and wafer curvature can also be obtained from the X-ray rocking curves. In this work (chapter 5) this technique is used to study the composition and strain depth profiles of Si_xGe_{1-x} alloy structures. When used in conjunction with other techniques, such as TEM, alloy relaxation mechanism can be investigated and optimum growth condition may be found.

Consider a single crystal with interatomic spacing a. When a beam of X-rays incidents on the atomic planes at an angle θ, it is reflected from each successive plane. These reflected rays will be completely in phase if the path difference is a whole number, n, of the X-ray wavelength, λ. A peak in the diffraction pattern will result corresponding to the condition:

$$n\lambda = 2aSin\theta \tag{3.60}$$

This is known as the 'Braggs Law'. Now consider an epilayer with lattice constant a_{epi} grown on a substrate with a slightly different lattice constant a_{subs}. The Bragg angles of the epilayer (θ_{epi}) and the substrate (θ_{subs})can be expressed respectively as:

$$n\lambda = 2a_{epi} Sin\theta_{epi} \tag{3.61}$$

$$n\lambda = 2a_{subs} Sin\theta_{subs} \tag{3.62}$$

Assuming the angular difference is much smaller than either of the substrate or the epilayer, the measured (effective) lattice mismatch $m^* = (a_{epi} - a_{subs})/a_{subs}$ can be expressed as:

$$m^* = (\theta_{subs} - \theta_{epi})\cot\theta_B = \Delta\theta\cot\theta_B \tag{3.63}$$

here angles are expressed in radians and θ_B is the Bragg angle which is equal to θ_{subs}. Thus the difference in the two lattice constants can be deduced from the angular separation $\Delta\theta$ measured from the spacing of the two peaks in the rocking curve. Note that in this reflection geometry it provides data only on the lattice parameter mismatch normal to the specimen surface. The measured mismatch m^* is not the real mismatch m, to which composition is directly related. This is because for a coherent interface the epilayer will be in either compression or tension strain and as a result of the Poisson ratio effect, the layer becomes tetragonally distorted. The lattice parameter normal to the surface is changed via the Poisson ratio effect:

$$m^* = m\frac{1+\nu}{1-\nu} \tag{3.64}$$

where υ is Poisson's ratio. From Vegard's law which states that the lattice parameter

varies linearly with the alloy composition we can obtain the chemical composition of the alloy.

When we have an epilayer with a varying lattice parameter with depth, we need to simulate the structure and compare it with the experiment result until the best fit is found. Most simulation programs are based on the solution of the Takagi-Taupin equations [Takagi 62]. As an example, Figure 3.19 shows the experimental (**a**) and simulated (**b**) rocking curves of a $Si_{1-x}Ge_x$ alloy structure (for detailed information about this structure see chapter 5 of this thesis) studied in this work. The strain depth profile obtained from the fit of the simulation to the experiment result is in agreement with the Ge compostion distribution (Gaussian distribution resulted from Ge^+ implantation). This result indicates a fully strained structure which is confirmed by the TEM results.

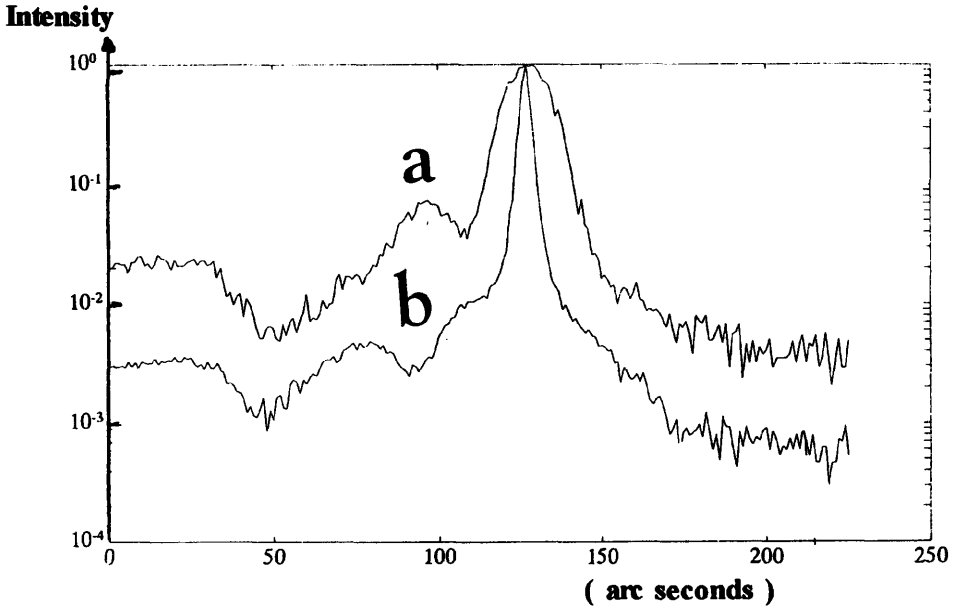

Figure 3.19 Experimental (a) and simulated (b) X-ray rocking curve of a Si_{1-x} Ge_x alloy resulted from Ge ion implantation

3.3.2 Experiment Set Up

Figure 3.20 is a schematic diagram of the double crystal diffraction technique. X-rays from the source are diffracted first from a reference crystal and then the specimen (hence the name double crystal diffraction) before being detected in a fixed, large aperture detector usually an scintillator in front of a photomultiplier. The electrical pulses, each of which corresponds to the absorption of a single X-ray photon, are amplified and, after pulse height analysis to discriminate against background, are counted to give a direct measure of X-ray intensity. To record a rocking curve the specimen is rotated about an axis normal to the plane of diffraction and the intensity recorded as a function of angle.

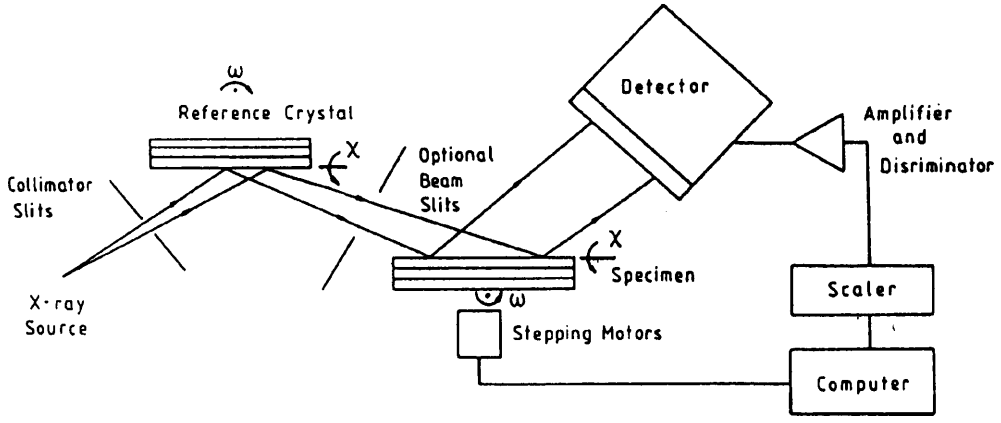

Figure. 3.20 Schematic diagram of the double crystal diffraction system

3.4 Optical Absorption Measurements Using Fourier Transform Infrared Spectroscopy (FTIR)

3.4.1 Introduction

Fourier transform infrared (FTIR) spectroscopy is a rapid and non-destructive technique used widely throughout the semiconductor industry. One of the most important applications of the FTIR technique is to quantitatively determine impurity concentrations in silicon and other semiconductor materials. There are two different absorption mechanisms of interest for IR measurements:

(a) the local vibrational modes caused by the distortion of the semiconductor crystal lattice due to impurity atoms on lattice or on interstitial sites which are bound to the neighboring host lattice atoms exhibiting a dipole momentum

(b) the electronic bands caused by the excitation of excited states of electrically active impurities exhibiting mostly shallow levels in the forbidden band gap of the semiconductor

Complications may arise from lattice vibrations of the host semiconductor, free carrier absorption and surface layer absorptions, for example oxides or rough surface. Free carrier absorption depends on the density of free carriers. For carrier density less than 1×10^{16} cm^{-3} it is not significant. Sample surface condition can be improved by proper surface treatment. In practice the easiest way to avoid the superposition of various absorption mechanisms is to record a reference spectrum at the same time when measuring the test sample. For an ideal reference spectrum the test sample and the reference sample must agree in all properties, but one which is under investigation.

For materials of high absorption coefficient or of thick slices the transmittance T for normal incidence is given by:

$$T=(1-R)^2 e^{-\alpha d} \tag{3.65}$$

where R is the reflectivity at a particular wavelength, α is the absorption coefficient and d is the sample thickness. In order to obtain the absorption coefficient from a reference spectrum the transmittance T_s of the sample is divided by the transmittance T_r of the reference sample:

$$\frac{T_s}{T_r}=e^{-(\alpha_s-\alpha_r)d} \tag{3.66}$$

3.4.2 Interstitial Oxygen and Substitutional Carbon in Silicon

3.4.2.1 Lattice Absorption spectrum of Silicon

High purity, single crystal silicon material could be produced by float zone (FZ) processing of the CZ grown single crystal silicon. Figure 3.21 shows the FTIR absorption spectrum of a FZ sample 2 mm thick. The strongest band seen in the spectrum at 610 cm^{-1} is assigned as the combination of a TO (transverse optical phonon) and TA (transverse acoustical phonon) and is commonly referred to as the "two-phonon" band.

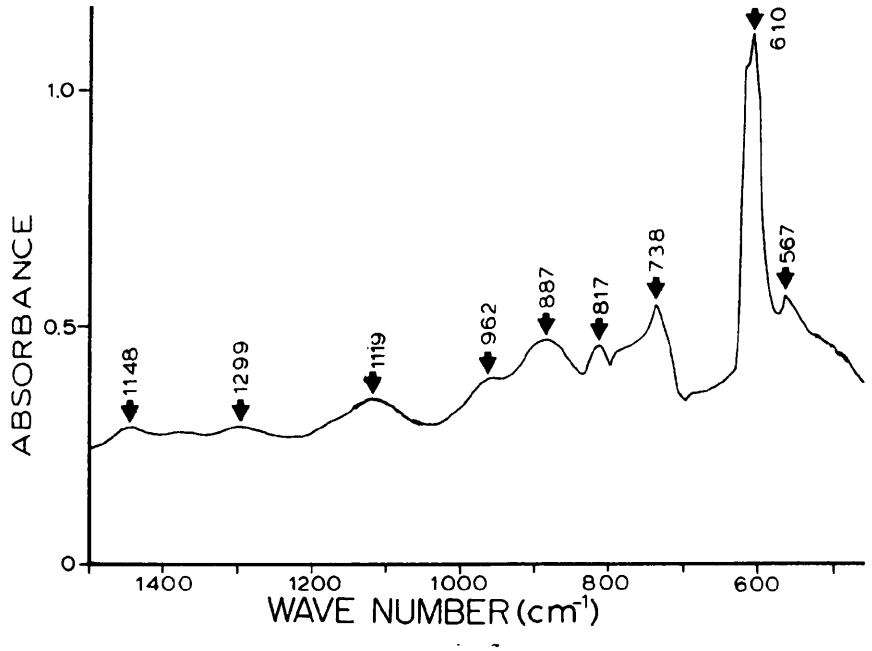

Figure 3.21 Infrared absorption spectrum of a float zone silicon sample showing the silicon phonon bands

3.4.2.2 Oxygen in Silicon

The oxygen atoms can occupy interstitial sites in the silicon unit cell and form two strong Si-O bonds with the nearest-neighbor silicon atoms. This is illustrated in Figure 3.22. During the semiconductor device fabrication the silicon is subjected to a number of different thermal budgets which can result in converting some of the interstitial oxygen into oxygen precipitates. There are three major modes of vibration in the Si-O-Si quasi-molecule (interstitial oxygen) which is shown in Figure 3.23 [Bosomworth 70].

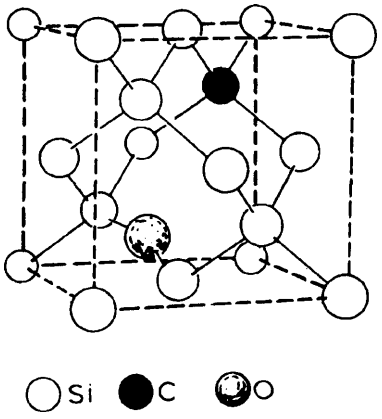

Figure 3.22 Unit cell of silicon containing interstitial oxygen and substitutional carbon

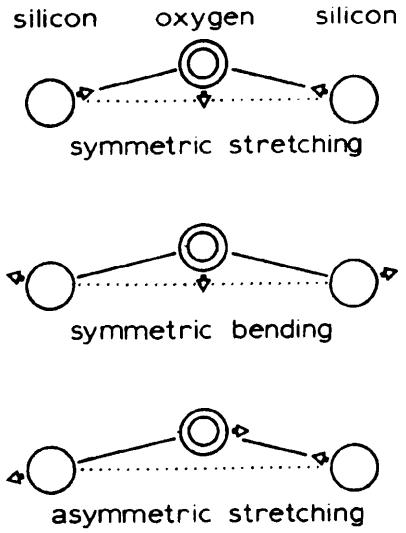

Figure 3.23 Normal vibrational modes of Si-O-Si quasi-linear molecule

Clear assignment has been given to the asymmetric stretching mode, 1107 cm^{-1} band at room temperature which is used for the quantitative determination of the oxygen content in silicon and symmetric bending mode, 515 cm^{-1}, though there has been some controversy in the literature regarding the nature of this absorption. The absorption bands of oxygen precipitates are suggested to be different due to the different precipitation stages at different temperatures [Gaworzewski 84]. Organizations have established standard procedures for the measurement of the interstitial oxygen concentrations in silicon based on the absorption coefficient of the 1107 cm^{-1} band. The method includes conversion factors that will convert the measured absorption coefficient into the oxygen concentrations expressed as parts per million atoms per cubic centimeter according to:

Oxygen concentration = absorption coefficient x conversion factor

Several values for the conversion factor ranging from 2.45 to 4.82 x 10^{17} cm^{-2} have been reported by different measuring organizations such as ASTM (American Society for

Testing Materials), DIN (Deutsches Institute für Normung) in the Federal Republic of Germany and JEIDA (Japan Electronics Industry Development Association) in Japan and so on. The discrepancy of the value of the conversion factor is due to the difficulty in conducting the experiments from which the value is extracted by these organizations. The "Old ASTM (1979)" standard specified a value of 4.82×10^{17} cm^{-2}. In 1980, ASTM approved a new value of 2.45×10^{17} cm^{-2} which is referred to as the "New ASTM" standard. The JEIDA determined a value of 3.03×10^{17} cm^{-2}. The measurements given throughout this thesis have been calculated using the New ASTM standard.

3.4.2.3 Substitutional Carbon in Silicon

The carbon impurity occupies substitutional sites in the silicon lattice, as shown in Figure 3.22, and forms C-Si bonds. The stretching of this bond in the silicon lattice gives rise to an infrared absorption band at 607 cm^{-1} [Newman 65]. Since this band is completely overlapped by the strong two phonon band of silicon, the 607 cm^{-1} band can only be seen in the difference spectrum obtained by subtracting away the silicon phonon bands by using a reference sample. And it is suggested the best way is to use the test and reference specimens that are polished on both sides and are exactly matched in thickness (about 2 mm). Another difficulty is the carbon absorption band is considerably narrower (full-width at half-maximum at room temperature is 6 cm^{-1}) compared to the oxygen band (full-width at half-maximum at room temperature is 31 cm^{-1}). Therefore the carbon absorption band has to be recorded with a higher spectral resolution. In silicon samples containing oxygen and relatively large amount of carbon, carbon-oxygen complexes with their own characteristic infrared absorption bands are present [Pradhan 87].

3.4.3 Experiment Set Up

Figure 3.24 shows a Michelson interferometer for transmissive FTIR spectroscopy measurement used in this work. Radiation leaves the source and reaches the beam splitter (BS). Part of the beam passes through the BS and is reflected from a fixed mirror M1, whereas another part is reflected from the BS and then from mirror M2, which is movable. As M2 moves, it changes the difference in length Δ between the paths the two light beams traverse. When the beams recombine they produce an intensity I(Δ) which depends on Δ, called the 'interferogram'. Then it continues through the sample to a detector, whose output is processed by a computer. The computer performs a Fourier transform to recover intensity versus wavenumber. To measure the source spectrum the sample shown in Figure 3.24 is removed. The ratio of the two quantities gives the wavenumber-dependent transmission coefficient.

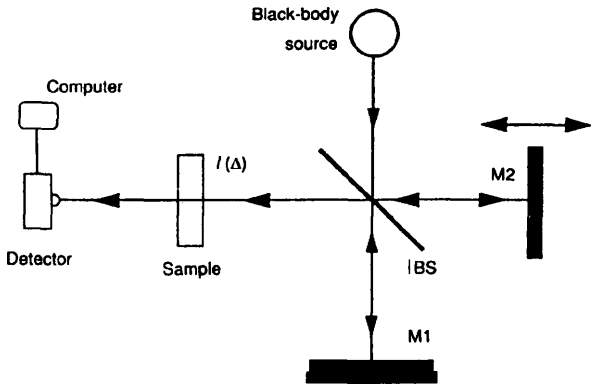

Figure 3.24 Michelson interferometer for transmissive FTIR spectroscopy.

3.5 Transmission Electron Microscopy (TEM)

The most direct way to analyze a crystal defect is to "look at" it. Transmission Electron Microscope (TEM) acts as a high resolution, high magnification microscope which allows the local structure of a solid to be investigated on a nanometer scale (even on an angstrom scale using high resolution TEM). In many ways electron optics are the same as light optics. But one obvious difference between electrons and light is that the wavelengths of electrons which depend on the electrons' energy are shorter than that of the light with a factor of many thousands. This means electrons can provide much higher resolution and magnification. However since electrons are much more strongly scattered by gases compared with light their paths must be evacuated to a vacuum better than 10^{-3} Pa. Figure 3.25 is a schematic drawing of a typical TEM system.

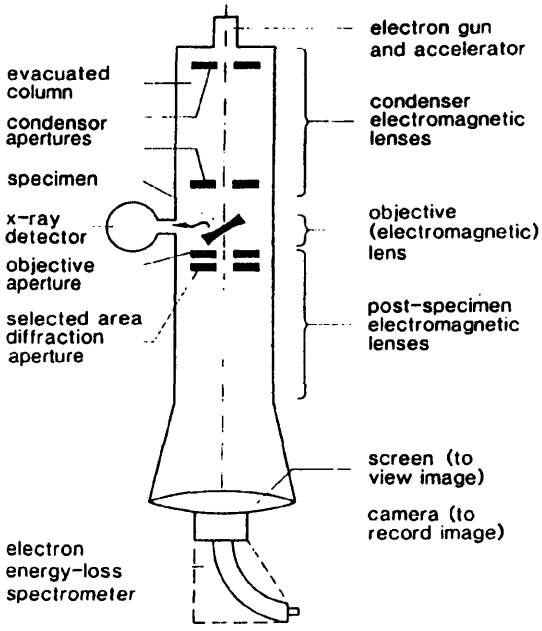

Figure 3.25 Schematic drawing of a typical TEM system.

The system basically consists of an assembly of electromagnetic lenses arranged in a vertical column with an electron source normally positioned at the top of the instrument and a fluorescent screen at the bottom of the column. Electrons produced at the gun are

accelerated down the column by a high voltage. These electrons are collimated and converged by apertures and electromagnetic lenses located immediately below the electron source which constitute the condense lens system. Its setting determines the intensity of illumination on the specimen by controlling the area of the specimen hit by the beam. Below the condenser lenses lies the specimen chamber. The specimen is mounted in a special holder and inserted into the evacuated column through an airlock. The specimen area examined must be very thin so that the electrons are able to pass through it. Electrons which emerge from the lower side of the specimen are focused by the objective lens (OL). The optics is shown in Figure 3.26.

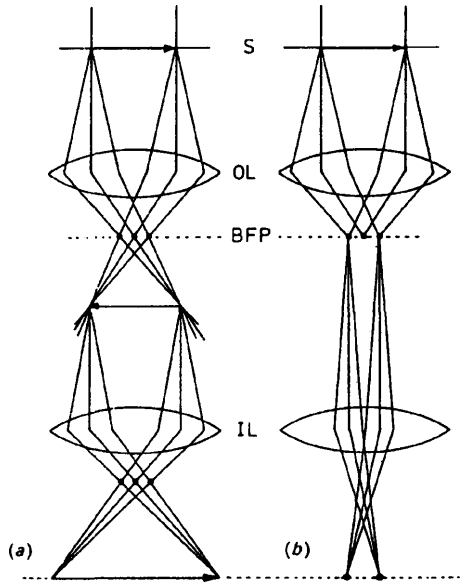

Figure 3.26 The objective and first intermediate lenses. OL is objective lens, BFP is back focal plane and IL is intermediate lens.
(a) Image mode
(b)Diffraction mode

The intermediate (or diffraction lens) can usually be switched between two settings, shown in Figure 3.26 (a) and (b). In the image mode it is focused on the image plane

of the objective (Figure 3.26 (a)) lens and the magnification of the final image on the microscope screen is then controlled by the strength of the remaining projector lenses. In the diffraction mode the intermediate lens are on the backfocal plane of the objective lens (Figure 3.26 (b)). In order to make the diffraction pattern visible, the intermediate lens is refocused on the back focal plane of the objective lens and the diffraction pattern is passed to the projector system. When a camera is used it is normally located under the removable fluorescent screen.

3.6 Rutherford Backscattering Spectrometry (RBS)

Rutherford backscattering spectrometry (RBS) has been a widely used analysis technique in material science since the late '60s [Chu 73]. It is a high-energy (MeV range of energies) ion beam technique which irradiates an unknown target with a mono-energetic beam of ions of hydrogen, helium or any other light elements. Backscattered particles coming from the target as a result of the interaction of the beam with the target are detected and energy analyzed. The results are presented as an energy spectrum from which we can determine the atomic mass of an unknown target and its concentration depth profile. Normally, RBS is associated with the analysis of amorphous materials only. If the ion beam impinges on an ordered sample in a nonrandom direction, for example, along a crystalline axis, channeling effect occurs. This effect may be used to yield information about the sample structure or lattice location of impurities.

A typical experiment set up is shown in Figure 3.27. Particles from the accelerator are

selected and collimated by a magnetic analyzer and collimator. Samples are located in the target chamber and energetic particles coming out from the target are detected and analyzed. The scattering chamber and the beam tube need to maintain a vacuum of the order of 10^{-5}-10^{-6} Torr for work in the high and medium energy ranges.

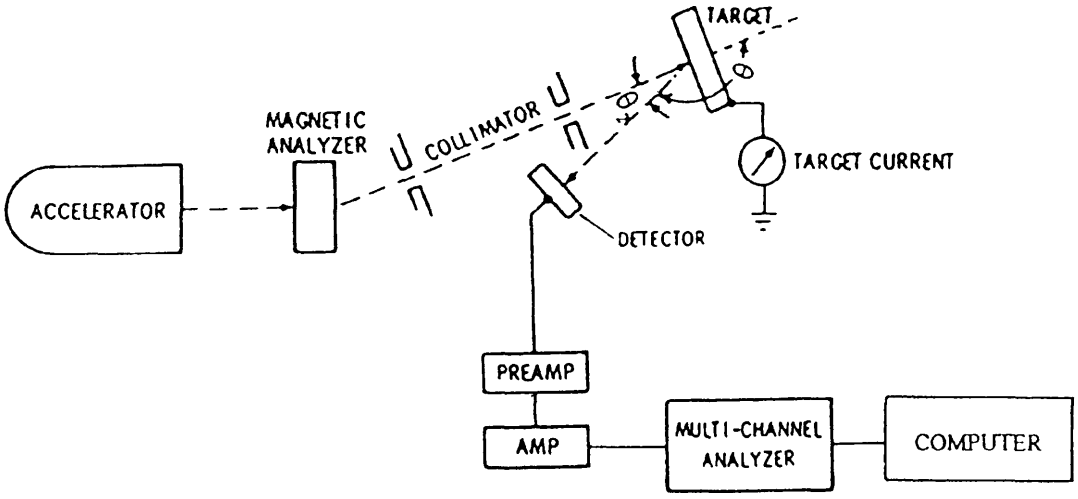

Figure 3.27 Schematic diagram of RBS system

References

[Blood 92] Blood P. and Orton J.W., in *The Electrical Characterization of Semiconductors: Majority Carriers and Electron States*, Academic Press, 1992, pp 585

[Bosomworth 70] Bosomworth D. R., Hayes W., Spray A. R. L. and Watkins G. D., *Proc. R. Soc. London, Ser. A 317*, 1970, pp 133

[Chu 73] Chu W. K., Mayer J. W., Nicolet M. A., Buck T. M., Amsel G. and Eisen F., *Thin Solid Films, 17*, 1973, pp 1

[Colley 87] Colley P. McL. and Lightowlers E. C., *Semicond. Sci. Technol., 2*, 1987, pp 157

[Efeoğlu 93] Efeoğlu H., *Ph.D thesis*, University of Manchester, 1993, pp 3-32

[Gaworzewski 84] Gaworzewski P., Hill E., Kirochi F. G. and Vecserny'es L., *Phys. Status Solidi 85*, 1984, pp 133

[Hawkins 89] Hawkins I. D., *Ph.D thesis*, University of Manchester, 1989

[Henry 73] Henry C. H., Kukimoto H., Miller G.L. and Merritt F. R., *Phys. Rev. B7*, 1973, pp 2499

[Kaniewski 92] Kaniewski J., Kaniewska M. and Peaker A. R., *Appl. Phys. Lett. 60(3)*, 1992, pp 359

[Kimerling 74] Kimerling L. C., *J. Appl. Phys., vol 45, no. 4*, 1974, pp 1839

[Lang 74] Lang D. V., *J. Appl. Phys., vol. 45, no. 7*, 1974, pp 3023

[Macfarlane 59] Macfarlane G. G., Lean T. P., Quarrington J. E. and Roberts V., *J. Phys. Chem. Solids 8*, 1959, pp 388

[Miller 77] Miller G. L., Lang D. V. and Kimerling L. C., *Ann. Rev. Mater. Sci.*, 1977, pp 377

[Newman 65] Newman R. C. and Willis J. B., *J. Phys. Chem. Solids 26*, 1965, pp 373

[Peaker 89a] Peaker A. R. and Hamilton B., *Electrochemical Society Symposium*, Sept. 1989 (Berlin).

[Peaker 89b] Peaker A.R., Hamilton B., Lahiji G. R., Ture I. E. and Lorimer G., *Mater. Sci. Eng. B 4*, 1989, pp 123

[Shaklee 70] Shaklee K. L. and Nahory R. E., *Phys. Rev. Lett. 24*, 1970, pp 942

[Tajima 77] Tajima M., *Jpn. J. Appl. Phys., 16*, 1977, pp 2265

[Takagi 62] Takagi S., *Acta Cryst., 15*, 1962, pp 1311

[Vincent 79] Vincent G., Chantre A. and Bois D., *J. Appl. Phys., vol. 50*, 1979, pp 5484

[Vouk 77] Vouk M. A. and Lightowlers E. C., *J. Phys. C 10*, 1977, pp 3689

Chapter 4 Defects in Ge^+ Implanted and Annealed Silicon

4.1 Introduction

4.1.1 Brief Theory of Ion-Implantation

Ion implantation of semiconductor was developed extensively during the 1960s [Gibbons 68] since then it has become a more and more important technique in the fabrication of integrated circuits. Ion implantation offers many advantages over conventional diffusion techniques. The most important advantage is the ability to control with precision the thickness and doping level of implanted layers by varying the energy and dose of the ion species. Another advantage is that the implanted dopant can have much less lateral spread outside the masked area than in the case of the diffusion processes. Potentially this allows devices to be fabricated with features of smaller dimensions. During ion implantation, the ions are accelerated and directed at the silicon target, enter the crystal lattice, bombarding the crystal atoms and meanwhile lose energy, finally coming to rest at some depth. Although the travelling path of each implanted ion is random, their average behavior can be well predicted. There is a distribution of ion ranges with depth from the sample surface which is approximately Gaussian. Thus, implanted atomic profiles can be described by a projected range R_P (representing the depth at which most ions stop, and also the distance

at which the profile along the implantation direction has the maximum value) and the standard deviation of this range known as the projected straggle, ΔR_p. The ions are also scattered to some degree along the direction perpendicular to the incident direction, and the statistical fluctuation along this direction is called the projected lateral straggle, $\Delta R_\perp$. They are illustrated in Figure 4.1.

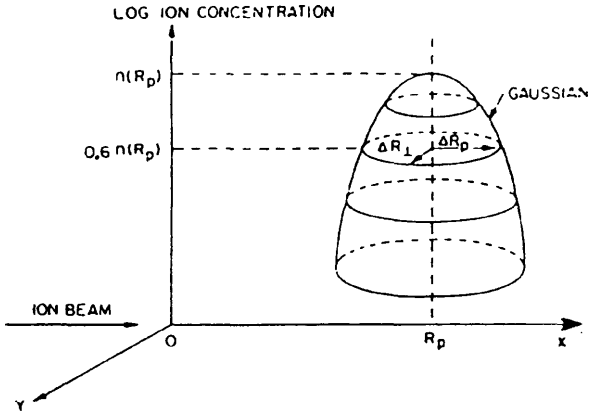

Figure 4.1 Two-dimensional distribution of the implanted atoms. *After Sze [Sze 85]*

The most successful model for predicting implantation profiles in amorphous material is the so called LSS (Lindhard, Schaiff, Schiott) model. Using R_p and ΔR_p the distribution of the implanted ions could be described as:

$$n(x)=\frac{\phi}{\sqrt{2\pi}\Delta R_p}\exp[\frac{-(x-R_p)^2}{2\Delta R_p{}^2}] \qquad (4.1)$$

where x is the depth of ion in the target and ϕ is the dose (in number of implanted

ions/cm^2). R_P and ΔR_P can be obtained using LSS model. The value of ΔR_P is calculated in terms of R_P, the mass of the implanted ions M_1 and the target atoms M_2 according to the approximate expression:

$$\Delta R_P = \frac{2R_P}{3}\left[\frac{\sqrt{M_1 M_2}}{M_1 + M_2}\right] \tag{4.2}$$

The concentration is at its maximum at R_P and equation (4.2) at $x = R_P$ reduces to:

$$n_{max} = \frac{\phi}{\sqrt{2\pi}\Delta R_P} = \frac{0.4\phi}{\Delta R_P} \tag{4.3}$$

The model fits experiment data well for all implantation near the peak. However, significant asymmetries begin to appear in experimental implant profiles once the concentration levels drop by a factor of 10 below the peak value. In the case of the implantation of heavy atoms more will come to rest at a distance further away from the surface than R_P and there will be a tail extending deeper into the bulk region.

Channelling may occur when implantation is done into crystalline materials because the ions are scattered in low index crystallographic directions and penetrate deeply within the material before coming to rest. This process is difficult to model theoretically and attempts are made to eliminate it when processing semiconductors. Channelling is particularly detrimental when trying to implant shallow junctions. If the target is made amorphous before implantation, the channelling can be totaliy suppressed. During recent years,

preamorphisation of silicon by implantation of group IV atoms, such as silicon and germanium, have been used in device fabrication processes. The regrowth of amorphous layers by solid phase epitaxy (SPE) starts from the underlying crystalline substrate and proceeds towards the surface. Annealing also functions to activate dopant atoms by putting them onto substitutional lattice sites.

4.1.2 Literature Survey on Defects in Amorphized and Annealed Silicon and Overview of Present Work

Annealing of the amorphous layer generates the so called end of range (EOR) defects such as dislocation loops [Jones 88] at the region just beyond the original amorphous/crystalline (α/c) interface. The EOR defects are due to the condensation of the excess self-interstitials created by the amorphizing implant [Thornton 88]. If the end of range dislocation loops are in the vicinity of the active region of the device the associated electrically active deep states will result in high leakage current and short minority carrier lifetime and can degrade device performance [Brotherton 89][Zhang 93].

The removal of the EOR defects is found to be affected by the presence of sinks and sources of the self-interstitials as well as their location relative to the sample surface [Ajmera 86][Jones 88]. But in most cases they are very thermally stable and cannot be easily removed by annealing. Point defects related to the recoil implanted Si interstitials beyond the α/c interface are often observed. They can cause high leakage current and

transient enhanced diffusion of dopant atoms such as boron [Servidori 87]. Their thermal stability is relatively low compared with that of EOR defects as such that they can be removed by annealing at 800°C [Brotherton 89].

In the past limited studies have been carried out on (1) evolution of defects during annealing; (2) influence of background impurities on implantation related residual defects. In order not to complicate the situation by involving any dopant implantation this chapter only deals with the preamorphisation implantation using Ge^+ ions.

In **section 4.2** of this chapter defects evolution in n-type Ge^+ implanted and furnace annealed silicon (chemical vapor deposition (CVD) epitaxy Si on CZ substrate) was studied as a function of annealing temperature. This study is very important in the sense that it helps to understand the formation of the EOR and related defects and to understand their roles in affecting the electrical and optical properties.

Capacitance-voltage (C-V) and current-voltage (I-V) measurements were used to obtain the apparent free carrier concentration depth profiles and reverse bias leakage current respectively. These were directly affected by the presence of deep level defects. Deep level transient spectroscopy (DLTS) technique was used to find the activation energy and the concentration depth profile of each defect. Photoluminescence (PL) was carried out to investigate the radiative centers related to defects and impurities and to estimate the general quality of the implanted and annealed silicon. All these results were then compared with published data. A tentative identification and proposed evolution of these defects is

discussed and a correlation between the defects and the measured electrical properties has been established.

A study of the role of background impurities (oxygen) in p-type Czochralski silicon on the formation and evolution of implantation related residual defects is discussed in **section 4.3**. The role of nitrogen and oxygen on the EOR defects was mentioned by Maher [Maher 86] as a possible cause for defect "hardening" during rapid thermal annealing (RTA). Lorenz [Lorenz 91] studied the effect of oxygen on the formation of EOR defects in CZ (with various oxygen concentrations) and FZ (as 'low oxygen') wafers subjected to Ge^+ implantation and concluded that the conditions for defect formation favored samples with high oxygen concentrations.

In section 4.3 the effect of background oxygen concentration on the residual defects after Ge^+ implantation and rapid thermal annealing (RTA) was studied in terms of optical, electrical and structural properties by means of PL, C-V, DLTS and TEM techniques.

4.2 Defects Evolution in Ge^+ Preamorphized and Furnace Isochronal Annealed N-type Si (CVD Epitaxy Si on CZ substrate)

4.2.1 Sample Information and Experimental Details

Phosphorous doped (100) CVD epitaxy on CZ substrate silicon wafers (dopant

concentration is N_D= 2.75 x 10^{15} cm^{-3}) were amorphized by Ge^+ implantation with an amorphized layer of thickness ~ 0.5 μm. The implantation was carried out at an energy of 400 keV with dose 1 x 10^{15} cm^{-2}. The slices were tilted so that the surface normal was inclined at 7° with respect to the direction of incident ion beam in order to reduce direct channelling effects. The beam current density was kept at 0.046 μA cm^{-2} to avoid heating. The projected range of 400 keV Ge^+ ions in Si is 260 nm (TRIM simulation [Ziegler 85]).

The wafer was cleaved into rectangles of ~ 1cm x 2cm. After standard Si cleaning using H_2O : H_2O_2 : NH_4OH (= 5:1:1) and H_2O : H_2O_2 : HCl (= 6:1:1) [Kern 70] solutions (for organic and metallic contamination removal respectively), the samples were annealed in a furnace at a different temperature for each piece. The temperatures used were 750°C, 775°C, 800°C and 825°C with an anneal time of 10 minutes in a flowing nitrogen ambient. The annealing and the ion implantation conditions are summarized in Table 4.1.

Sample Number	Annealing Temperature (°C)	Annealing Time (minutes)	$^{74}Ge^+$ dose (cm^{-2})	$^{74}Ge^+$ energy (keV)
1	750°C	10	$1x10^{15}$	400
2	775°C	10	$1x10^{15}$	400
3	800°C	10	$1x10^{15}$	400
4	825°C	10	$1x10^{15}$	400

Table 4.1 Ion-implantation and annealing conditions for samples studied in section 4.2

For electrical measurements gold was evaporated on the front to form Schottky barrier

diodes and aluminum was evaporated on the back to form Ohmic contacts. Photoluminescence measurements were carried out at 13 K using excitation by the 514 nm line of an Ar^+ laser at 98 mW (details of PL experiment set up can be found in chapter 3, section 3.2.2). Room temperature C-V measurements were carried out at 1MHz. A Bio-Rad DL4600 system was used for the DLTS measurements (refer to chapter 3, section 3.1.3.2.2 for details). The concentration depth profiles was derived using a technique described in Chapter 3 section 3.1.3.1.4.

4.2.2 Results

4.2.2.1 Photoluminescence (PL) Studies

Photoluminescence spectra of all the samples listed in Table 4.1 are plotted in Figure 4.2.

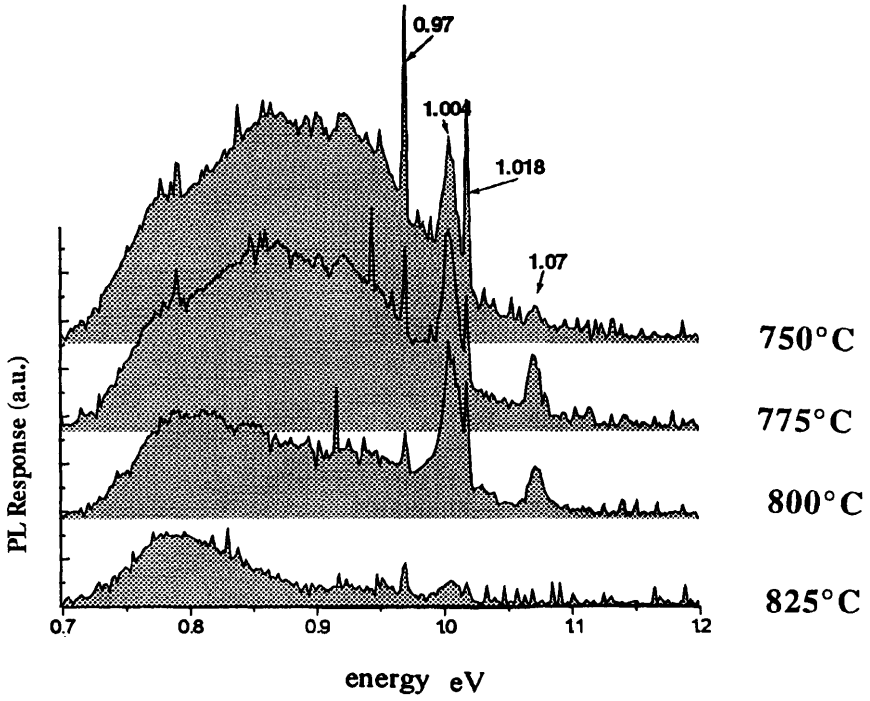

Figure 4.2 PL spectra of samples annealed at 750°C, 775°C, 800°C and 825°C.

The samples annealed at 750°C and 775°C showed a big broad peak centered at around 0.88 eV. The sample annealed at 800°C resulted in a change of the shape of the PL spectrum. The dominant feature was no longer the previous big broad peak, instead there was a smaller broad peak centered around 0.79 eV. This effect was further enhanced in the sample annealed at 825°C. Fine PL lines located at 0.97 eV, 1.004 eV, 1.018 eV and 1.07 eV were also observed and their intensities are summarized in Table 4.2.

Sample Number	0.97 eV line intensity	1.004 eV line intensity	1.018 eV line intensity	1.07 eV line intensity
1	1.46	0.81	1.02	0.12
2	0.77	0.83	0.55	0.32
3	0.35	0.74	0.57	0.2
4	0.18	0.1	0.09	0.07

Table 4.2 PL intensities of 0.97 eV line, 1.004 eV line, 1.018 eV line and 1.07 eV line observed in the samples annealed at 750°C, 775°C, 800°C and 825°C.

4.2.2.2 Capacitance-Voltage (C-V) and Current-Voltage (I-V) Studies

Room temperature apparent free carrier concentration profiles derived from capacitance-voltage measurements of all the samples are shown in Figure 4.3. A high concentration of excess carriers in the implanted samples annealed at 750°C, 775°C are clearly seen. The concentration of these excess carriers decreased greatly in the sample annealed at 800°C. In the sample annealed at 825°C they reduced to a negligible level.

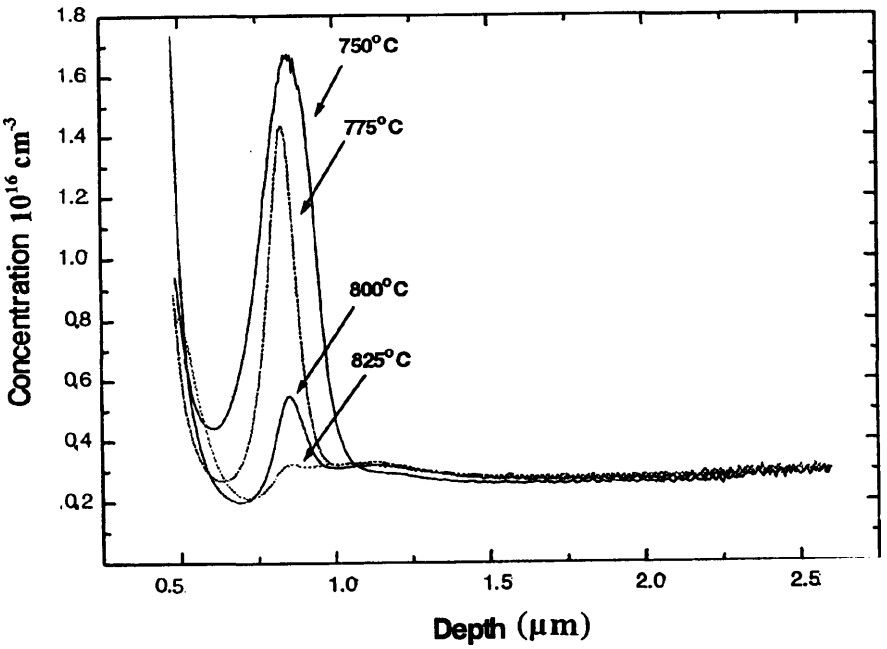

Figure 4.3 Apparent free carrier concentration depth profiles derived from capacitance-voltage measurements in the samples annealed at 750°C, 775°C, 800°C and 825°C .

Similar to the C-V results the room temperature leakage currents (from I-V measurements) reduced remarkably in the samples annealed at 800°C and 825°C. This is shown in Figure 4.4.

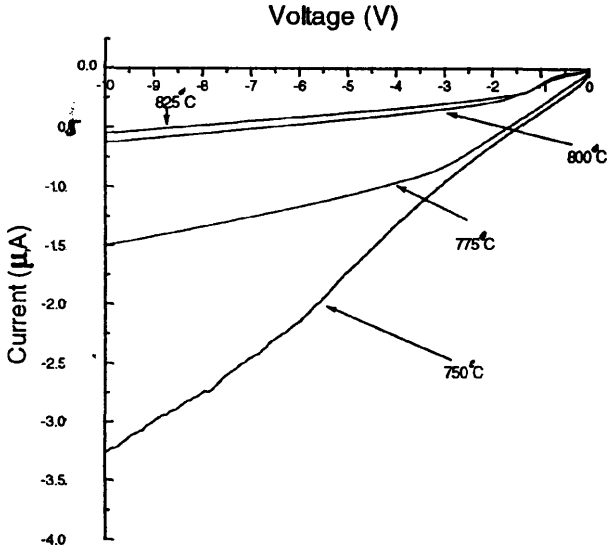

Figure 4.4 Reverse bias leakage currents of samples annealed at 750°C, 775°C, 800°C and 825°C . (DLTS measurements were carried out at voltages < 4.5 volts).

4.2.2.3 Deep Level Transient Spectroscopy (DLTS) Studies

4.2.2.3.1 Thermal Emission Characteristics

There are seven majority traps labelled A, B, C, D, E, F and G detected in the germanium implanted materials. Because of the localized spatial distribution of each trap a range of measurement bias conditions (corresponding to various depths) was used for each sample to detect all the traps. Figure 4.5 (a), (b), (c) and (d) shows a family of DLTS spectra for each of the samples annealed at 750°C, 775°C, 800°C and 825°C respectively.

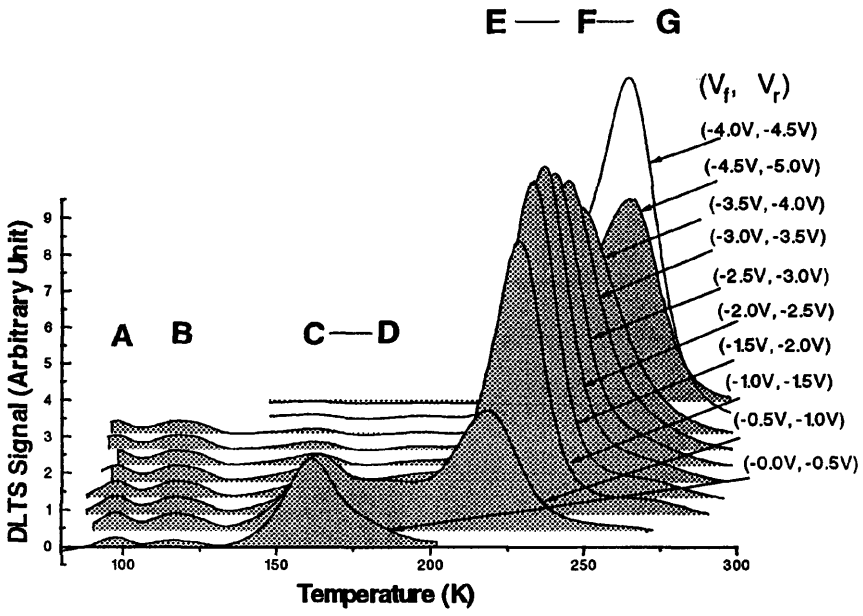

Figure 4.5(a) A family of DLTS spectra of the sample annealed at 750°C. The numbers in brackets represent the bias conditions of measurements (corresponding to various depths of each trap). Traps A, B and C are clearly seen. There is a small indication of trap D when the measurement condition is V_f= - 0.5V (V_f stands for forward bias) and V_r= - 1V (V_r stands for reverse bias). Traps E, F and G were not individually resolved.

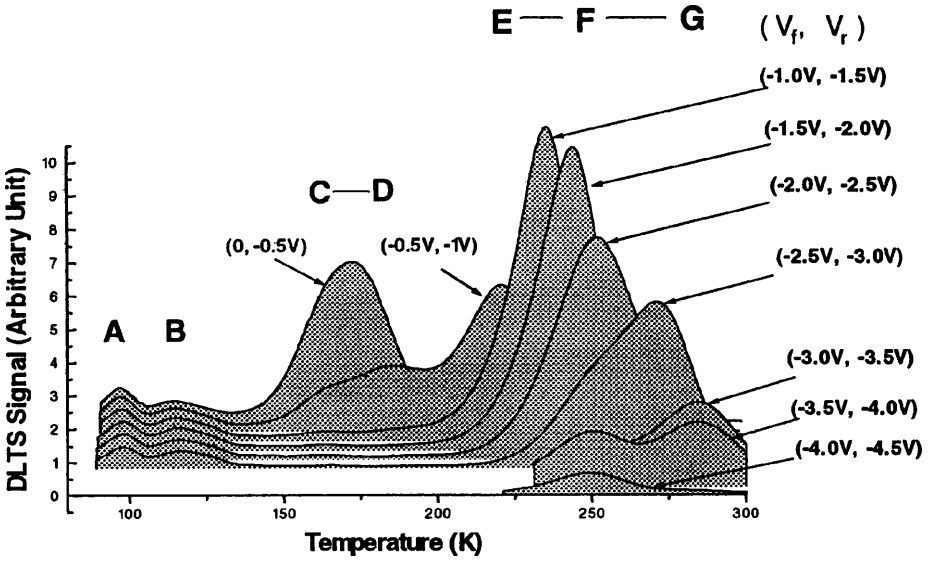

Figure 4.5(b) A family of DLTS spectra of the sample annealed at 775°C. Traps F and G are clearly resolved in measurements at higher bias conditions.

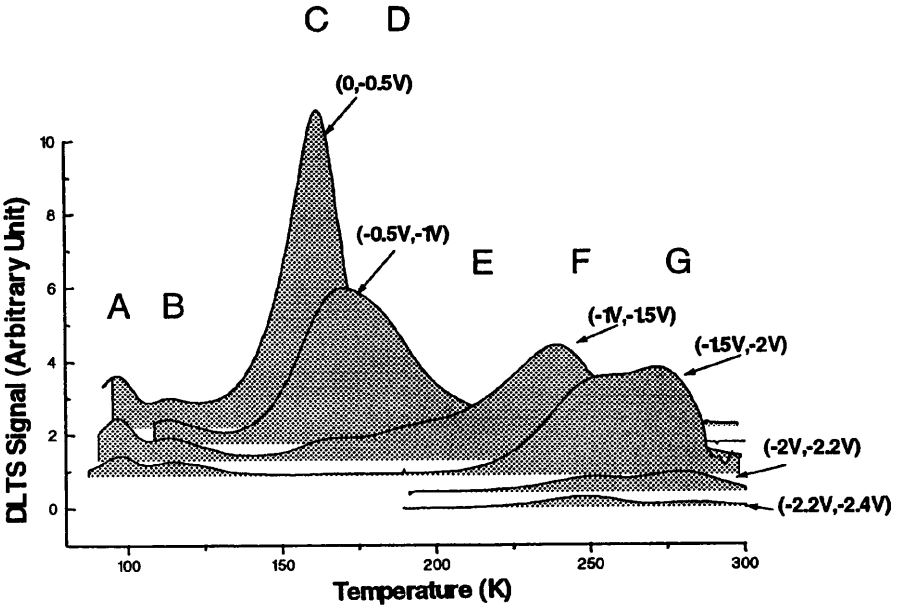

Figure 4.5(c) A family of DLTS spectra of the sample annealed at 800°C. Unlike the samples annealed at 750°C and 775°C, traps located at higher temperatures are no longer the dominant ones.

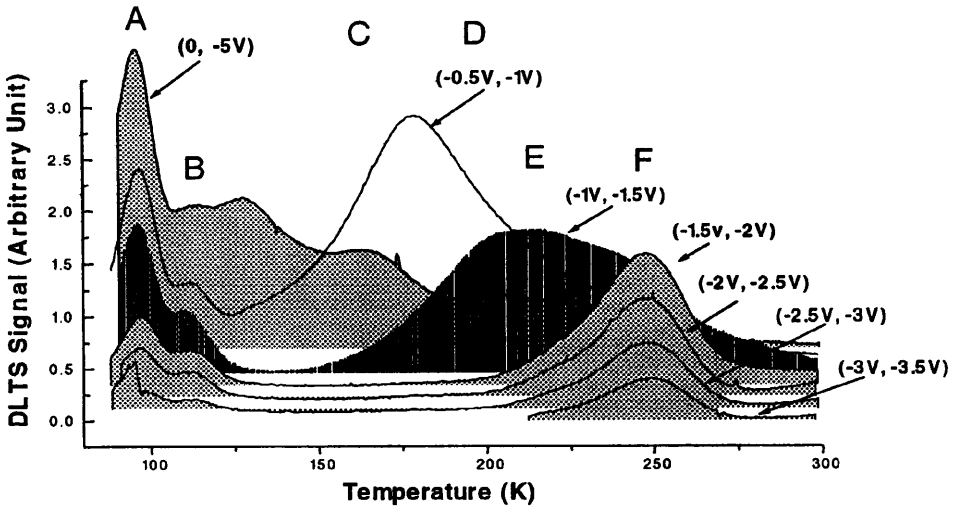

Figure 4.5(d) A family of DLTS spectra of the sample annealed at 825°C. In this sample the coexistent of both traps E and F at a bias condition V_f= - 1V and V_r= - 1.5V can be seen.

The activation energy (denoted as E_a) of electron emission of all the traps (excluding trap D) are given in Table 4.3. Figure 4.6 shows the Arrhenius plot of thermal emission rates of them.

Trap Name	A	B	C	E	F	G
Peak Temperature at 100/s	94	113	153	210	242	278
E_a (meV)	158	200	286	440	506	640

Table 4.3 List of activation energy values of traps by DLTS measurements

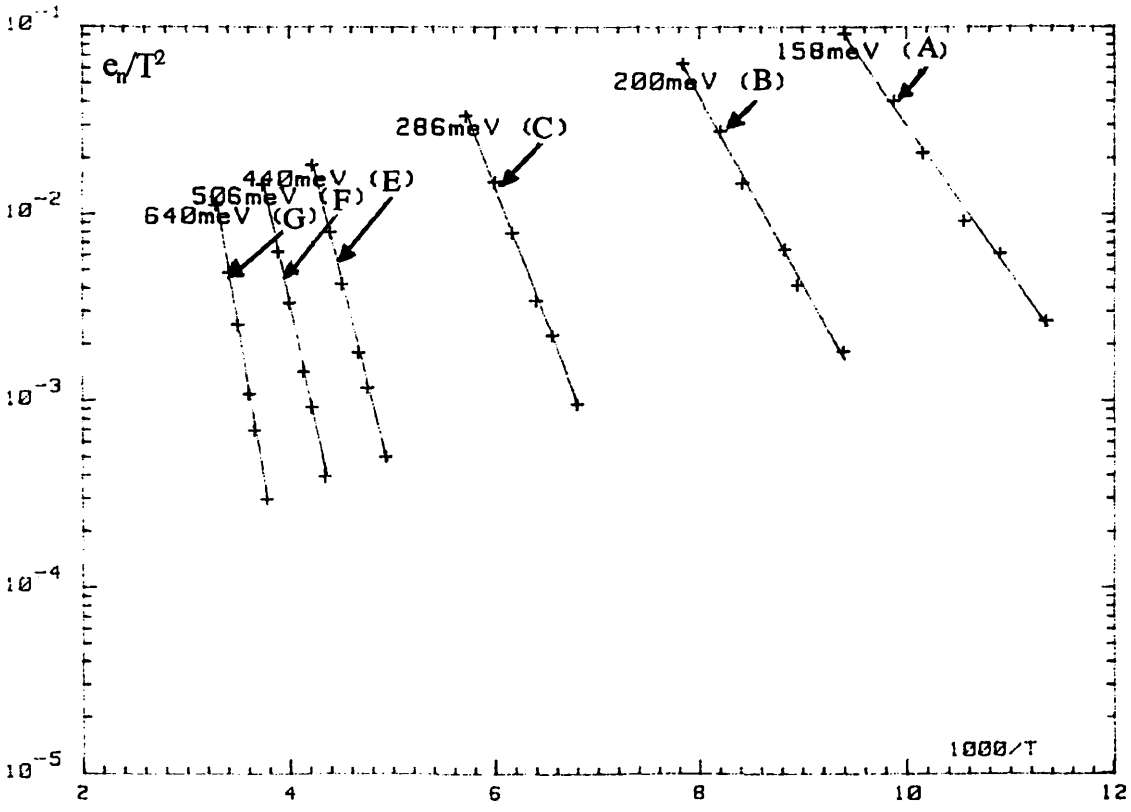

Figure 4.6 Arrhenius plot of thermal emission rates for traps A, B, C, E, F and G.

4.2.2.3.2 Concentration Depth Profiles

The concentration depth profiles of traps A, B, C, E and F in the sample annealed at 825°C are shown in Figure 4.7 (trap G does not exist in this sample and trap D is not clearly resolved hence not available).

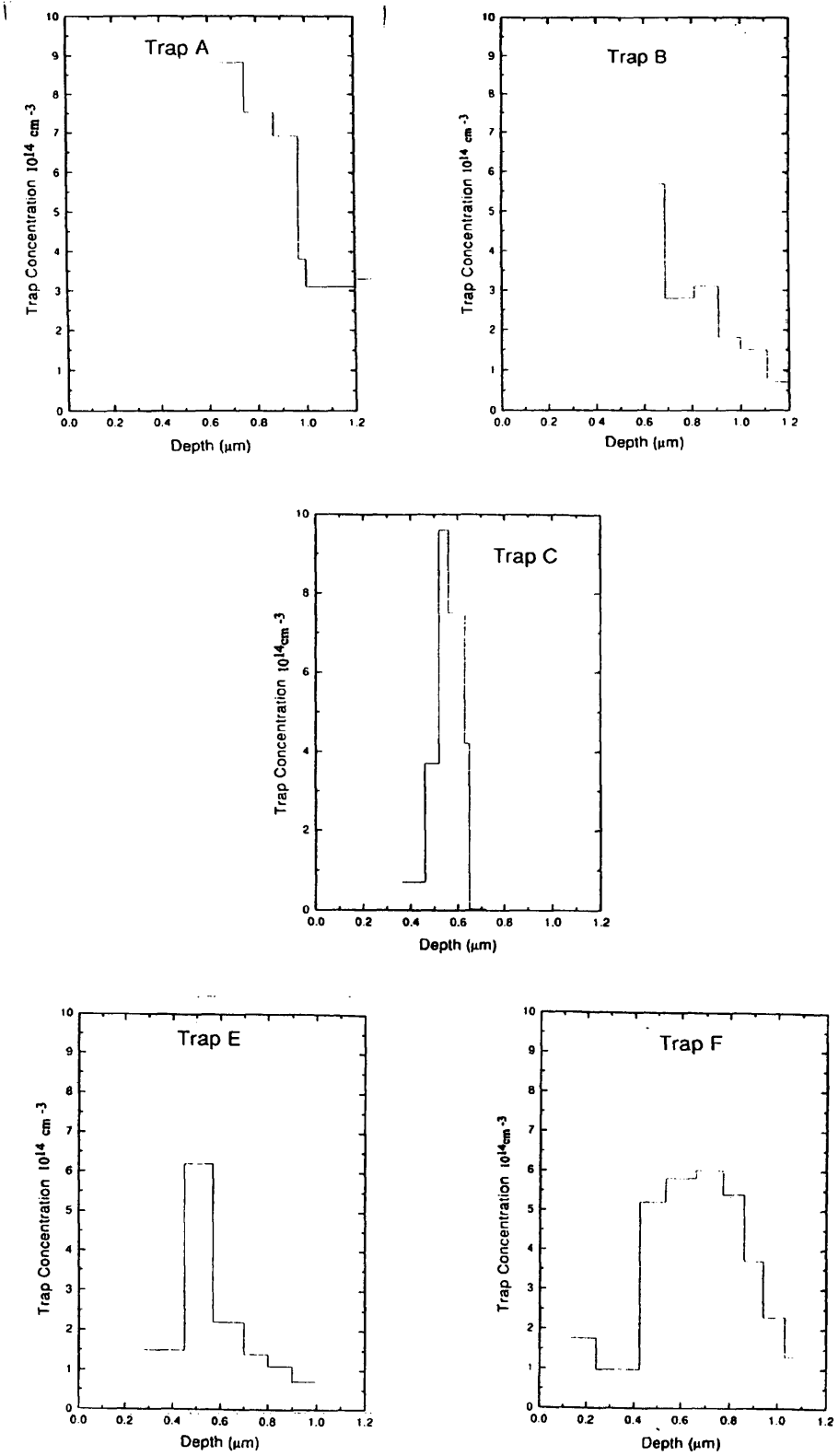

Figure 4.7 Concentration depth profiles of traps A, B, C, E and F in the sample annealed at 825°C.

Depth profiles of traps C, E, F and G in the samples annealed at 750°C, 775°C and 800°C could not be derived due to the fact that their concentrations were too high (>10N_D) for quantitative evaluation (the concentrations of traps A and B are not too high for a quantitative evaluation in these three samples). Therefore only qualitative descriptions will be given below (the descriptions will include traps A and B for consistence):

Trap E and F: very difficult to obtain depth profiles for traps E and F individually in these samples because in addition to high concentration problem mentioned earlier their activation energy as well as their physical locations were very close to each other that often they could not be resolved from the DLTS spectra. However the approximate range of each trap was obtained by judging the depth at which they appeared and disappeared. The results are presented in Table 4.4.

	Trap range in 750°C sample (μm)	Trap range in 775°C sample (μm)	Trap range in 800°C Sample (μm)	Trap range in 825°C Sample (μm)
Trap E	0.7 - 0.8	0.6 - 0.7	0.5 - 0.6	0.4 - 0.6
Trap F	0.7 - >0.9	0.6 - >0.9	0.5 - >0.9	0.4 - >0.9

Table 4.4 Approximate ranges of traps E and F in samples annealed at 750°C, 775°C and 800°C.

Trap G: the concentration in the samples annealed at 750°C, 775°C and 800°C decreased with depth rapidly (bearing in mind we could not detect very shallow regions). The observations were made within a depth range of at least 0.75 μm. In the sample annealed

at 825°C this trap disappeared completely.

Trap C: In the samples annealed at 750°C, 775°C and 800°C the concentration of it decreased with depths rapidly but we were not able to obtain the maximum values (if they existed) because sample resistivity was too high for monitoring the shallower depths where the maximum concentrations might locate. The observations were made within a depth range of at least 0.7 μm. Upon annealing at 825°C the concentration of this trap reduced dramatically. We can now detect the maximum concentration (refer to Figure 4.7) which is 9.6 x 10^{14} cm^{-3} and locate at ~ 0.55 μm.

Trap A and B: DLTS profile results showed that the concentration distributions of traps A and B had the same trend in each sample. The concentrations increased with depth in the samples annealed at 750° C and 775° C. They decreased with depth in the samples annealed at 800°C and 825°C. These observations were made in regions at a depth between 0.8 μm and 1.4 μm (we were not able to reach smaller depths due to the limitation of wafer resistivity). The concentrations remained below 33% of the substrate doping in all cases.

4.2.3 Discussions

4.2.3.1 Optical Characteristics

Referring to Figure 4.2, the most obvious change in the PL spectra at the various anneal temperatures occurs in the sample annealed at 800°C. The dominant broad peak seen in the samples annealed at 750°C and 775°C changed shape in the samples annealed at 800°C and

825°C and the integrated intensity is reduced greatly. This is interpreted as the annealing out of a high population of point defects. This is in consistent with the electrical measurements where most of the non-radiative recombination centers were annealed out at 800°C.

Referring to Figure 4.2 and Table 4.2, the **1.018 eV** PL line from this work has the same energy as the reported W (or I1) peak in ion implanted and annealed Si [Kirkpatrick 76] or in neutron transmutation doped (NTD) Si [Tajima 81]. The W center in their paper was suggested to be intrinsic in nature. There were reports on variants of the W peak when the silicon was bombarded with He, Ne, Ar, Kr or Xe ions [Bürger 84]. It was suggested the modified peaks were due to the perturbation by the presence of the inert gas atoms as a result of the strain field created by them. According to the same principle it is possible that the **1.004 eV** line in this work is due to the modified W peak associated with Ge atoms.

The energy of the **0.97 eV** line in this work coincide with the energy of the reported 'G' line ('C_i-C_s' center with one interstitial carbon atom: C_i and one substitutional carbon atom: C_s) [Davies 88]. If it is true then the question to ask is where does the carbon atoms come from? This is because CVD materials should have a very small concentration of carbon atoms. However carbon contamination from ion implantation is possible. The other point to make is the 'C_i-C_s' center was reported to be destroyed by annealing at temperatures much lower than our annealing temperature, however we should bear in mind that it is still unknown what process is occurring during the annealing.

The **1.07 eV** line in our measurements has the same energy as one of the centers belonging to the 'S' series formed in heat treated CZ Si [Nakayama 81] or in CVD Si (grown on CZ substrate) with oxidation induced stacking faults in it [Evans 92]. The exact nature of the 'S' lines is still unknown, however they have been suggested to relate to oxygen and/or carbon impurities in the Si material. If it is the case the question to ask again is where the oxygen and/or carbon atoms come from in our CVD materials.

In order to answer the above questions, further PL studies should be pursued and a better condition should be established to produce well resolved PL lines (not superimposed on the broad bands).

4.2.3.2 Electrical Characteristics

Referring to Figure 4.3 which shows the apparent free carrier depth profiles derived from C-V measurements, the most obvious feature is the large excess donor concentration in the region of the implant tail. This is dramatically reduced on annealing at temperatures in excess of 800°C. Figure 4.4 illustrated that the Schottky barriers fabricated on materials annealed below 800°C had very high reverse bias leakage currents. A comparison of the C-V and I-V measurement results at this crucial annealing temperature, 800°C, implied that either the same deep level traps were responsible for both the excess donor concentration and the generation centers or there were two different kinds of traps with the same annealing characteristics.

The results of the DLTS depth profiles revealed that traps E and F were the only traps that had a remarkable concentration decrease upon annealing at 800°C. Therefore it was suggested that they were responsible for the excess donors observed in C-V depth profiles and were the generation centers causing the high reverse leakage currents. More detailed analysis will be given below.

Now consider trap E: Figure 4.8 shows the excess carrier concentration depth profile derived from C-V measurement of the sample annealed at 825°C (Figure 4.8 (a)) and the concentration depth profile of trap E derived from DLTS measurements in the same sample (Figure 4.8 (b)).

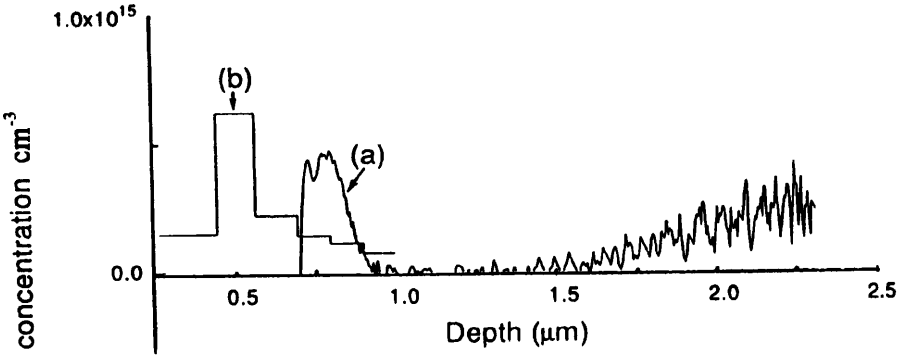

Figure 4.8 (a) Excess free carrier concentration depth profile derived from C-V measurement of the sample annealed at 825°C
(b) Concentration depth profile of trap E derived from DLTS measurements in the same sample

Assume trap E is a donor-like trap and its emission rate e_n satisfies the inequality $\omega(\Delta V_{osc}) > e_n > \omega(\Delta V)$. Where $\omega(\Delta V_{osc})$ is the changing rate of the oscillating voltage in the capacitance measurement which is 1MHz in this work. $\omega(\Delta V)$ is the changing rate of reverse bias voltage which is approximately 1Hz in this work. As long as the electron capture cross section of trap E, σ_n, satisfies: $4x10^{-14}cm^2 > \sigma_n > 4 \times 10^{-20}cm^2$, which is in consistent with most donor-like centers in n-type Si [Melvin 60]), the inequality $\omega(\Delta V_{osc}) > e_n > \omega(\Delta V)$ (using equation (3.22): $e_n=(\sigma_n<V_{th}>N_c/g)e^{-\Delta E/kT}$) is satisfied. We now can apply equation (3.13): $n_m(W) = N_T(y)\, y/W + n(W)$ (refer to Figure 3.1 (a) for the definition of W and y) to the present situation, and obtain that the concentration (maximum value) of the excess donors from the C-V profile should be 65% of the concentration (maximum value) of the real trap (trap E here). In fact our experiment data is 70% (Figure 4.8), which agrees well with theoretical prediction.

Since the DLTS depth profile (Figure 4.8 (b)) of trap E had a triangle distribution, from chapter 3 Figure 3.3 (b), we would see a shift of the real position of the donor maximum towards deeper region in the C-V profile. According to equation (3.7) in chapter 3 the shift of the peak caused by trap E would be 0.29 μm. The maximum donor concentration from the C-V profile in the 825°C sample was at 0.84 μm (Figure 4.8(a)). Therefore the actual maximum position correlated with trap E in C-V profile would be at 0.84μm-0.29μm=0.55μm. This result is in good agreement with the DLTS depth profile (Figure 4.8(b)).

Thermal emission characteristics and annealing behavior of trap E compared with literature

shows it is similar to electron traps in plastic deformed n-type silicon [Kimerling 79][Omling 85] [Kveder 82] where they were related to dislocation dangling bonds or kinks in the dislocations. Annealing of the plasticaly deformed samples between 650°C and 800°C resulted in a decrease of the EPR signal associated with the centers. The explanation was a core reconstruction to minimize the number of dangling bonds by grouping together to form bonds. The observed physical movements of trap E (in this work) as a function of anneal temperature from our DLTS depth profiles might suggest it was related to the core reconstruction process towards the stable dislocation loops at the α/c boundary.

The reason why trap E started at a point deeper than the α/c boundary (refer to Table 4.4) can be explained as follows: according to Seibt and co-workers [Seibt 92] the starting location of defects depended on the types of defects introduced. It stated in that paper that {111}-SFs and {113}-SFs (most of the a/2 <110> loops, which were often observed in ion implanted and annealed silicon, appeared to be the result of the unfaulting of {113} loops [Salisbury 81]) were the two commonly observed defects in ion-implanted and annealed silicon [Lambert 81]. A very low temperature annealing prior to SPE growth or storage at room temperature for several months [Myers 86] (our sample had been in storage for six months!) allowed the controlled deposition of Si_I into {113}-SFs. In this case the formation of the defects was found to start from the region of highest Si_I supersaturation [Seibt 92]. The highest Si_I supersaturation region, in this work, coincided with the region of trap E at low anneal temperatures.

The evolution from the supersaturation of point defects to dislocation loops was proposed

by Tan [Tan 81] via the intermediate defect configurations (IDC). According to this model the supersaturated point defects would first condense into a row configuration elongated in <110> which were the previously mentioned IDC's. The evolution into dislocation dipoles is driven by the formation of more perfect bond which subsequently evolve into <110> elongated dislocation dipoles and then at still higher temperatures into dislocations. These processes might well be related to the observed movements of trap E as a function of annealing temperature in this work.

Trap F: if we assume it is donor-like deep level and analyze its concentration profile in the same way as we did for trap E, we would conclude that the width of the excess donor peak from C-V measurement (Figure 4.8(a)) should be doubled. In another word trap F is not donor-like deep levels. Comparison of the thermal emission characteristics and the annealing behavior of trap F with the published data shows a similar electron trap in Ge^+ or Si^+ preamorphized and 600°C or 700°C annealed silicon [Ayres 87]. In that paper they related the defects to fundamental damage related Si_I beyond α/c boundary, however no identification was made there.

Trap G: this trap was annealed out upon annealing at 825°C. Deep levels with similar thermal emission characteristics and annealing behavior was observed in Si^+ or Ge^+ implanted annealed samples in Brotherton's work [Brotherton 89].

Another trap similar to G was found in plasticaly deformed Si [Kimerling 79] and there it was suggested to be an acceptor-type deep level and was assigned to point defect clusters.

Trap C: it is similar to one of the major electron states reported by Kimerling [Kimerling 79] where it was suggested to be acceptor-like and was related to point defects located within, or very close to, the dislocation core. This may be used to explain the DLTS depth profile of trap C in this work. A similar deep state was also reported in Ge^+ or Si^+ preamorphized and 600°C and 700°C annealed silicon [Ayres 87] and no identification was made in that paper.

Trap A: it has very similar thermal emission characteristics to a trap reported in Au implanted and annealed (850°C for 2 hours) n-type silicon [Wang 76]. It was suggested in that paper that it might resulted from the defect-defect or defect-Au interactions.

Trap B: the thermal emission characteristics and annealing behavior of trap B compared with the literature shows it was similar to defects referred to as 'group A' [Omling 85] where they were suggested to be related to dopants in or around the dislocation core.

4.2.3.3 Concentration of Traps When a High Level of Them are Present

When the trap concentration exceeds $0.1N_D$ the emission transient will no longer be exponential (see chapter 3 section 3.1.3.2.1). This will result in errors in the value of trap concentration and possibly in the activation energy. There are no errors regarding the activation energies in this work because they were always obtained under the condition that $N_T \leq 0.1N_D$. Traps C, E, F, and G in the samples annealed at 750°C, 775°C and 800°C had

concentrations much higher than the shallow doping level. This is why we could not obtain accurate values for their concentration profiles, as stated in the results section. However according to Brotherton [Brotherton 89] even when the trap concentration was 10 times the shallow doping level the errors would be less than a factor of two and so some qualitative conclusions are possible (as we did in the results section).

4.2.4 Conclusions

Seven deep level defects labelled A, B, C, D, E, F and G were detected by DLTS measurements in Ge^+ implanted and furnace annealed n-type silicon (CVD epitaxy Si on CZ substrate). The evolution of these defects was studied as a function of anneal temperature in terms of their change in concentration depth profiles and their influence on the optical and electrical characteristics.

Apparent carrier concentration depth profiles derived from room temperature capacitance-voltage measurements revealed a high concentration of excess donors in addition to the shallow doping in the samples annealed at temperatures lower than 800°C. Current-voltage measurements showed high reverse leakage currents in those samples. Furthermore the 800°C anneal resulted in a remarkable reduction of the broad peak in the photoluminescence spectrum which correlated well with the electrical measurements in the sense that the broad peak could be caused by a high population of point defects.

A general picture of how the defects evolve and which defects affected the electrical properties was established. Trap E is thought to be responsible for the excess donors observed in the C-V depth profiles. Traps E and F are thought to be responsible for the high reverse leakage currents from I-V measurements (trap F may be a more efficient recombination center because it is nearer to the middle of the energy gap). Defects such as trap C might be resulted from impurity-dislocation interactions from the DLTS depth profile result and a comparison with literature.

4.3 Effects of Oxygen Concentration on the Residual Defects in Ge^+ Implanted and Rapid Thermal Annealed P-type CZ Silicon

4.3.1 Sample Information and Experimental Details

Three Czochralski (CZ) and one float zone (FZ) boron doped p-type (100) silicon wafers were doubly implanted with germanium at 800 + 400 keV to produce an amorphized layer of about 0.75 μm thick.

The concentrations of oxygen were measured using Bio-Rad STS-60A Fourier Transfer Infrared Spectrometer calibrated according to the new ASTM standard [ASTM 85]. The FZ wafer was used as the reference for the oxygen measurements. No reference wafer for the carbon concentration measurement was available The only information available among the three CZ wafers is that the sample with the medium oxygen content has the highest carbon

concentration while the other two have a similar amount of carbon content which is lower than in the medium oxygen sample.

A summary of the implantation conditions and the oxygen/carbon concentrations are given in Table 4.5. Due to the complication caused by carbon as a second variable in the medium oxygen (MeO) sample we will concentrate our results on the other two CZ samples. The carbon content of FZ sample is not available.

Wafer Identifier	Substrate doping (cm^{-3})	Oxygen content (cm^{-3})	Carbon content (cm^{-3})	$^{74}Ge^+$ dose (cm^{-2})	$^{74}Ge^+$ energy (keV)	$^{74}Ge^+$ dose (cm^{-2})	Ge^+ energy (keV)
HiO	$3.2x10^{15}$	$9.5x10^{17}$	Low	$1x10^{15}$	800	$1x10^{15}$	400
MeO	$2.3x10^{15}$	$8.5x10^{17}$	High	$1x10^{15}$	800	$1x10^{15}$	400
LoO	$2.3x10^{15}$	$7.5x10^{17}$	Low	$1x10^{15}$	800	$1x10^{15}$	400
FZ	$6 x10^{14}$	Ref.	----	$1x10^{15}$	800	$1x10^{15}$	400

Table 4.5 Implantation conditions and the concentrations of oxygen and carbon in samples studied in section 4.3.

The wafers were implanted at room temperature. The beam current density was kept at 0.046 $\mu A\ cm^{-2}$ to avoid heating. Cross sectional TEM (XTEM) on un-annealed samples showed the wafers were fully amorphized after ion implantation. A standard Si cleaning as detailed in section 4.2 was carried out before solid phase epitaxial regrowth in a rapid thermal annealer in 100% nitrogen for 20 seconds. This provided an atmosphere in which oxide growth did not occur at the surface. The significance of this is discussed in section 4.3.3.1. The maximum temperature during RTA was 970°C. Each wafer was then cleaved

into 3 samples for structural, optical and electrical measurements. Titanium Shottky Barriers and Aluminum Ohmic contacts were made for the electrical measurements.

Cross sectional (XTEM) and plan view transmission electron microscopy (PTEM) were carried out using a Phillips CM12 microscope operating at 120 kV. Bright-field (BF) micrographs were recorded with the sample tilted to a [110] pole for the cross sectional samples and the [001] pole for the plan view samples. In addition, bright field micrographs were recorded with the samples tilted to g (220) two beam diffraction condition for cross sectional samples.

Ge concentration profiles and atomic lattice location were checked using 1.5 MeV He^+ Rutherford backscattering spectrometry (RBS) and channelling analysis. The overall energy resolution of the RBS system was better than 13 keV and the scattering angle was 160°.

Photoluminescence (PL) measurements were carried out at 8.5 K using excitation by the 514 nm line of an Ar^+ laser at 50 mW.

Room temperature C-V measurements were carried out at 1MHz. A Bio-Rad DL4600 system was used for the DLTS measurements.

4.3.2 Results

4.3.2.1 TEM Results

Figure 4.9 are XTEM and PTEM micrographs for high oxygen (HiO) and low oxygen (LoO) samples. Figure 4.9 (a) and (b) are XTEM micrographs showing the EOR dislocation loops and the threading dislocations in HiO and LoO samples respectively. The dislocation loops observed in both samples were located just below the original α/c interface at a depth of approximately 0.75 μm from the sample surface. The mean average dislocation loop diameter of the HiO and LoO sample was 33 nm and 40 nm respectively. The mean area densities of them were 2.6 x 10^{10} cm^{-2} [1] and 1.3 x 10^{10} cm^{-2}. Threading dislocations were present in the upper part of the regrown layers in both samples. None of them extended down to the loops, the depth of the threading dislocations ranged from 400 nm to 600 nm. Figure 4.9 (c) and (d) are the PTEM micrographs showing the threading dislocations in HiO and LoO samples respectively. The area density of them were 1.2x10^9 cm^{-2} and 4x10^8 cm^{-2} for HiO and LoO samples respectively. Table 4.6 summaries the TEM results.

Sample Identifier	Mean dislocation loop diameter (nm)	Area density of dislocation loops (cm^{-2})	Area density of hairpin dislocations (cm^{-2})
HiO	33	2.6 x 10^{10}	1.2 x 10^9
LoO	40	1.3 x 10^{10}	4 x 10^8

Table 4.7 Summary of TEM results

[1] values from similar samples

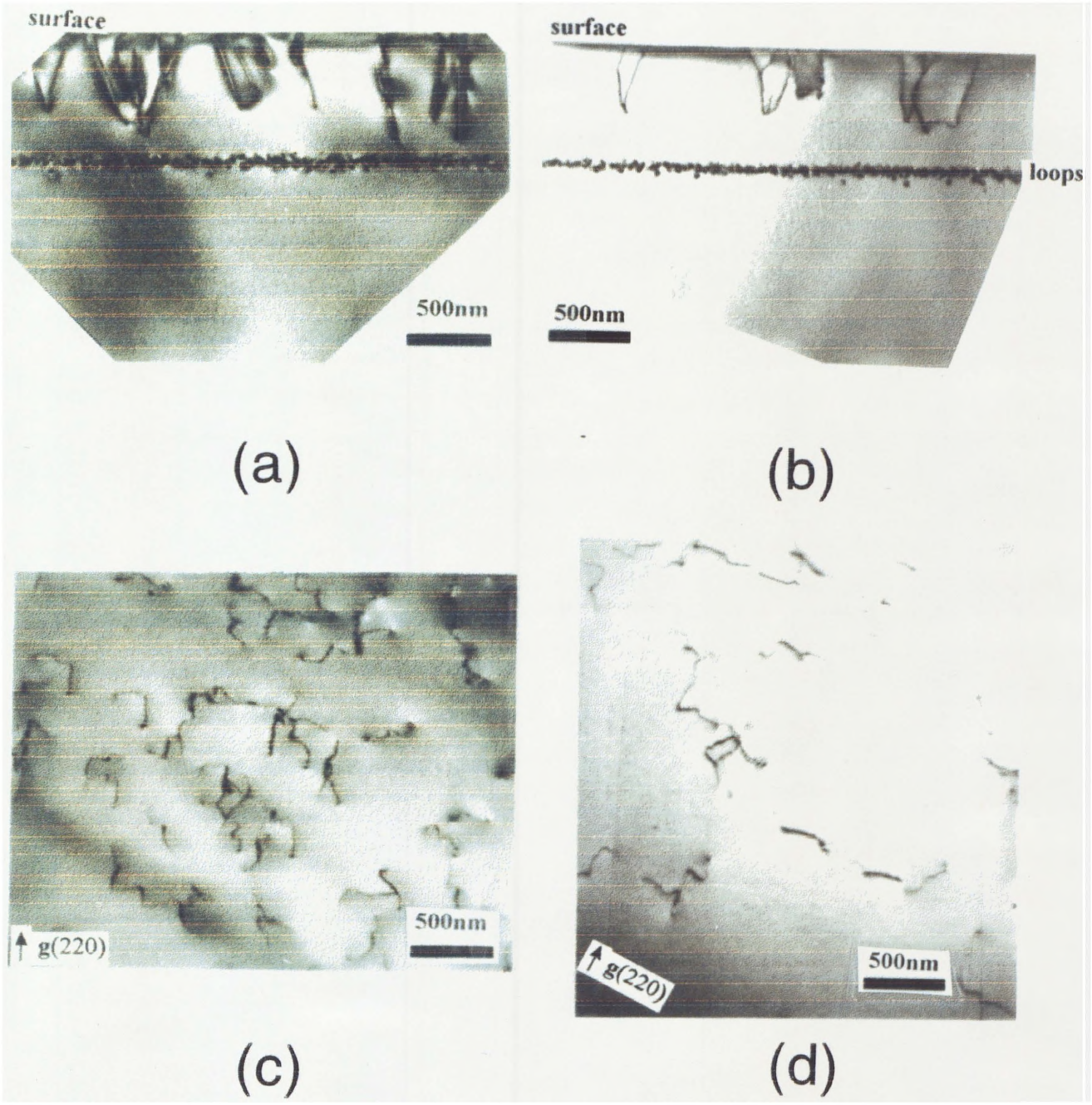

Figure 4.9 (a) and (b) are XTEM micrographs showing the EOR dislocation loops and the threading dislocations in HiO and LoO samples respectively (c) and (d) are the PTEM micrographs showing the threading dislocations in HiO and LoO samples respectively

4.3.2.2 PL Results

Photoluminescence results are plotted in Figure 4.10 (a) and (b) for HiO and LoO samples respectively. The 0.81 eV and 0.87 eV broadband lines were clearly seen in both samples. Other lines at energies 0.919 eV, 1.034 eV, 1.093 eV, 1.098 eV were also observed. The ratio of the integrated area under the 0.81 eV (D1) and 0.87 eV (D2) lines to the integrated area under the 1.093 eV (transverse optical phonon sideband of boron bound exciton B_{TO}, refer to chapter 3, section 3.2.1) and 1.098 eV (TO phonon sideband of free-exciton luminescence FE(TO), refer to chapter 3, section 3.2.1) peaks was used as a means to obtain the relative total number per unit area of D1/D2 related radiative defects in the two samples (the concept is similar to the ratio technique described in chapter 3, section 3.2.1), the results being 20.4 for the HiO sample and 7.5 for the LoO sample.

4.3.2.3 C-V and DLTS Results

Apparent free carrier concentration profiles derived from room temperature capacitance-voltage (C-V) measurements of HiO and LoO samples are shown in Figure 4.11 (a). In both samples excess acceptors, clearly above the substrate doping level were observed. This was based on the assumption that distractions from various sources such as the surface states of the Schottky diodes had not caused serious artifacts in these measurements. The concentrations of the excess acceptors (maximum value of apparent acceptor doping concentration minus the substrate doping concentration) in the HiO and LoO samples were

3.36×10^{14} cm^{-3} and 1.06×10^{14} cm^{-3} respectively. As will be discussed later, the results shown in Figure 4.11 (a) needs to be treated with care with respect to the precise interpretation of the concentration and location of the acceptors when deep levels are present.

Further investigation of deep defect levels beyond the α/c boundary was carried out by DLTS measurements. The thermal emission characteristics of the peak observed in both samples suggested they originated from the same deep level state. The hole emission activation energy of the deep trap increased from 0.44 eV to 0.51 eV as we increased the reverse and forward bias together (keeping the difference between them the same e.g. from reverse bias V_r= - 0.5 V and forward bias V_f= 0 V to V_r= - 1 V and V_f= - 0.5 V). As an example, Figure 4.11 (b) shows the DLTS spectrum from the LoO sample at two rate windows: 400/s and 200/s.

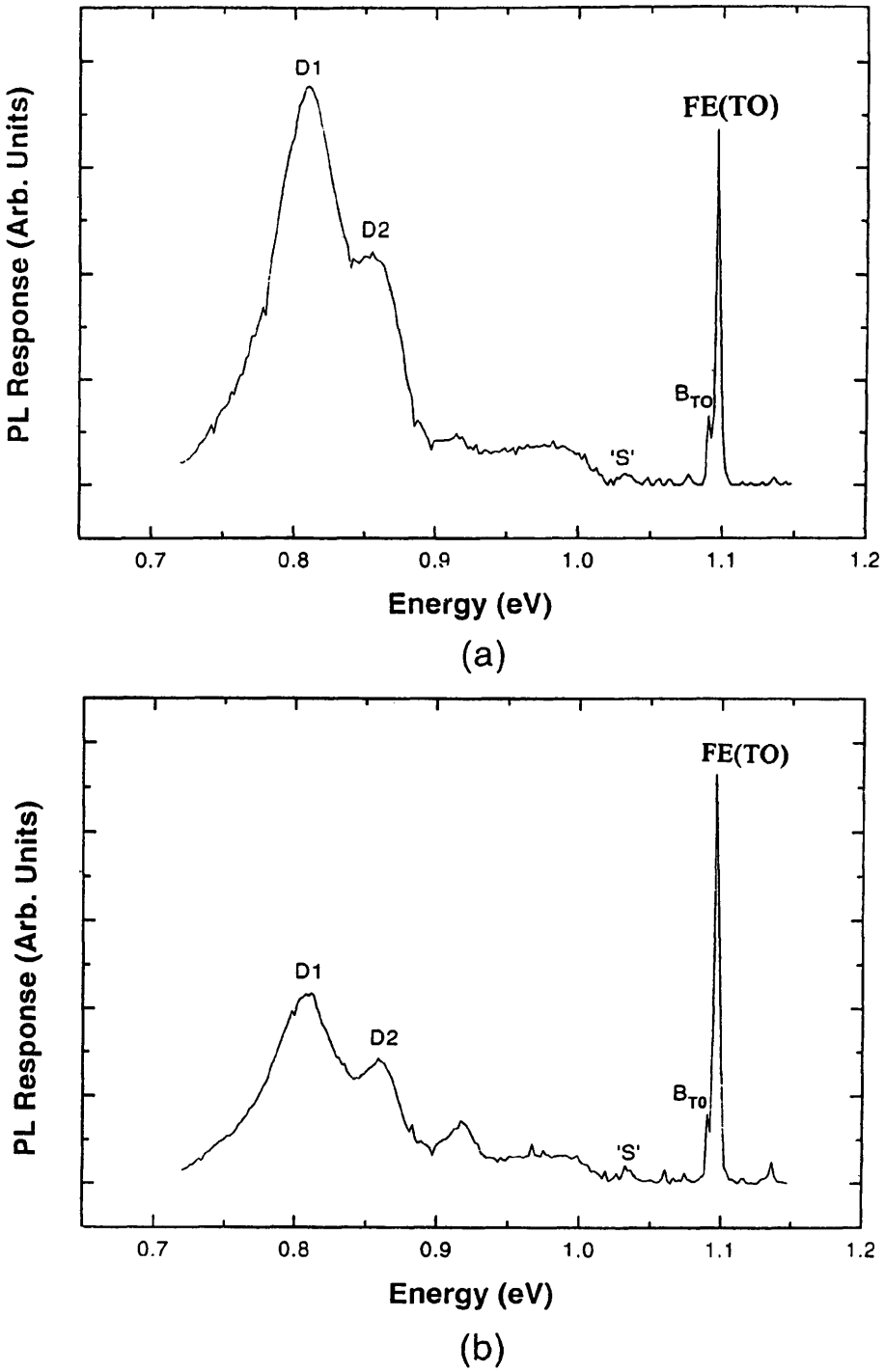

Figure 4.10 (a) and (b) are photoluminescence results for HiO and LoO samples respectively. B_{TO} is the transverse optical phonon sideband of the boron bound exciton luminescence. FE(TO) peak is the TO phonon sideband of free-exciton luminescence.

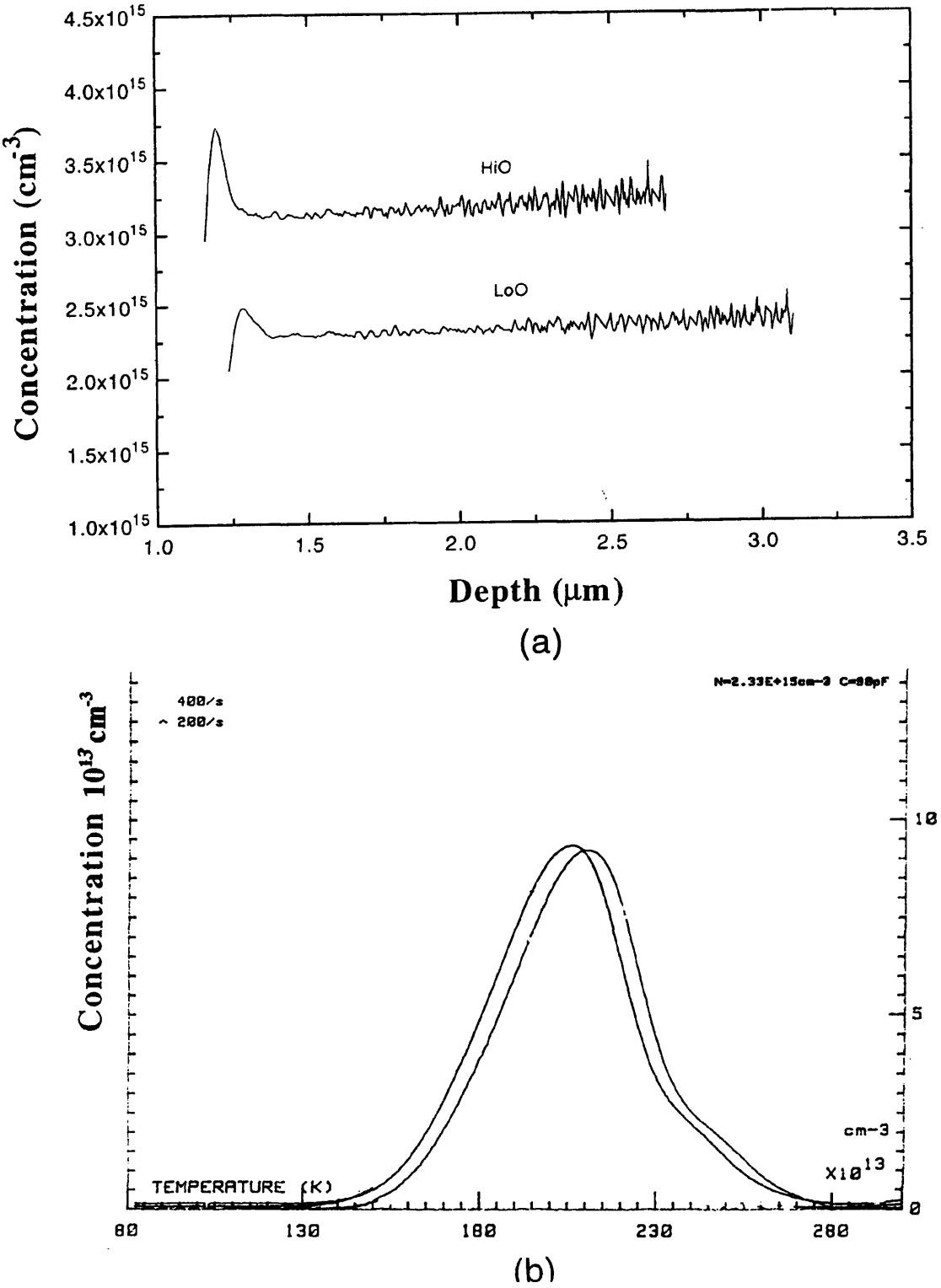

Figure 4.11 (a) apparent free carrier concentration profiles derived from room temperature capacitance voltage (C-V) measurements of HiO and LoO samples (b) DLTS spectrum from LoO sample at two rate windows: 400/s and 200/s.

4.3.3 Discussions

4.3.3.1 Defects Structure and Distribution by TEM Observations

The point defects present immediately after ion implantation are believed to be predominantly self-interstitials. In particular the EOR region becomes highly supersaturated with self-interstitials during implantation. The evolution from the supersaturation of point defects to the EOR dislocation loops is believed via the intermediate defect configurations (IDC) proposed by Tan [Tan 81].

The removal of the EOR defects was studied by Seidel et al [Seidel 85] using isothermal annealing experiments and observing the evolution of defects by TEM technique. The annealing rate was found to have ~ 5 eV activation energy, indicating that the self-diffusion of silicon atoms was a rate determining factor in the annealing process. The removal of the EOR defects was found to be greatly affected by the presence of sinks and sources for the self-interstitials. For example Ajmera [Ajmera 86] reported the removal, in a nonoxidizing Ar ambient, of the shallow EOR defects located near the sample surface whereas the deeper EOR defects still remained. This was because the free surface could be considered as a infinite sink for the self-interstitials. It was also reported that the annealing of the EOR defects was enhanced when the concentration of implanted species exceeded the solid-solubility limits, so that at a later stage the dissolution of the precipitates could provide vacancies (self-interstitial sinks) for the enhanced elimination of the dislocation loops.

An oxidizing annealing ambient was found to inject silicon self-interstitials into the material from the oxidizing interface and impeded the annealing out of the EOR defects. Silicon self-interstitials can also be produced by heating oxygen rich CZ silicon when oxygen atoms start to precipitate. Precipitation of other impurities such as copper and palladium will form metal-rich silicide particles causing a supersaturation of Si self-interstitial as well [Seibt 88].

Narayan et al [Narayan 72] developed a model suggesting that the coarsening of dislocation loops occurred primarily by dislocation glide and conservative climb processes. TEM work on similar wafers to those used in this study [Meekison 89][Meekison 91] showed that after the formation of such dislocation loops they then increased in size and decreased in number by diffusion between loops and subsequently decreased in size before being eliminated by diffusion to the wafer surface.

The fact that our TEM results revealed that the low oxygen sample had a bigger mean loop diameter with a lower mean loop density implied that the coarsening of dislocation loops in this sample was more favored than in the high oxygen sample. In other words it would be more difficult to remove the EOR defects in the high oxygen sample because the oxygen "hardened" the material and making glide and climb process less favored.

In this work the geometry observed by TEM of the threading dislocations in the upper part of the layer might suggest that as the α/c interface moved towards the wafer surface during annealing, it encountered local inhomogeneities (nucleation centers), and this generated

dislocations which extended to the wafer surface with the advancing interface. A possible source for these inhomogeneities may result from the implanting Ge^+ beam, e.g. contaminating ions within the beam, or contaminating atoms initially on the wafer surface which were knocked into the wafer by the beam (the depth of the threading dislocations corresponded to the amorphized layer thickness produced by the second 400 keV Ge^+ implant which might have added to the effect due to the first 800 keV Ge^+ implant).

It has been reported that high temperature annealing of oxygen rich CZ Si caused the out-diffusion of oxygen atoms towards the sample surface and during this process, oxygen atoms may interact with impurities generated by ion implantation. Therefore the increased nucleation centers may be responsible for the higher area density of threading dislocations in the high oxygen sample in this work.

Actually oxygen might not be the only influence on the behavior of extended defects. Due to the second variable: the carbon concentration, in addition to the oxygen concentration in the medium oxygen sample (MeO), we have observed rod-like defects in the MeO sample (not in the other two samples). Further investigation is needed in this respect.

4.3.3.2 PL Analysis on Defect Related D-lines

Photoluminescence spectra from dislocated silicon exhibit a number of characteristic lines termed D1 to D6 [Drozdov 76][Sauer 85]. Most studies have been carried out on plastically

deformed silicon. However, it has been reported that D1 and D2 lines can be observed in heat-treated Czchralski grown silicon [Tajima 83].

The 0.81 eV and 0.87 eV lines in this work were at the energies of the dislocation related D1 and D2 lines. In addition, judging from the features of the spectra, the other reported D lines (D3, D4, D5, D6, D12), may well exist in this work. The small broad peak at 0.919 eV had the same energy as the reported radiation damage center involving carbon [Davies 84]. The 1.034 eV line in this work can be related to one of the 'S' series in heat treated CZ silicon [Davies 89]. The peak at 1.093 eV in this work is the transverse optical (TO) phonon sideband of the boron bound exciton luminescence B_{TO}. The peak at 1.098 eV in this work is the transverse optical phonon sideband of the free-exciton luminescence FE(TO).

D-lines from ion-implanted silicon were reported by Uebbing [Uebbing 80] where D1 was the main feature of the PL spectra and the TEM showed slip dislocations. Shreter [Shreter 93] reported ion-implanted silicon with D2 line dominating PL spectra and TEM of these samples showed EOR defects.

The influence of oxygen on D-lines was studied with controversial results. Suezawa et al [Suezawa 83] reported that D1 does not vary between float-zone and CZ silicon heated at 900°C. In contrast, Osip'yan [Osip'yan 82] investigated D-line PL spectra in two plastically deformed and annealed CZ samples with different oxygen content. He found that the behavior of D1 line depended on the initial content of the oxygen in the crystal.

The D-line luminescence have been proposed as being associated with dislocations introduced by plastic deformation. Two models have emerged regarding the origin of the PL features observed from dislocated silicon. One is the radiative electronic transition involving capture into a strain field potential associated with the dislocation and the other involves excitonic collapse onto impurities residing at dislocations and possibly interacting with point defect clusters present in dislocated samples ('impurity model') [Kimerling 79]. An important observation which supports the 'impurity model' is the absence of the D-line luminescence in plastically deformed silicon without a deliberate contamination with copper [Higgs 90].

In our CZ silicon where the dissolved oxygen concentration was above the solid solubility limit, excess oxygen atoms may rapidly redistribute through the annealing process. They then precipitated and interacted with dislocations [Sumino 87] and other impurities. According to the 'impurity model' described previously this enhanced interaction between dislocations, EOR defects and threading dislocations, and impurities, (from transition metal related defects or from excess oxygen atom related defects), was suggested to be responsible for the larger D-line signal observed in the high oxygen sample.

The concept that oxygen is an essential influence on the D1 and D2 lines in our samples is supported by two additional observations:

1) missing D1/D2 lines in the FZ sample. Instead a broad band centered at about 0.97 eV dominated the PL spectrum in addition to the B_{TO} and FE(TO) luminescence. The 0.97 eV line had the same energy as the "G" line which involved

two carbon atoms and one silicon atom [Woolley 87].

2) although the carbon content in the MeO (medium oxygen) sample was higher than the HiO and LoO samples, the ratio of the integrated area under the D1 and D2 lines to the integrated area under the B_{TO} and FE(TO) peaks was smaller than that of HiO sample and bigger than that of LoO sample.

4.3.3.3 C-V and DLTS Characterization of Excess Acceptors and the Associated Deep Hole Traps

It has already been mentioned that the apparent free carrier profiles derived from high frequency C-V measurements needed to be treated with care with respect to the precise interpretation of the concentration and location of the acceptors when deep levels are present. We will consider acceptor-type deep levels in p-type material and their contribution to the excess hole concentration in the C-V profiles. According to the equation [Kimerling 74] shown below (assuming an inhomogeneous triangle shape distribution of the deep level) the measured location of the maximum acceptor concentration would be ~ λ deeper than the actual location. There would be a reduction in the measured excess acceptor concentrations as well , the lower the substrate doping the more the reduction [Brotherton 89].

$$\lambda = \sqrt{\frac{2\varepsilon(E_T - E_F - kT)}{qN_A}} \tag{4.4}$$

where N_A is the shallow acceptor concentration, E_T is the energy level of the deep defect and E_F is the Fermi level. When applied to the observed hole trap with an activation energy for hole emission of 450 meV, the actual location of the maximum point of excess acceptor concentration was at 1.3μm - 0.33μm (λ) = 0.97 μm, which was 0.22 μm beyond the actual α/c boundary in this work. This is in consistent with previous work [Brotherton 89] where it was found that all the deep levels revealed from DLTS measurements were about 0.2μm-0.3μm deeper than the α/c boundary (figure 6 in reference [Brotherton 89]). He related these defects to the interstitial silicon excess in the region beyond the α/c boundary.

The anomalous phenomena from the C-V profiles that a one to one correspondence was lacked (donor levels in p-type materials as in section 4.3 and acceptor levels in n-type materials as in section 4.2) could be caused by many distractions such as: the two types of materials are not grown with the same method, the ion implantation conditions are different, the annealing conditions are different, etc.

Deep states with similar thermal emission characteristics from published data were compared with our DLTS results. Our 450 meV hole trap was found to have similar emission characteristics to a deep level reported by Barbier [Barbier 87] in p-type rapid thermal annealed silicon with a hole emission activation energy of 450 meV, there it was

associated with interstitial iron. Other reported metallic impurities such as cobalt [Evwaraye 78], copper [Brotherton 87] also had a thermal emission characteristics similar to our hole trap.

In addition an acceptor type deep level with hole emission activation energy of 520 meV has been reported by Ono [Ono 85] in p-type silicon. This was induced by plastic deformation. According to Ono this defect was associated with agglomerations of point defects that resulted from dislocation debris.

The width of our hole trap peak was larger than that due to a single deep trap (a shoulder on the side of the peak can also be seen), indicating it was probable that several kinds of traps contributed to give rise to this broad peak.

Iron and other transition-metal impurities have been reported as being present in the form of precipitates in as grown materials [Barbier 87]. If this was the case in our samples the heating stage of our RTA would have resulted in the dissolution of the precipitates and the diffusion of the transition metals. A subsequent quenching during the fast cooling-down stage would leave a significant concentration of positively charged interstitial atoms which could be captured by negative substitutional shallow acceptors in p-type silicon. Then at lower temperature these pairs would dissociate and formed other complexes. In general 3d-metal impurities diffuse via interstitial sites [Weber 83]. As there are considerable concentrations of excess self-interstitials beyond the α/c boundary due to the recoil implantation of displaced host atoms [Thornton 88][Brotherton 89], it is probable that our

hole trap is related to agglomerations of point defects that were associated with more than one type of 3d-metal related defects accumulated beyond the α/c boundary.

4.3.4 Conclusions

Czochralski (CZ) grown p-type silicon samples with different oxygen concentrations have been implanted with Ge^+ and subsequently rapid thermal annealed in nitrogen. The effect of oxygen concentration in the starting material on residual defects has been studied by TEM, PL, C-V and DLTS techniques.

A photoluminescence study showed a strong correlation between the D-line (D1 and D2) intensity and the initial oxygen content in the material. We observed a larger D-line signal in the sample with the high oxygen content.

TEM results suggested that the formation of extended defects was not only influenced by the oxygen content but also by the carbon content. In the case where the carbon content was the same the extended defects were present in higher concentration in the high oxygen sample.

High frequency room temperature C-V profiles revealed excess acceptor levels which may relate to deep hole traps measured by DLTS at the region beyond the α/c boundary. The hole traps are suggested to be the agglomerations of point defects associated with more

than one type of 3d-metal related defects. They accumulate beyond the α/c boundary region via the enhanced diffusion mechanism due to the recoil implanted excess self-interstitials.

References

[Ajmera 86] Ajmera A. C. and Rozgonyi G. A., *Appl. Phys. Lett., 49*, 1986, pp 19

[ASTM 85] 1985 Annual Book of ASTM Standards (Philadelphia, PA: ASTM) pp 242

[Ayres 87] Ayres J. R., Brotherton S. D., Clegg J. B. and Gill A., *J. Appl. Phys., 62*, 1987, pp 3628

[Barbier 87] Barbier D., Remram M., Joly J. F. and Laugier A., J. *Appl. Phys., 61 (1)*, 1987, pp 156

[Brotherton 87] Brotherton S. D., Ayres J. R., Gill A., van Kersteren H. W. and Greidanus F. J., *J. Appl. Phys., 62*, 1987, pp 1826

[Brotherton 89] Brotherton S. D., Ayres J. R., Clegg J. B. and Gowers G. P., *J. Electron Mater., 18*, 1989, pp 173

[Bürger 84] Bürger N., Thonke K., Sauer R and Pensl G., *Phys. Rev. Lett., 52(18)*, 1984, pp 1645

[Chappell 88] Chappell S. P., Claybourn M., Newman R. C. and Barraclough K. G., *Semicond. Sci. & Technol., 3*, 1988, pp 1047

[Davies 84] Davies G., Lightowlers E. C., Woolley R. A., Newman R. C. and Oates A. S., *J. Phys. C17*,1984, pp L499

[Davies 88] Davies G., Lightowlers E. C., Thomas M. F. and Wilkes J. G., *Semicond. Sci. Technol., 3*, 1988, pp 608

[Davies 89] Davies G., *Phys. Rep., 176*, 1989, pp 83

[Drozdov 76] Drozdov N. A., Patrin A. A. and Tkachev V. D., *Sov. Phys. JETP Lett. 23*, 1976, pp 597

[Evans 92] Evans J. H., Kaniewski J. and Kaniewska M., *Semicon. Sci. & Tech. 7(1A)*, 1992, pp A41

[Evwaraye 78] Evwaraye A. O., *J. Electron. Mater., 7*, 1978, pp 383

[Ferreira 76] Ferreira C. A. and Howie A., *Phil. Mag., 34*, 1976, pp 1057

Distribution Theory and Experiment", *Proc., IEEE, 56*, 1968, pp 295

[Higgs 90] Higgs V., Lightowlers E. C. and Kightley P., in Impurities, Defects and Diffusion in Semiconductors: Bulk and Layered Structures, edited by Wolford D. J., Bernholc J. and Haller E. E. (Materials Research Society, Pittsburgh, PA, 1990), pp 57

[Jones 88] Jones K. S., Prussin S. and Weber E. R., *Appl. Phys. A., 45*, 1988, pp 1

[Kern 70] Kern W. and Puotinen, *RCA Rev. 31*, 1970, pp187

[Kimerling 74] Kimerling L. C., *J. Appl. Phys., 45 (4)*, 1974, pp 1839

[Kimerling 79] Kimerling L. C. and Patel J. R., *Appl. Phys. Lett., 34*, 1979, pp 73

[Kirkpatrick 76] Kirkpatrick C. G. and Noonan J. R., *Rad. Effects, 30*, 1976, pp 97

[Kveder 82] Kveder V. V., Osipyan Yu. A., Schröter W. and Zoth G., *Phys. Stat. Sol. (a), 72*, 1982, pp 701

[Lambert 81] Lambert J. A. and Dobson P. S., *Phil. Mag., 44*, 1981, pp 1043

[Lorenz 91] Lorenz E., Gyulai J. Frey L., Ryssel H., J. and Khanh N. Q., *Mater. Res., Vol. 6*, No. 8,1991, pp 1695

[Maher 86] Maher D. M., Knoell R. V., Ellington M. B. and Jacobson D. C., *Mat. Res. Soc. Symp. Proc. 52*,1986, pp 93

[Meekison 89] Meekison C. D., Gold D. P., Booker G. R., Hill C. and Boys D. R. *Micros. Semicond. Mater. Conf., Oxford, Inst. Phys. Conf. Ser. No. 100*, 1989, pp 507

[Melvin 60] Melvin L., *Phys. Rev., 119(5)*, 1960, pp 1502

[Myers 86] Myers E., Rozgonyi G. A., Sadana D. K., Maszara W., Wortman J. J. and Narayan J., I. *Mat. Res. Soc. Proc., 52*, 1986, pp 108

[Narayan 72] Narayan J. and Washburn J., *Philos. Mag. 26*, 1972, pp 1179

[Nakayama 81] Nakayama H., Nishino and Hamakawa Y., *Appl. Phys. Lett., 38*, 1981, pp 623

[Omling 85] Omling P., Weber E. R., Montelious L. and Alexander H. M., *Phys. Rev. B, vol. 32*, 1985, pp 6571

[Ono 85] Ono H. and Sumino K., *J. Appl. Phys. 57 (2)*, 1985, pp 87

[Osip'yan 82] Osip'yan Y. A., Rtishchev A. M., Shteinman E. A., Yakimov E. B., Yarykin N. A., Ah. Eksp. *Teor. Fiz. 82*, 1982, pp 509; *Sov. Phys. JETP 55*, 1982, pp 294

[Salisbury 81] Salisbury I. G., *Acta metall., Vol. 30*, 1982, pp 627

[Sauer 85] Sauer R., Weber J., Stolz J., Weber E. R., Kusters K. H. and Alexander H., *Appl. Phys., A 36*, 1985, pp 1

[Seibt 88] Seibt M., Graff K., *J. Appl. Phys. 63(9)*,1988, pp 4444

[Seibt 92] Seibt M., Imschweiler J. and Hefiner H. A., *Mat. Res. Soc. Symp. Proc. Vol. 262*, 1992

[Seidel 85] Seidel T. E., Lischner D. J., Pai C. S., Knoell R. V., Maher D. M. and Jacobson D. C., *Nucl. Inst. Meth. Phys. Res. B, 7/8*, 1985, pp 251

[Servidori 87] Servidori M., Angelucci R., Cembali F., Negrini P., Solmi S., Zaumsei P. and Winter U., *J. Appl. Phys., 61*, 1987, pp 1834

[Shreter 93] Shreter Yu., Evans J. H., Hamilton B., Peaker A. R., Hill C., Boys. D. R., Meekison C. D. and Booker G. R., *Appl. Surf. Sci., 63*, 1993, pp 227

[Suezawa 83] Suezawa M. and Sumino K., *Phys. stat. sol. (a) 78*, 1983, pp 639

[Sumino 87] Sumino K., in Defects and Properties of Semiconductors: Defect Engineering, edited by Chikawa J., Sumino K. and Wada K. (KTK Scientific Publishers, Tokyo, 1987), pp 227

[Sze 85] Sze S. M., *Semiconductor Devices, Physics and Technology*, 1985, John Wiley & Sons

[Tajima 81] Tajima M., in *Neutron Transmutation Doped Silicon*, edited Guldberg J. (Plenum, New York), 1981

[Tajima 83] Tajima M. and Matsushita Y., *Jpn. J. Appl. Phys. 23*, 1983, pp L589

[Tan 81] Tan T. Y., *Philos. Mag., 44*, 1981, pp 101

[Thornton 88] Thornton J., Webb R. P., Wilson I. H. and Paus K. C., *Semicond. Sci. Technol. 3*, 1988, pp 281

[Uebbing 80] Uebbing R. H., Wagner P., Buamgart H. and Quiesser H. *J., Appl. Phys. Lett., 37*, 1980, pp 1078

[Wang 76] Wang K. L. and Evwaraye A. O., *J. Appl. Phys., 47*, 1976, pp 4547

[Weber 83] Weber E. R. and Wiehl N., *Defects in Semiconductors II*, Mater. Res. Soc. Proc. (North-Holland, New York, 1983), 14, pp 19

[Woolley 87] Woolley R. A., Lightowlers E. C., Tipping A. K., Claybourn M. and Newman R. C., *Mater. Sci. Forum 10-12*, 1987, pp 929

[Zhang 93] Zhang J. P., Fan T. W., Gwilliam R. M., Hemment P. L. F., Wen J. Q., Qian Y., Efeoglu H., Evans J. H. and Peaker A. R., *Nucl. Instru. Meth. in Phys. Res. B74, Iss:1-2*, 1993, pp 127

[Ziegler 85] Ziegler J. F., Biersack J. P. and Littmark D. V., *The Stopping and Ranges of ion in Solids, Vol. 1*, Ed: Zeigler J. F. (Pergamon Press, New York, 1985)

Chapter 5 Characterization of $Si_{1-x}Ge_x/Si_{1-x-y}Ge_xC_y$ Alloys Formed by Implantation

5.1 Introduction

SiGe alloys have smaller fundamental bandgaps than Si that decreases with increasing Ge content [Braunstein 58] and are further reduced when the $Si_{1-x}Ge_x$ alloy is tetragonally strained [Baslev 66]. This system therefore has potential for devices that rely for their operation on some degree of bandgap engineering. In recent years, there has been considerable interest in such devices as high performance heterojunction bipolar transistors (HBT) [Patton 88], high speed modulation doped field effect transistors [Temkin 86], resonant tunnelling diodes [Rhee 88] and $Si/Si_{1-x}Ge_x$ strained superlattices (SLS) [Presting 92]. Fabrication of these devices could, in principle, be integrated with Si-based waveguide and device technology to provide optoelectronic functionality. However high quality $Si_{1-x}Ge_x$ layers are normally grown by epitaxial techniques such as Molecular Beam Epitaxy (MBE) [Kasper 88], low pressure chemical vapor deposition (LPCVD) [Meyerson 88] or Chemical Beam Epitaxy [Kramer 92] techniques. They are not easily integrated into conventional silicon processing at the present time.

In contrast, ion implantation is highly compatible with modern silicon processing and has been shown to be suitable for fabricating SiGe alloys [Hart 81][Paine 90] using suitable implantation and regrowth conditions; bandgap engineering can be achieved by

adjusting the implant conditions. Since the interface between the substrate and the SiGe layer is graded and the composition change in the SiGe layer itself is gradual, the strain relaxation mechanism in the ion-implantation layer is somewhat different from that in epitaxial grown layers and may result in a reduction of threading dislocations. It has been demonstrated that by grading the Ge content in the SiGe alloy (grown by MBE [LeGoues 91]), very high quality layers can be obtained that have low dislocation densities. In addition, for certain device applications a graded configuration is beneficial. For example, composition grading of the Ge content in the base region of a SiGe HBT will create a built-in field that reduces the base transit time

which enables higher frequency performance to be achieved [Chen 92].

However, ion implantation of high doses of Ge^+ and subsequent thermal annealing of the semiconductor alloy is liable to lead to the generation of defects. One type is a group of extended defects consisting of misfit dislocations and misfit induced stacking faults in the SiGe layer. They are introduced when the alloy layer exceeds the critical layer thickness and starts to relax. It has been reported that misfit dislocations and misfit-induced stacking faults from a high dose germanium implantation can not be completely eliminated for a certain germanium peak volume concentration (above 6% in Im's paper [Im 92]). However, a reduction in the density of these defects has been achieved by using carbon (C^+) co-implantation [Fukami 90]. The lattice constant in Ge is about 4% larger than in Si whereas in diamond it is 52% smaller. When on substitutional sites, carbon contracts the lattice and counteracts the strain introduced by the germanium, which expands the lattice. Therefore co-implant of carbon into SiGe system and locate it onto substitutional sites will compensate fully or partially the strain caused by the Ge. Another advantage of adding carbon is it can act as sink for the

excess Si self-interstitials [Liefting 92] therefore reducing the source for the formation of dislocations which relieve the strain. This method has been shown to produce a regrown material of a higher structural quality with improved electrical characteristics [Fukami 90].

Another characteristic defect in ion-implanted silicon is a plane of dislocation loops at or near the original amorphous/crystalline (α/c) interface, known as end of range (EOR) defects. If the EOR dislocation loops are in the vicinity of the active region of the device the associated electrically active deep states will result in high leakage currents or a reduction in minority carrier lifetime, and, as such, are a cause of device degradation [Brotherton 89]. When the EOR defects are in the vicinity of the SiGe alloy region, the presence of them may have influence on strain relaxation, dependent on how big the strain is. As has been reported [Berti 91] that a good quality, almost fully strained, SiGe layer was achieved when EOR defects were eliminated using eximer laser irradiation. But under the same condition except that when the laser power was not high enough to anneal out the EOR defects, the alloy layer was partially relaxed. Reduction and even annihilation of the EOR defects in SiGe alloys are reported by lowering the substrate temperature during germanium [Jones 91] or carbon co-implantation [Lombardo 93]. Alternatively, the EOR defects can be moved away from the SiGe alloy region into deeper substrate region [Paine 90] [Zhang 94].

In this chapter structural characterization of SiGe alloys formed by Ge^+ implantation combined with prior C^+ implantation or Si^+ post amorphisation were carried out. Alloy layer relaxation mechanism from different strain and defects distribution are discussed. The depth profiles of the strain in the layers were determined by comparing the

experiment X-ray rocking curves with simulated data based on the dynamical theory of diffraction applied to the substitutional Ge and C implant profiles obtained by RBS or SIMS measurements. Defects distribution and structure quality was assessed by TEM technique.

5.2 Brief Literature Review on SiGe Alloys

5.2.1 SiGe Alloys

Germanium is immediately below silicon in column IV of the periodic table. The two elements have the same valence structure (four tetragonal sp^3 hybrids), the same crystal structure (diamond fcc) and similar indirect energy bandgaps. They are chemically compatible and that they can be freely mixed to form crystalline alloys of all compositions with no tendency to segregate into regions of differing structure or compositions. But there is a 4.17% lattice mismatch between them at room temperature which slightly increases when the temperature is increased. Because of the lattice mismatch, two types of epitaxial growth are possible on a bulk silicon substrate: pseudomorphic, or strained; and relaxed, or dislocated. First, as indicated in Figure 5.1 bottom right, because crystalline lattices have a certain elasticity, sufficiently thin epitaxial SiGe layers can distort to match the bonding arrangement of the Si substrate. The more widely spaced epitaxial alloy crystal compresses along the interfacial plane where the strain due to the lattice mismatch is accommodated. In the second situation the fourfold bonding cannot be maintained along the interface, and an occasional atom

is left with only three bonds. Rows of these improperly bonded atoms form so-called misfit dislocations and hence the material is relaxed. This situation is illustrated at top right of Figure 5.1

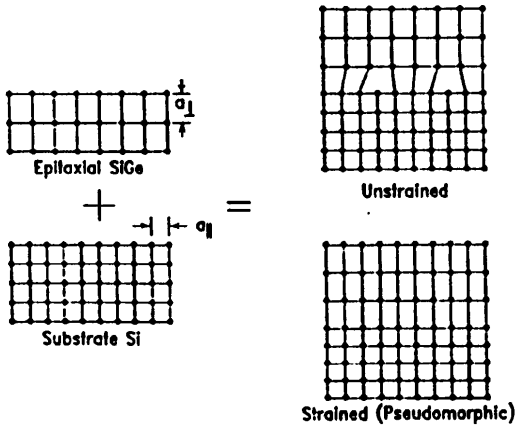

Figure 5.1 Two-dimensional representation of unstrained and pseudomorphic SiGe alloy layers grown on Si substrate.

The interest in pseudomorphic growth is not only due to the lack of interfacial dislocations which could give rise to interface states, band discontinuities, and undesirable electrical activities, but also to the fact that the presence of tetragonal strain in the alloy produces a further reduction in the bandgap, with respect to the bulk alloy layer. Figure 5.2 shows the energy gap value as a function of Ge content. The upper curve are calculated for unstrained material and the lower curve for strained alloy layer on silicon substrates.

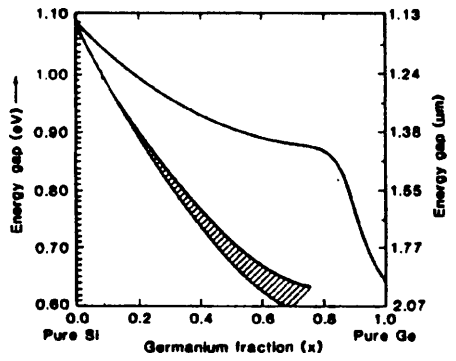

Figure 5.2 Energy bandgap for $Si_{1-x}Ge_x$ alloys. Curves are calculated for unstrained material (upper) and strained layer epitaxy (lower) on silicon substrates

5.2.2 Critical Layer Thickness

In strained layer semiconductor epitaxial systems the critical thickness for coherent growth refers to the thickness above which the strain in the layer is reduced by plastic deformation through the formation of misfit dislocations at the layer-substrate interface. Two values of h are required to describe any practical system. The equilibrium critical thickness (h_e) refers to the thickness at which it is energetically favorable for misfit dislocations to propagate through the material [Matthews 74][van der Merve 63]. The metastable critical thickness (h_m) defines the point at which a significant amount of strain has been released [Dodson 87] [Fritz 87]. When a material lies between h_e and h_m it is metastable and strain relaxation is a kinetically limited process. Major factors that control the rate of relaxation include the temperature [Miles 88], the density of misfit dislocation nucleation centers [Dodson 87][Tuppen 89], the misfit glide and/or climb velocities, and the efficiency of dislocation multiplication processes [Dodson 87].

There exist many different models for the calculation of critical thickness concerning, for example, the energy barrier for the formation of different types of dislocations [Jain 93] (90°, 60°, or 30° dislocations); the different types of defect nucleation sources (homogeneous misfit dislocation source [People 85], heterogeneous sources [Perovic 89]); the interaction with each other among dislocations and dislocations with point defects [Hull 90]; and the defect propagation systems related to material structures [LeGoues 91].

5.3 Effects of C^+ Co-implantation and Si^+ Post-amorphisation on the Optical and Structural Characters of $Si_{1-x}Ge_x$ Alloys

5.3.1 Sample Information

Four Czochralski p-type (100) 10 Ω-cm Si wafers were implanted using the conditions listed in Table 5.1.

Wafer No.	Identifier	C^+ dose (cm^{-2})	C^+ energy (keV)	$^{74}Ge^+$ dose (cm^{-2})	$^{74}Ge^+$ energy (keV)	Si^+ dose (cm^{-2})	Si^+ energy (keV)
1	LoGe	----	----	$3x10^{16}$	400	----	----
2	HiGe	----	----	$9x10^{16}$	400	----	----
3	HiGe+C	$6x10^{15}$	110	$9x10^{16}$	400	----	----
4	HiGe+Si	----	----	$9x10^{16}$	400	$6x10^{15}$	500

Table 5.1 Ion-implantation conditions for samples studied in this chapter

An identifying acronym is also shown in Table 5.1, e.g. for wafer 3 "HiGe+C" means high dose Ge^+ implant plus a prior C^+ implant. ---- means none.

The ion beam energy of $^{74}Ge^+$ was chosen to form a layer of $Si_{1-x}Ge_x$ with the maximum Ge concentration located at a depth of 0.26 μm below the sample surface. Wafer 3 was implanted with carbon prior to the high dose Ge^+ implantation. Wafer 4 was amorphised with silicon implant at liquid nitrogen temperatures after the high dose Ge^+ implant. The C^+ ion energy was chosen so that the distribution of C and Ge coincided, and for the Si postamorphisation energy, to ensure that the amorphised layer penetrated deeper into the crystal than the $Si_{1-x}Ge_x$ alloy region. Except for the Si postamorphisation all the other wafers were implanted at room temperature and were inclined at an angle of 7° to the beam so as to reduce direct ion channelling. The beam current densities for the C^+, $Ge^+$and Si^+ implantation were approximately 0.06 μA cm^{-2}, 1 μA cm^{-2} and 0.15 μA cm^{-2} respectively. All wafers were fully amorphised with Ge^+ implants. Solid phase epitaxial regrowth was at 700°C in a tube furnace with a flowing 100% nitrogen gas ambient.

5.3.2 Experiment Details

Cross sectional transmission electron microscopy (***XTEM***) was carried out using a JOEL 200 transmission electron microscope to determine the microstructure quality and defects distributions in the implanted wafers.

The Ge concentration depth profiles and the atomic lattice location were determined

using 1.5 MeV He^+ Rutherford backscattering spectrometry (***RBS***) and channelling analysis. The overall energy resolution of the RBS system was better than 13 keV and the scattering angle was 160°. Lattice damage was assessed from (100) RBS channelling spectra as well.

Double crystal X-ray diffraction (***DCD***) was employed to monitor the quality and Ge/C composition distributions of the structures and determine the depth distributions of strain perpendicular to the surface in the alloy layers. The radiation source of the X-ray: Cu Kα beam, was conditioned with a Si (004) crystal and detected by a scintillation counter. The step size was 2 arcsec. A dynamical X-ray simulation program (RADS) based on the Takagi-Taupin equations was used to generate theoretical spectra which were fitted to the experimental data.

Secondary ion mass spectroscopy (***SIMS***) using a 15 keV O^+_2 primary ion beam was also employed to obtain the depth profiles of total Ge and C concentrations.

The average concentration of substitutional carbon in the implanted layer was measured using Bio-Rad STS-60A Fourier Transfer Infrared Spectrometer (***FTIR***).

5.3.3 Results

5.3.3.1 TEM Results on Structural Quality and Defects Distributions

Figure 5.3 (a), (b), (c) and (d) are XTEM micrographs taken from samples from wafers

1, 2, 3 and 4 respectively. The XTEM micrograph of wafer 1, LoGe, is shown in Figure 5.3 (a) which indicates that the regrowth of the amorphised layer is complete and no extended defects other than the EOR defects which is about 0.5 μm from the sample surface are detected.

Figure 5.3 (b) is taken from a sample from wafer 2, HiGe, which shows that there is a dislocated region between the original amorphous/crystalline (α/c) interface and the sample surface.

Figure 5.3 (c) is taken from a sample from wafer 3, HiGe+C, which shows that the only detectable defects are the EOR defects located at the original α/c boundary of the Ge implantation at approximately 0.5 μm from the sample surface.

Figure 5.3 (d) is taken from the sample from wafer 4, HiGe+Si. The defects observed consist of EOR defects at the position of the original α/c boundary resulting from the Si postamorphisation, which is about 1μm from the sample surface, and threading dislocations located between the sample surface and the Ge implant peak position.

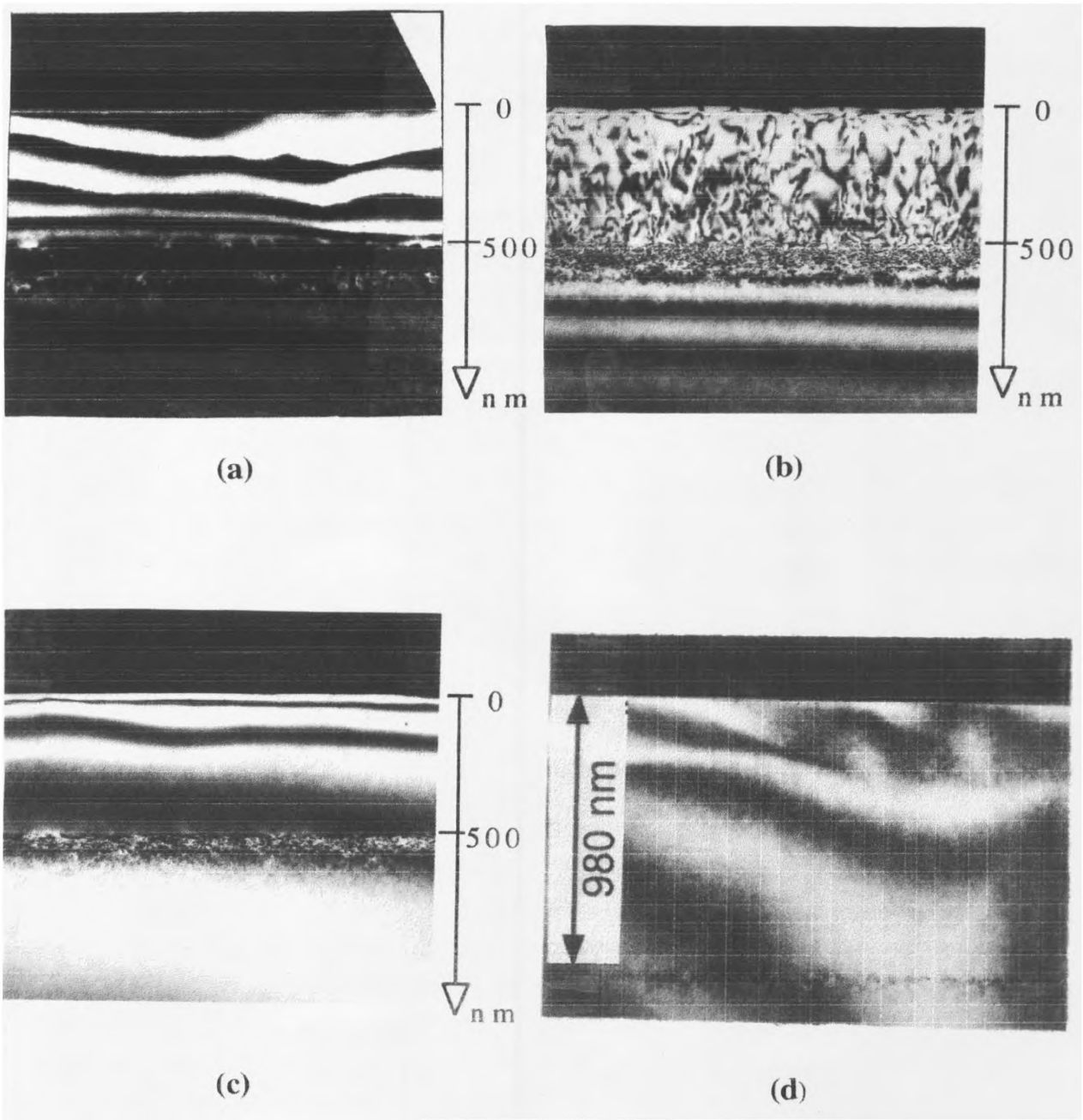

Figure 5.3 XTEM micrographs for:
(a)wafer 1 (LoGe), EOR defects at ~ 0.5 μm
(b)wafer 2 (HiGe), dislocations between EOR defects and sample surface
(c)wafer 3 (HiGe+C), EOR defects at ~ 0.5 μm
(d)wafer 4 (HiGe+Si), EOR defects at ~ 1 μm, and dislocations between sample surface and Ge peak position at ~ 0.26 μm

5.3.3.2 RBS and SIMS Results of Ge and C Distributions in SiGe Alloys

Figure 5.4 (a), (b), (c) and (d) are RBS spectra measured on samples from wafers 1, 2, 3 and 4 respectively. Curves A are the non-channelled spectra after annealing (the same for before annealing). Curves B and C are (100) channelled spectra from as implanted and after annealed samples respectively.

The Ge signals are located between channel numbers 300 and 395. The substitutional Ge concentration depth profiles were obtained by comparing curves A and C. In all wafers they follow a Gaussian profile, with the maxima located at a depth of approximately 0.26 μm from the sample surface.

The peak concentrations are found to be 8.7 at. % for wafers 2, 3 and 4, and 2.4 at. % for wafer 1. The total thickness of the $Si_{1-x}Ge_x$ alloy layer formed by the Ge^+ implantation is 0.5 μm.

SIMS measurements reveal that Ge distributions are consistent with RBS results. In the case of carbon implant the distribution of carbon overlaps with the Ge distribution and has a peak content of 0.68 at. %. A very thin layer of surface carbon is observed.

The Si postamorphisation process results in an amorphized layer of thickness 1 μm.

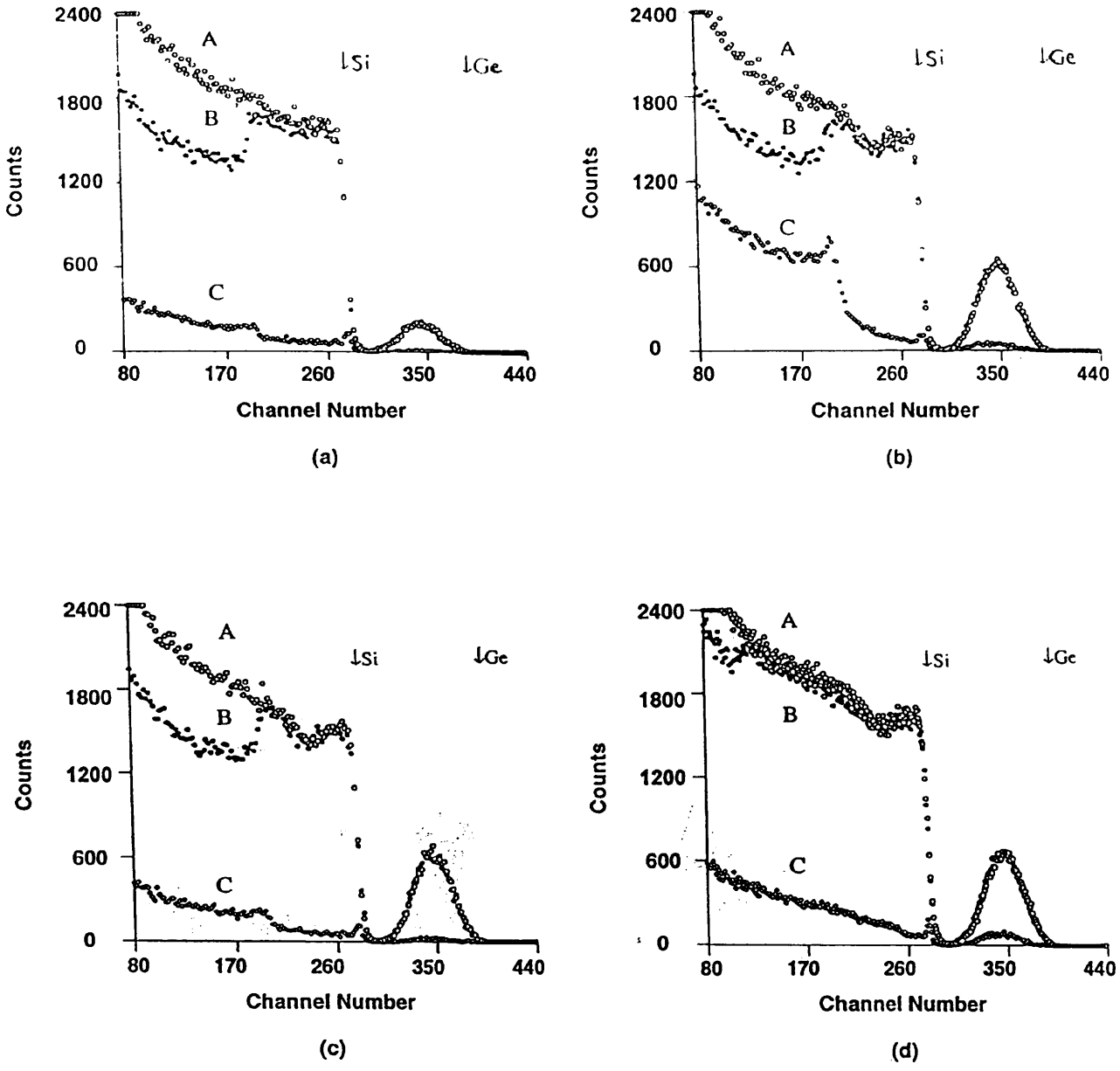

Figure 5.4 (a), (b), (c) and (d) are RBS spectra of samples from wafers 1,2,3 and 4 respectively. Curves A are the non-channelled spectra after annealing. Curves B and C are (100) channelled spectra from as implanted and after annealing samples respectively.

5.3.3.3 FTIR Results on Substitutional Carbon Concentration

Substitutional carbon gives rise to an infrared absorption band at 607 cm^{-1} [Newman 65] which is completely overlapped by the strong two phonon band of silicon at 610 cm^{-1}. Therefore in order to determine the C content, a subtraction was carried out using the signal from a sample cleaved from the non-implanted region at the edge. Results show there was a strong signal from the substitutional carbon sites in the carbon implanted wafers. A weak absorption signal at about 794 cm^{-1} from βSiC was also observed.

5.3.3.4 Double Crystal X-ray Diffraction Results of Composition and Strain Distributions in $Si_{1-x}Ge_x$ and $Si_{1-x-y}Ge_xC_y$ Alloys

Figure 5.5 (a), (c) and (d) show the experiment X-ray rocking curves (A) and simulations (B) of samples from wafers 1, 3 and 4 respectively. Figure 5.5 (b) curve A is experiment data from wafer 2 and curve B is experiment data from a piece from the un-implanted area of the same wafer.

In the simulation trial depth profiles of the Ge concentration measured by RBS and C concentration depth profile measured from SIMS (combined with the FTIR results) were used. Layer relaxation factors were used as the variable parameters to obtain a best fit of the simulated rocking curves to the experiment data.

The composition and strain as a function of depth is taken into account by using a model which dividing the implanted region in a number of thin lamellae within which

the composition and strain is assumed constant. The number of lamellae chosen was such that no change in the simulated data was observed when the number was increased. For some samples angular distribution of the diffuse scattering was also taken into account by adding the X-ray intensity distribution from an un-implanted region of the same wafers.

Figure 5.5 (a) shows the measured (curve A) and simulated (curve B) X-ray rocking curves from the sample taken from the LoGe wafer. The peak centered at 0 arcsecond is the reflection from the Si substrate and the satellite peaks on the left are from the SiGe alloy layer. The substrate peak is broader in the experimental data than predicted by the model. This could be due to strain associated with the high population of point defects which are known to be present in samples which have undergone a similar processing treatment as determined from our previous DLTS studies [Zhang 93]. The strain distribution is found to follow the misfit distribution due to the Ge composition distribution, indicating a coherently strained SiGe layer.

Figure 5.5 (b), curves A is the experiment X-ray rocking curve of the HiGe wafer, curve B is the experiment X-ray rocking curve from a piece of the un-implanted area in the same wafer. In curve A, the alloy related satellite peaks are no longer detected leaving only the substrate peak. The absence of the alloy related satellite peaks may result from the fact that the layer is highly defective, as observed from the XTEM micrograph. In curve B from the un-implanted region, the substrate peak is narrower than that from the implanted region, as is to be expected.

Figure 5.5 (c), curve A, is the X-ray rocking curve measured from HiGe+C wafer.

Curve B is a simulated X-ray rocking curve of ternary $Si_{1-x-y}Ge_xC_y$ based on the distribution of Ge and C described previously.

Figure 5.5 (d), curve A, is the X-ray rocking curve measured from HiGe+Si wafer. Curve B is a simulated X-ray rocking curve assuming that the strain distribution follows the Ge content with a relaxation factor less than 20% in the SiGe layer.

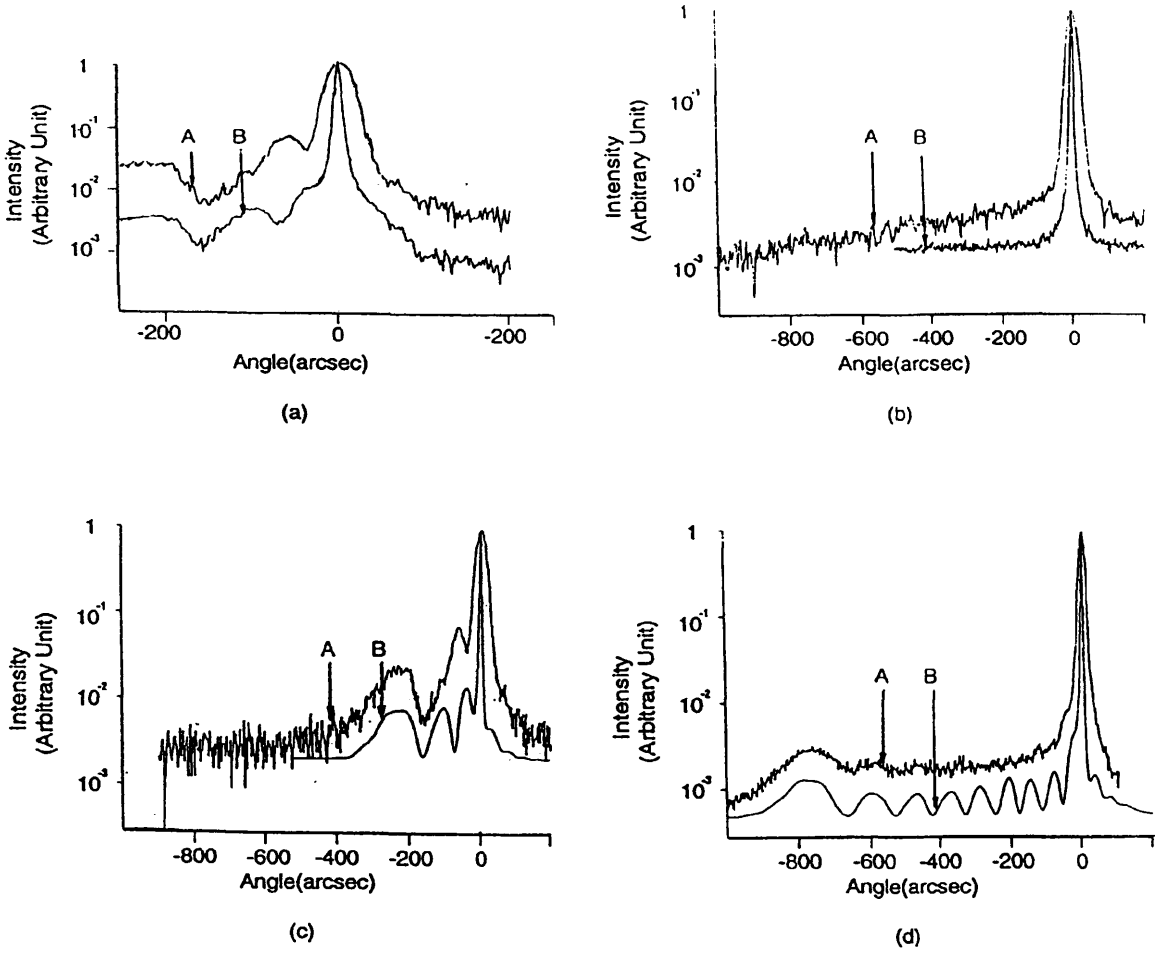

Figure 5.5 (a), (c) and (d) show the experiment X-ray rocking curves (A) and simulations (B) of samples from wafers 1, 3 and 4 respectively.
(b) curve (A) is experiment data from wafer 2 and curve (B) is experiment data from a piece from the un-implanted area of the same wafer.

5.3.4 Discussions

Paine et al [Paine 90] have studied SiGe alloys fabricated by ion implantation using transmission electron microscopy (TEM) technique and developed a model for the strain relief in compositionally graded SiGe layers. In this model a critical thickness concept similar to that applied to the introduction of dislocations during strained layer growth by MBE or CVD is used. The critical thickness is defined as the strained layer thickness at which the work done by the layer stress during defect formation equals the work that is required to introduce the defect in the material, as expressed in:

$$W_{defect} + W_{layer} = 0 \qquad (5.1)$$

where W_{defect} refers to the work needed to be done to introduce the defect and W_{layer} refers to the work done by the layer stress. If the critical level is not exceeded in the grown layer, the entire amorphous alloy regrows with lattice mismatch being elastically accommodated and no misfit induced defects are observed. If the critical level is exceeded then the material starts to relax and the defects are introduced.

Using this model and compare our wafer 1, LoGe and wafer 2, HiGe. We deduce that the $Si_{1-x}Ge_x$ layer formed by low dose Ge^+ implant is below the critical layer thickness for this alloy composition. X-ray rocking curves from experiment data and simulation result, shown in Figure 5.5 (a), reveal that the lattice mismatch being elastically accommodated and the XTEM reveals no misfit induced defects within the detection limits; only EOR defects can be detected. However, XTEM from wafer 2, HiGe, which

has been subject to a threefold increase in the germanium dose, illustrates that the critical level is exceeded during the SPE regrowth. In addition to the EOR defects, which are always present in these layers, the alloy layer now contains a substantial concentration of misfit induced defects between the amorphous/crystalline boundary and the sample surface. The misfit induced defects also have a big influence on the X-ray rocking curve spectrum: the satellite peaks of the $Si_{1-x}Ge_x$ alloy overlayer can no longer be detected in Figure 5.5 (b).

It has been demonstrated that though the equilibrium solubility of carbon in Si is very small, high concentration, far in excess of the equilibrium solubility, of implanted carbon could be incorporated onto substitutional sites using solid phase recrystallization and low temperature annealing following the ion implantation schedule [Strane 93].

From the X-ray rocking curve simulation and experiment results of the HiGe+C wafer, shown in Figure 5.5 (c), compressive strain caused by the presence of Ge has been partially compensated in proportion to the amount and profile of the implanted carbon; a $Si_{1-x-y}Ge_xC_y$ ternary alloy has been formed. The resultant alloy appears to be below the critical layer thickness for this particular composition. The XTEM micrograph of this layer in Figure 5.3 (c) shows no misfit induced defects other than EOR defects.

Our results are consistent with previous suggestions [Fukami 90] regarding the effects of a carbon co-implant: the strain due to the high dose Ge ion implantation is reduced. In addition, the small carbon atoms also act as sinks for point defects [Liefting 92] i.e. the excess silicon interstitial, which may impede the relaxation process through the reduced nucleation mechanism. This is supported by RBS (100) channelled spectra of

regrowth of wafer 2, HiGe, and wafer 3, HiGe+C; the level of lattice damage in the C co-implant sample is smaller.

In our postamorphisation process the initial α/c interface is much deeper in the substrate, and this has two effects on alloy relaxation:

(1) Reduces the dislocation nucleation probabilities [Hull 90]. Because the highest concentration of point defects is in the tail of the implant, this defect source is now made away from the SiGe alloy region by the postamorphisation process.

(2) Regrowth begins homoepitaxially in the HiGe+Si sample (with the Si^+ post-amorphisation), but inhomoepitaxially in the HiGe sample which facilitates the introduction of strain relieving defects so that alloy relaxed at an early stage. This can be explained in the following two situations:

(a) if the α/c interface is located in the Si substrate, as in the HiGe+Si sample, the SPE regrowth begins homoepitaxially towards the SiGe layer. As the compressive biaxial stresses develop when the growth continues, the strain energy accumulated until it reaches a "critical point", in our case around the Ge peak position (Figure 5.3 (d)), when relaxation via defects is energetically favored.

(b) if the α/c interface is in the vicinity of the SiGe alloy region, as in the sample HiGe, the SPE regrowth may begin inhomoepitaxially (a change in the α/c interface morphology from a single planar <001> growth habit to one which

is faceted parallel to the {111} of the crystal) in which case planar defects are more likely to be introduced at an early stage, even before the 'critical point' (as in situation (a)), to relax the alloy layer.

The reason that growth changed from <001> planar to one which is faceted parallel to {111} planes are more likely to introduce defects is as follows: When the growth is in the <001> direction on the (001) surface the requirement that tetrahedral bonding be preserved means that atoms undergoing attachment are forced into positions that preserve the crystal registry with the underlying atoms [Lau 82]. On these surfaces only one site is tetrahedral coordinated and only at this site the crystal registry is preserved. This means that planar defects are not easily introduced during SPE growth in this orientation. But when growth occurs on {111} habit planes, which is very much possible for inhomogeneous growth, there are two types of surface sites that preserve tetrahedral bonding: one results in a stacking fault while the other maintains the crystal registry. Although only one of these sites will result in the correct stacking of {111} planes, both sites are tetrahedral coordinated and, in terms of nearest neighbor interactions, look very similar to the atoms that are undergoing attachment across the α/c interface. Consequently, the possibility of an atom attachment error is large, particularly since the stacking fault energy in silicon is relatively small [Alexander 86].

Si postamorphisation is a good way to impede the alloy layer from relaxation if one wants to avoid forming the ternary alloy which has a different bandgap and strain compared with binary system [Soref 91].

5.4 Conclusion

We have contrasted the effects of either a carbon co-implant or a silicon post-amorphisation implant on the structural quality of $Si/Si_{1-x}Ge_x/Si$ heterostructures which have been formed by implanting high doses of Ge^+ ($3x10^{16}$ cm^{-2} and $9x10^{16}$ cm^{-2}). The maximum Ge concentrations are 2.4 and 8.7 at. % for the low dose and high dose cases respectively. The maximum Ge concentrations occur at a depth of 0.26μm below the sample surface. The thickness of the alloy layers is approximately 0.5μm. For the low dose Ge implant case the alloy layer appears, from XTEM and X-ray diffraction studies, to be perfectly strained. In the higher dose case, a high density of defects are observed crossing the region between the sample surface and the EOR defects. A carbon implant prior to the Ge^+ implant reduces the dislocation density considerably and greatly improved the quality of the alloy layer. Resulting from this process, a ternary $Si_{1-x-y}Ge_xC_y$ alloy is formed. Analysis of the strain in the layer indicates that the strain in the alloy layer is reduced to below the critical thickness point for misfit dislocation formation. We have also examined the effect of a deep Si postamorphisation which moves the end of range defects deeper into the substrate so that they are remote from the alloy region. We find in this case that the density and extent of the defects are much reduced compared to that from the sample implanted only with Ge^+. We attribute this effect to a model involving homogenous and inhomogeneous alloy growth which affects the introduction of strain relief defects

References

[Alexander 86] Alexander H., *Dislocations in Solids*, edited by Nabarro F. R. N. (Elsevier Sci. Pub.), vol. 7, 1986, pp 135

[Baslev 66] Baslev J., *Phys. Rev., 143*, 1966, pp 636

[Berti 91] Berti M., Mazzi G., Calcagnile L., Drigo A. V., *J. Mater. Res., Vol.6, no.10*, 1991, pp 2120

[Braunstein 58] Braunstein R., Moore A.R. and Herman F., *Phys. Rev., 109*, 1958, pp 695

[Brotherton 89] Brotherton S. D., Ayres J. R., Clegg J. B. and Gowers G. P., *J. Electron Mater., 18*, 1989, pp 173

[Chen 92] Chen J., Gao G. B. and Morkoc D. H., *Solid-State Electronics, vol. 35, no.8*, 1992, pp 1037

[Dodson 87] Dodson B. W. and Tsao J. Y., *Appl. Phys. Lett., 51*, 1987, pp 1325

[Fritz 87] Fritz I. J., *Appl. Phys. Lett., 51*, 1987, pp1080

[Fukami 90] Fukami A., Shuji Ken-ichi, Nagano T. and Yang C. Y., *Appl. Phys. Lett., 5(22)*, 1990, pp 2345

[Hart 81] Hart R. R., Hunsperger R. G., Dunlap H. L., and Marsh O. J., *Nucl. Instrum. Methods, 191*, 1981, pp 70

[Hull 90] Hull R., Bean J. C., Bonar J. M., Higashi G. S., Short K. T., Temkin H. and White A. E., *Appl. Phys. Lett., 56(24)*, 1990, pp 2445

[Im 92] Im S., Washburn J., Gronsky R., Cheung N. W. and Yu K. M. and Ager J. W., Mat. Res. Soc. Symp. Proc., 298, 1992, pp 139

[Jain 93] Jain U., Jain S. C., Nijs J., Willis J. R., Bullough R., Mertens R. P. and van Overstraeten R., *Solid State Electronics Vol.36, No.3*, 1993, pp 331

[Jones 91] Jones K. S. and Venables D., *J. Appl. Phys. 69*, 1991, pp 2931

[Kasper 88] Kasper E. and Bean J. C., Eds.: *Silicon Molecular Beam Epitaxy, Vols. 1 and 2* (CRC Press, Boca Raton, FL), 1988

[Kramer 92] Kramer K., Talwar S., Sigmon T. W., Weiner K. H., *Appl. Phys.*

Lett., 61(7), 1992, pp 769

[Lau 82] Lau S. S. and Mayer J. W., *Treatise on Materials Science and Technology*, edited by Tu K. N. and Rosenberg R. (Academic Press, New York), Vol. 24, 1982, pp 67

[LeGoues 91] LeGoues F. K., Meyerson B. S. and Morar J. F., *Phys. Rev. Lett., 66,* 1991, pp 2903

[Liefting 92] Liefting J. R., Custer J. S., Saris F. W., *Mat. Res. Soc. Symp. Proc.,* 1992, pp 235

[Lombardo 93] Lombardo S., Priolo F., Campisano S. U. and Lagomarsion S., *Appl. Phys. Lett. 62(19),* 1993, pp 2335

[Matthews 74] Matthews J. W. and Blakeslee A. E., *J. Cryst. Growth, 27,* 1974, pp 118

[Meyerson 88] Meyerson B.S., Uram K. J. and Legoues F. K., *Appl. Phys. Lett., 53,* 1988, pp 2555

[Miles 88] Miles R. H., McGill T. C., Chow P. P., Johnson D. C., Hauenstein R. J., Nieh C. W. and Strathman M. D., *Appl. Phys. Lett., 52,* 1988, pp 916

[Newman 65] Newman R. C. and Willis J. B., *J. Phys. Chem. Solids, 26,* 1965, pp 373

[Paine 90] Paine D. C., Howard D. J., Stoffed N. G., and Horton J. A., *J. Mater. Res., 5,* 1990, pp 1023

[Patton 88] Patton G. L., Iyer S. S., Delage S. L., Tiwari S. and Stork J. M. C., *IEEE Electron Device Lett., EDL-9,* 1988, pp 65

[People 85] People R. and Bean J. C., *Appl. Phys. Lett., 47,* 1985, pp 322

[Perovic 89] Perovic D. D., Weatherly G. C., Baribeau J. M. and Houghton D. C., *Thin Solid Films, 183,* 1989, pp 141

[Presting 92] Presting H., Kibbel H., Jaros M., Turton R. M., Menczigar U., Abstreiter G. and Grimmeiss H. G., *Semi. Sci. and Tech., 7,* 1992, pp 1127

[Rhee 88] Rhee S. S., Park J. S., Karunasiri R.P.G., Ye Q. and Wang K. L., *Appl. Phys. Lett., 53,* 1988, pp 204

[Soref 91] Soref R. A., *J. Appl. Phys., 70(4),* 1991, pp 2470

[Strane 93] Strane J. W., Stein H. J. and Mayer J. W., *Appl. Phys. Lett.,*

63(20), 1993 , pp 2786

[Temkin 86] Temkin H., Antreasyan A., Olsson N. A., Pearsall T. P. and Bean J. C., *Appl. Phys. Lett., 49(13)*, 1986, pp 809

[Tuppen 89] Tuppen C. G., Gibbings C. J. and Hockly M., *J.Cryst. Growth, 94*, 1989, pp 392

[van der Merve 63] van der Merve J. G., *J. Appl. Phys., 34*, 1963, pp 123

[Zhang 93] Zhang J. P., Fan T. W., Gwilliam R. M., Hemment P. L. F., Wen J. Q., Evans J. H., Peaker A. R., *Nuclear Instruments and Methods in Physics Research, B74*, 1993, pp 127

[Zhang 94] Zhang J. P., Wilson R. J., Hemment P. L. F., Claverie A., Wen J. Q., Evans J. H., Peaker A. R., Parker G., *Nucl. Instru. Meth. in Physics Research B 84*, 1994, pp 222

Chapter 6 Defects in Silicon Power Devices

6.1 Introduction

Some stages of silicon power device processing can generate significant concentrations of deep states which result in changes in the electrical properties of power devices. **Section 6.2** of this chapter deals with (1) deep level defects detected in the power p-i-n diode materials which had abnormally short minority carrier lifetimes (2) deep level defects in the Gate Turn Off (GTO) thyristor materials which had abnormally high leakage currents and short lifetimes. The purpose of the study in this chapter was to trace the origin of these deep level states so as to be able to understand and control their effects on the electrical properties of devices. In order to find out whether the deep level states were impurities introduced as a result of the production process or defects inherent in the "as delivered" silicon materials and "activated' by defect reactions during thermal treatments, we have, as discussed in **section 6.3**, simulated some segments of the processes by a conventional Rapid Thermal Anneal cycle (RTA) followed by a furnace anneal at various temperatures and finally a quenching treatment, of the "as delivered" materials. This provided a highly reproducible and clean process cycle which very effectively activated the deep level states in question. But first we need to discuss the general properties of silicon power devices and how the neutron transmutation doped (NTD) silicon materials widely used in the power device industry are prepared.

General electrical properties of silicon power devices: Power semiconductor devices operate at high currents and/or voltages. Most low frequency power devices are made of silicon because of its high thermal conductivity and uniformity. The power devices include diodes, thyristors, bipolar transistors, power MOS transistors and static induction transistors. Some power devices are switching devices while others are used for either switching or linear power amplification. Some of their main characteristics are:

(1) To carry large currents with a uniform current density over a large device area.

(2) The device forward voltage drop should be low to reduce heat dissipation. A low forward voltage drop is achieved via the conductivity modulation in the material with a long lifetime.

(3) At its 'OFF' state the voltage blocking capability should be sufficiently high.

Compromise should be made in the actual device design, for example, the high voltage blocking capability requires a thick region of low doping density on at least one side of the main junction while the low forward voltage drop requires the opposite.

Defects related to Neutron Transmutation Doped (NTD) silicon and their effects on material electrical properties:

(1) Neutron transmutation doping of silicon and the defects resulted from it

Neutron transmutation doping (NTD) of silicon was commercially introduced in 1973

[Schnoller 74]. The advent of this technique was a great step ahead in the development of high power semiconductor devices as it allows tight resistivity tolerance and excellent homogeneity of the silicon material. Resistivity fluctuation can lead to weak spots in the device area where premature avalanche and hot spots may form. Conventionally doped silicon shows local doping variations of $\pm$ 15% but the NTD silicon shows only $\pm$ 3% variation [Ammon 92]. Furthermore due to the accurate determination of the neutron flux the resistivity target can be specified within very tight tolerance at $\pm$ 7%. Phosphorus doping of the original silicon crystal is achieved by irradiating a dislocation free high purity undoped single crystal silicon (usually float zone Si) by thermal neutrons from a nuclear reactor. The neutron flux transmutes Si atoms first into a Si isotope with a 2.62 hours half-life which then decays into phosphorus. The main reaction is expressed as:

$$^{30}Si(n,\gamma)\,^{31}Si \xrightarrow[2.62\ \text{hours}]{} {}^{31}P+\beta \qquad (6.1)$$

Where (n, γ) represents (neutron absorption, γ emission (high energy photon emission)) and β represents β decay (high energy electron emission). In addition to the main reaction there are secondary reactions leading to the production of sulfur due to thermal neutron absorption by the phosphorus (P^{31}) and production of magnesium by the fast neutron absorption by silicon (Si^{30}).

Thermal neutrons (with energy less than 0.1 MeV) cannot knock out an atom from a lattice

site, but are absorbed by the nucleus and cause beta particle emission. When the target atoms undergo the γ and β decays, the recoil produced displaces the transmuted atom from its lattice site, and thus creates a defect near it. The corresponding recoil energy (about 0.8 keV) is consumed during atomic displacement [Smirnov 80]. The nuclear reactors in which the thermal neutron capture is performed for the doping are known to contain a background of fast neutrons. Fast neutrons with energy of around 50 keV interact with Si atoms, developing a cascade of displacements resulting in the formation of a large disordered region around the recoil track. Gossick, Cleland and Crawford were among the first to postulate the existence of defect clusters in NTD semiconductors [Gossick 59]. Bertolotti was the first to actually observed defect clusters in NTD semiconductors [Bertolotti 68].

(2) Effects of the radiation damage on material electrical properties

Resistivity:

It is invariably found that after the neutron irradiation process the silicon resistivity exceeded 10^5 Ω-cm. This is a direct consequence of the radiation damage which produces a large number of deep level states which act as compensating centers and cause the resistivity change in the material. Heat treating the wafers after irradiation at a sufficiently high temperature anneals out this damage [Herzer 77]. Most investigations showed [Stone 81][Maekawa 88] that a relatively mild annealing procedure (600°C-900°C, a few minutes to a few hours) was sufficient to achieve a full recovery of the target resistivity. In general 800°C is found to be the best compromise. At higher temperatures the minority carrier lifetime of the material could be reduced, an issue which will be discussed next.

Lifetime:

Minority carrier lifetime is another major concern for power semiconductor devices. A long minority carrier lifetime is necessary in power devices in order to obtain acceptable low forward voltage drop during current conduction (via conductivity modulation) and low leakage current in the blocking state. It is well known that immediately after a radiation the minority carrier lifetime is extremely low. This is because the radiation damage produces a large number of deep level states. These defects can act as recombination or generation centers and affect the material's recombination or generation lifetimes.

Again, annealing of those irradiated materials at a proper temperature would increase the minority carrier lifetime. Lifetime data obtained from NTD materials subjected to isochronal annealing (1 hour) in an argon ambient is shown in Figure 6.1 (a) for a temperature range of 400°C to 900°C [Jayant 79]. It could be seen that the lifetime was very low at 400°C and monotonically increased approaching 700°C, beyond which temperature the lifetime did not increase anymore. Actually higher temperature annealing can degrade the lifetime of NTD materials. Figure 6.1 (b) shows NTD materials subjected to isochronal annealing (4 hours) between 800°C and 1200°C. It could be seen that the lifetime decreased with the increasing annealing temperature in the range from 800°C to 1000°C [Ammon 88].

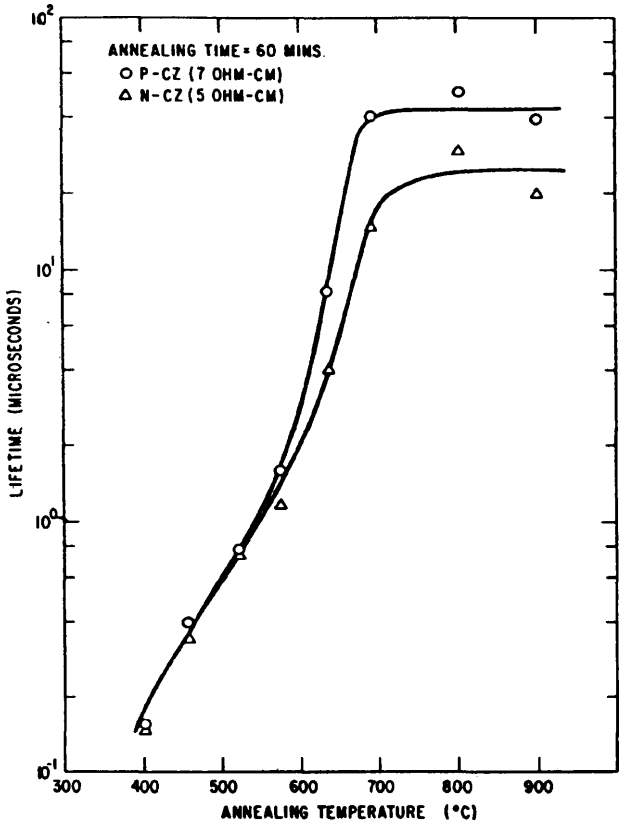

(a)

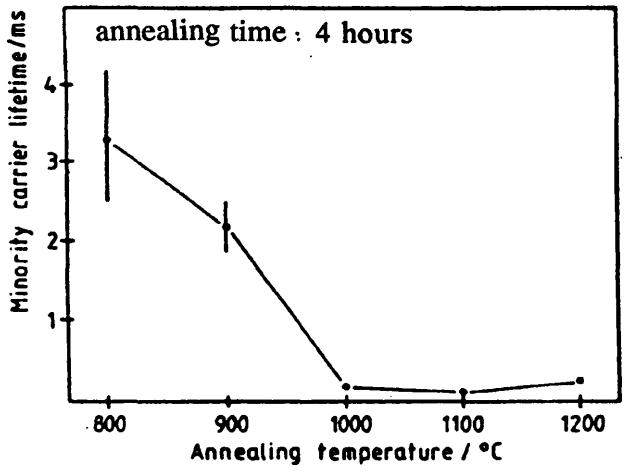

(b)

Figure 6.1 The minority carrier lifetime as a function of the annealing temperature after irradiation of neutrons
(a) 400°C - 900°C, for 1 hour, *after Jayant [Jayant 79]*
(b) 800°C -1200°C, for 4 hours, *after Ammon [Ammon 88]*

6.2 Deep Level Defects in Power Device Materials Which had Degraded Electrical Properties

6.2.1 Deep Level Defects in Power p-i-n Diode Materials Which had Abnormally Short Lifetimes

6.2.1.1 Sample Information

The p-i-n diode is a pn junction with a doping profile tailored so that an intrinsic layer, the i-region (approximated by a high resistivity n-type NTD silicon in practice) is sandwiched between the p-layer and the n-layer. The p-i-n diodes have many advantages over the conventional pn diodes. For example the p-i-n diode allows a much thinner wafer than its conventional pn counterpart in attaining the same reverse voltage ratings, thus facilitating improved switching properties. The p-i-n diode in this work is fabricated as following: a low concentration n-type NTD silicon wafer is chosen as the starting material (i-region). A diffusion using gallium or aluminum is carried out to form the p region on one side and the n region is then formed on the other side by phosphorus diffusion. Phosphorus gettering is applied as the final stage of the diffusion process to remove metallic contaminants.

The material studied in section 6.2.1 was the i region (low concentration n type) which had abnormally short minority carrier lifetimes. The starting material was n-type <111> NTD silicon whole wafers, with resistivity ~300 Ω-cm, diameter 100 mm and thickness 990 μm.

The i region of the power diode material was assessed at the process stage after the p region had been formed.

6.2.1.2 Results

6.2.1.2.1 Minority Lifetime[1]

A: Lifetime Measured by Open Circuit Voltage Decay (OCVD) Method

Experimental configuration and sample preparation: The OCVD method is a well established technique for the measurement of minority carrier lifetimes in p-i-n diodes. Figure 6.2 shows a typical circuit for measuring the OCVD lifetime of a p-i-n diode. The diode under test is forward biased (the switch is initially closed) to inject minority carriers into the i-region then, when a steady state has been established, the switch is opened and the lifetime τ is obtained from the decay of the voltage across the diode according to:

$$\tau^{-1} = \frac{e}{nkT}\frac{dV}{dt} \qquad (6.2)$$

Where V is the voltage across the diode when the circuit is open. n=2 or 1 depending on the injection condition (n=1 for low injection and n= 2 for high injection). Figure 6.3 shows a typical voltage decay curve observed in an OCVD experiment. An initial rapid decay is

[1] the OCVD lifetime measurements were done at GEC and the μPCD lifetime maps at Cascade Scientific using the Semilab WT85 Lifetime Scanner

followed by two linear regions which is associated with high and low injection conditions respectively.

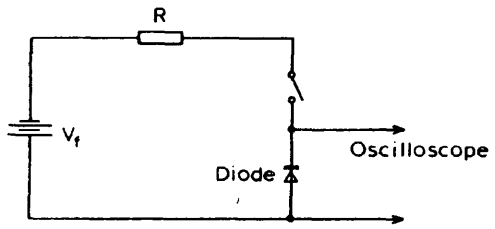

Figure 6.2 Circuit for measuring the OCVD lifetime of a p-i-n diode. The switch is initially closed under forward bias condition to inject minority carriers into the i-region then, when a steady state has been established, the switch is opened and the lifetime τ is obtained from the decay of the voltage across the diode.

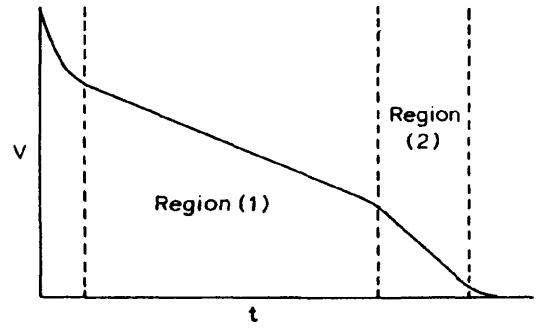

Figure 6.3 A typical voltage decay (V) versus time (t) curve observed in an OCVD experiment. An initial rapid decay is followed by two linear regions which is associated with high and low injection conditions respectively.

Results: A map was obtained by dicing the prepared wafer into small pieces (7 mm square) for individual measurement. Figure 6.4 shows an example of the results. The numbers in the squares represent lifetime values in μs.

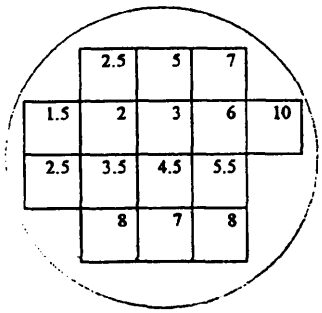

Figure 6.4 Results from OCVD method, numbers in squares are lifetime values in μs.

B: Lifetime Measured by Microwave Photoconductive Decay (μPCD) Method

Experimental configuration and sample preparation: μPCD is a non contact technique which uses photoconductive decay (PCD) combined with the microwave absorption. This is based on the fact that the absorption constant for microwave radiation propagating through a semiconductor is directly proportional to the conductivity [Gibson 56]. A laser pulse generates excess minority carriers which are monitored via the microwave absorption measurement. This technique avoids the problem of forming good electrical contacts to a sample. In order to reduce the recombination of carriers at the wafer surface so that lifetime values characteristic of the bulk could be measured [Waldmeyer 88] [Grivickas 92], the wafer surfaces are passivated in this study. Otherwise the measured "lifetime" could be the time that the generated carriers took to diffuse to the sample surface. Before the μPCD measurement the wafer had been thinned to remove the junctions leaving only the i region.

Results: Figure 6.5 shows a lifetime map obtained using this method. It had a lifetime value ranging from 1.7 μs to 10.3 μs across the wafer and exhibited a ring-like pattern. The lowest lifetime was seen near the center of the wafer. Comparing Figure 6.4 and Figure 6.5 it can be seen there is a broad agreement between the results from these two methods.

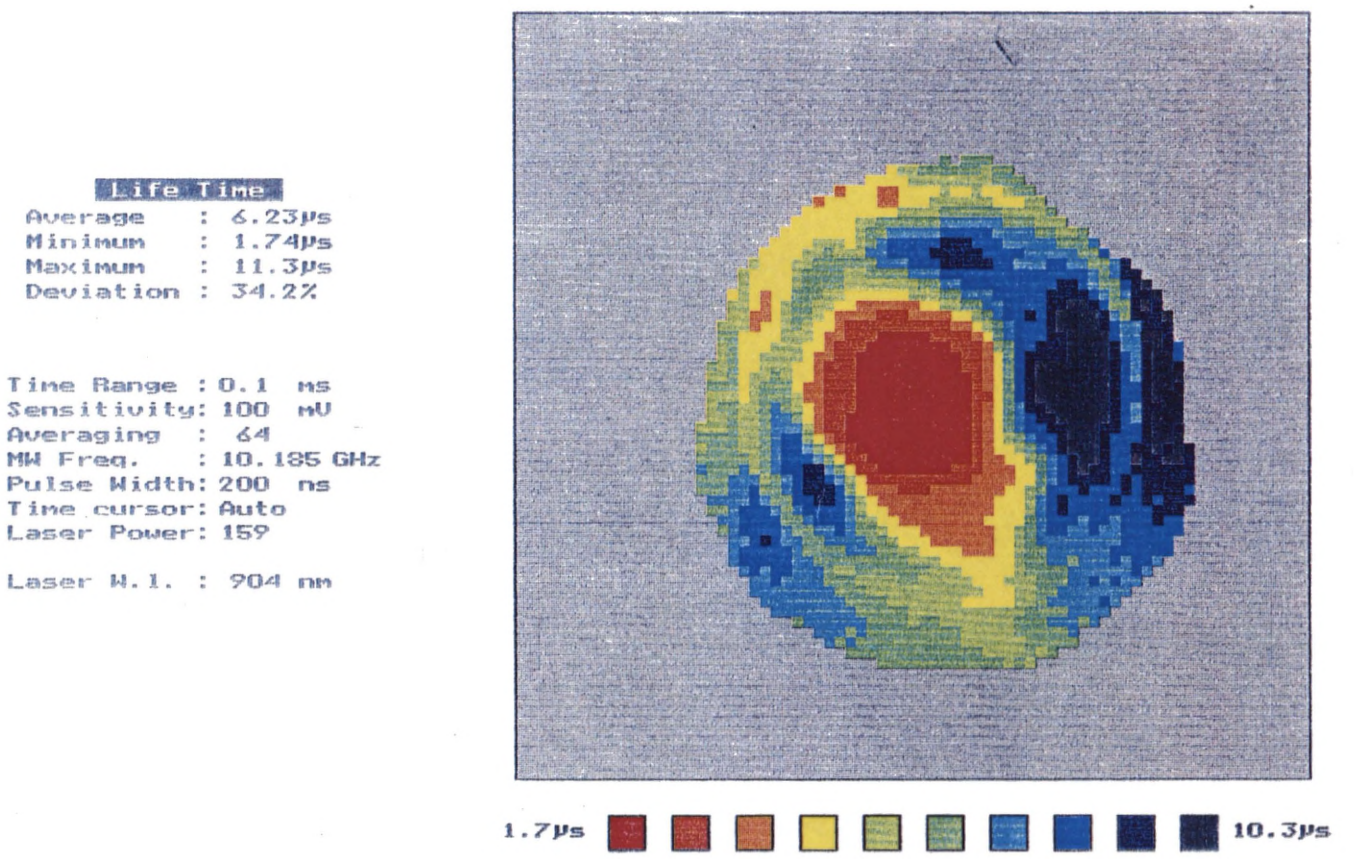

Figure 6.5 Lifetime map measured by µPCD method

6.2.1.2.2 DLTS Results

Sample preparation: In order to correlate deep level defects with the lifetime results, DLTS measurements were carried out on samples cleaved from various positions corresponding to different lifetime values (μPCD measured wafer, refer to Figure 6.5). Sample preparation for the DLTS measurements for each cleaved piece used a standard silicon cleaning method. Solvent (trichloroethylene, acetone and methanol) and high purity deionized water rinse was used to remove the surface contamination. Organic and metallic contamination was next removed by 10 minutes soaks in hydrogen peroxide solutions (at 80°C), H_2O: H_2O_2: NH_4OH (5:1:1) and H_2O: H_2O_2: HCl (6:1:1) [Kern 70] respectively. After the cleaning gold was evaporated on one side of the sample surface to form Schottky diodes of 1 mm diameter circles and indium on the other surface to form Ohmic contacts.

Results: Four deep level states labelled T_{L1}, T_{L2}, T_{L3} and T_{L4} were detected. Figure 6.6 shows DLTS spectra of two typical samples: one taken from the wafer position with the longest lifetime (10 μs) and the other from the position with the shortest lifetime (2μs). For convenience the lifetime map is also shown above the DLTS spectra. Direct measurement of the capture cross section of each of the four deep level states was carried out. Table 6.1 gives the summary of the activation energy, and the measured carrier capture cross section of each of the four deep level states. Also listed in Table 6.1 are the defect concentrations in the 10 μs and 2 μs samples.

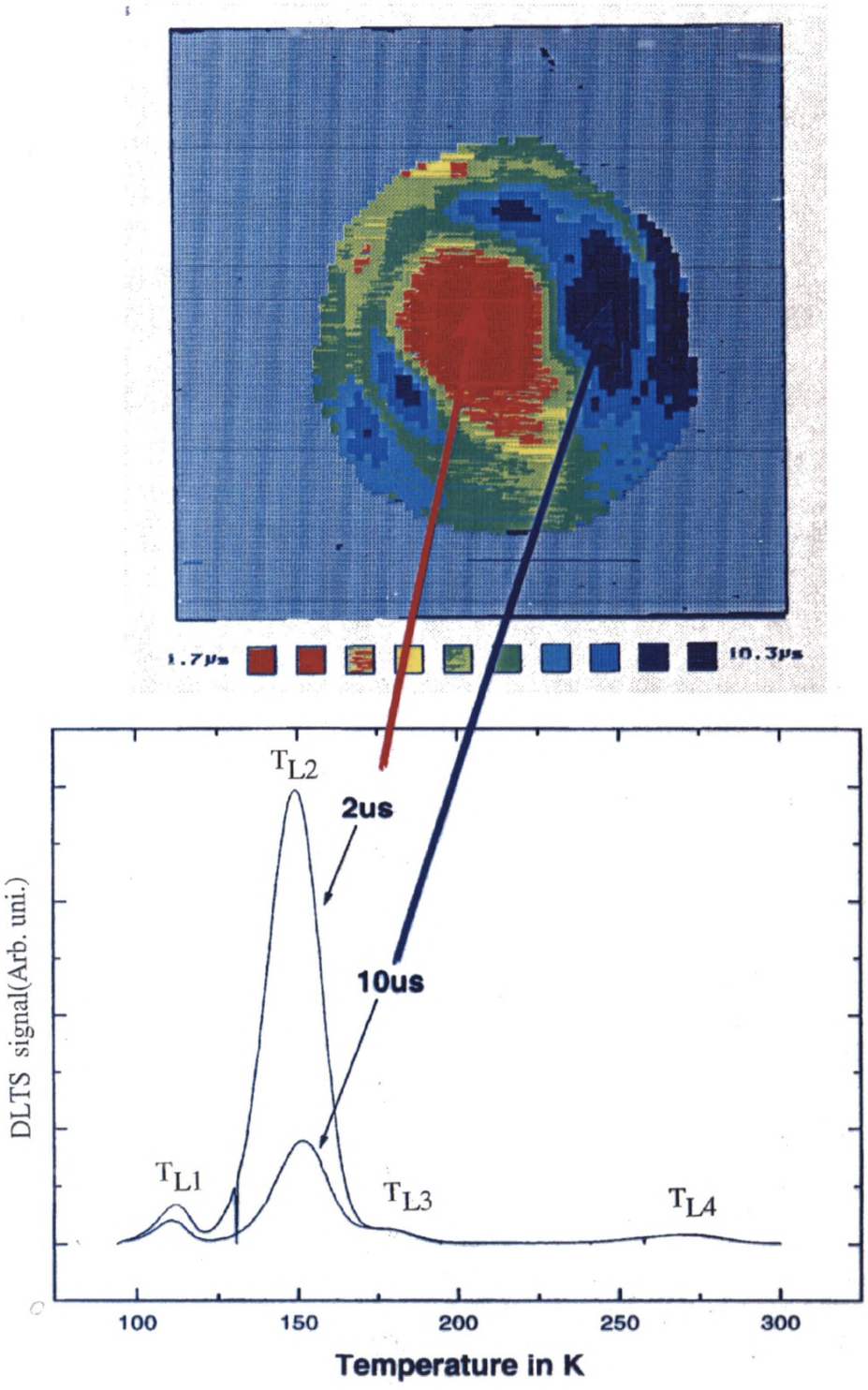

Figure 6.6 DLTS spectra of two samples: one had the longest lifetime (10 μs) and the other had the shortest lifetime (2 μs) over the wafer according to the μPCD lifetime map which is shown above the DLTS spectra. DLTS were carried out at $V_{Reverse}$= -30 volts, $V_{Forward}$ = 0 volt, and the forward filling time T_{Fill}=10ms. The DLTS spectra are plotted at 50/s rate window.

Deep Level Name	Activation Energy (meV)	Electron capture cross section (cm^2)	Deep level concentration 10 μs sample ($x10^{12}$ cm^{-3})	Deep level concentration 2 μs sample ($x10^{12}$ cm^{-3})
T_{L1}	185	4.7×10^{-16}	3.1	5.5
T_{L2}	275	5.7×10^{-17}	13.3	60
$T_{L3.}$	260	1.1×10^{-16}	1.8	1.8
T_{L4}	532	1.1×10^{-16}	1.3	1.3

Table 6.1 Activation energy, electron capture cross section of each of the four deep level state shown in Figure 6.6. The defect concentrations of the four deep levels in the longest and shortest lifetime samples are also given.

It can be seen from Table 6.1 that the T_{L2} was present in the highest concentration. It approached the shallow doping density (~ 1×10^{14} cm^{-3}) in the 2 μs sample. Also we have noticed its concentration values scaled well with the lifetime values in all the samples. The two samples listed in Table 6.1 was only a typical example.

6.2.1.3 Discussions

It was found the concentration of deep state T_{L2} correlated well with the lifetime map (Figure 6.6). This deep level was present in the highest concentration among the four deep level states. Comparing the thermal emission characteristics of this deep state with the published data we found that a similar deep level state has been observed in other people's work concerning power devices and often there was a related lifetime problem [Crees 83][Paxman 79].

T_{L2} had a similar emission characteristics to a very commonly observed defect first reported by Yau [Yau 74]. It was associated with a vacancy complex and referred to as a quenched-in donor, but no definitive assignment of its physical structure was achieved.

Although the thermal emission characteristics of T_{L2} was also found similar to that of a titanium related defect (titanium is known to kill the lifetime), the electron capture cross section of the titanium related defect was much higher ($3x10^{-15}cm^2$) than our result ($5.7x10^{-17}cm^2$).

Di Marco [Di Marco 89] observed a similar deep level generated in rapid thermal annealed or electron beam annealed CZ and FZ samples, however no identification was made there either.

A deep level state identical to T_{L2} was generated in the "as-delivered" materials (without any power device production processing) after certain thermal treatments. Further discussions will be given in section 6.3.

The deep state T_{L4} had a very similar thermal emission characteristics to that of the so called process-induced defects or "gold" acceptor level [Mesli 87]. Both defects were reported as recombination centers, however, in our samples no correlation between T_{L4} and the lifetime results was observed. T_{L4} was also similar to a deep level state often referred to as group D defect reported in plastically deformed silicon [Omling 85]. Group D defects were suggested to be point defects located in the vicinity of or inside the dislocations.

For the deep state T_{L1} the lineshape of it was point defect-like and the thermal emission characteristics was similar to the oxygen-vacancy centre. It was generated in the "as delivered" materials after certain thermal treatments. Its thermal emission and annealing characteristics will be further discussed and compared with the literature in section 6.3.

Trap T_{L3} had identical thermal emission characteristics as a deep level state reported in power device materials where it was suggested to have assisted in gettering lifetime killing impurities [Crees 83]. Their evidence was that the sample which had the highest concentration of the defect turned to be the sample which had the longest lifetime after the gettering process. Yet no assignment was made in that paper. Another similar deep state was found in n-type epitaxial layer and this level was produced during oxidation, yet no identification was given [Indusekhar 86] in that paper.

6.2.2 Deep Levels in the GTO Thyristor Materials Which had Abnormally High Leakage Currents and Short Lifetimes

6.2.2.1 Sample Information and Experimental Configuration

A four-layer p-n-p-n structure has three p-n junctions in series. When the out terminals are connected to the p1 (anode), P2 (gate) and n2 (cathode) regions, it is called the semiconductor-controlled rectifier (SCR) or thyristor. A typical doping profile of a p-n-p-n structure is shown in Figure 6.7 (a). The Gate-Turn-Off (GTO) thyristor is one special type

of SCR that is turned on by forward-biasing the cathode junction and turned off by reverse-biasing the same junction. The doping profile is characterized by a low p2 region sheet resistance and an interdigitated cathode region to ensure even distribution of the reverse bias across the cathode junction at turn-off. Another characteristics of GTO thyristor is the anode shorting and defocussing in order to improve the turn-off and temperature properties. Figure 6.7 (b) is a schematic diagram showing the structure of GTO finger with the anode defocussing shorts, n^+. Samples studied in section 6.2.2 were p^+nn^+ ($p2\text{-}n1\text{-}n^+$ in Figure 6.7 (b)) diodes taken from the GTO thyristor materials which had abnormally high leakage currents and high forward voltage drop (short lifetimes). The majority carrier traps were detected using the normal DLTS measurement techniques. For the observation of minority carrier emission. A pulse into forward bias of the diodes was used to inject minority carriers (refer to chapter 3, section 3.1.3.1.2 for detailed discussion of this method)

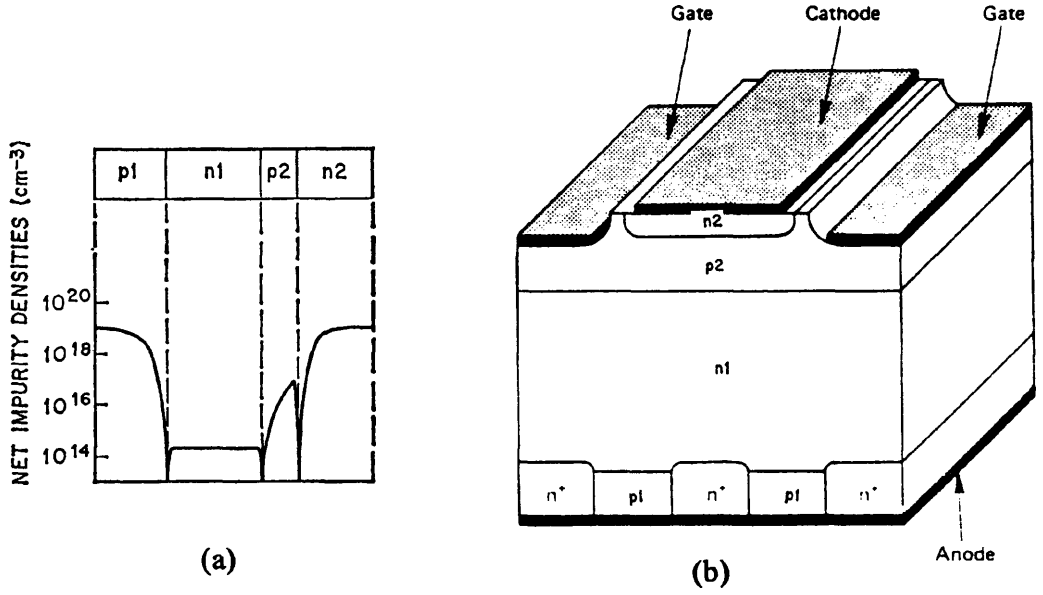

Figure 6.7 (a) a typical doping profile of a p-n-p-n structure, the n1 region is ~900 μm
(b) a schematic diagram showing the structure of GTO finger with the anode defocussing shorts, n^+.

6.2.2.2 DLTS Results

6.2.2.2.1 Majority Traps

Three majority (electron) carrier traps labelled T_{E1} , T_{E2} and T_{E3} were detected and the DLTS spectra are shown in Figure 6.8. Table 6.2 gives the activation energy (T_{E2} could not be resolved adequately for detailed analysis and hence the activation energy was not derived) and capture cross section (measured directly) of T_{E1} and T_{E3}. For T_{E1} the electron capture cross section was measured at 170K. The electron capture cross section of T_{E3} was studied as a function of temperature and it did not vary between 253 K and 280 K.

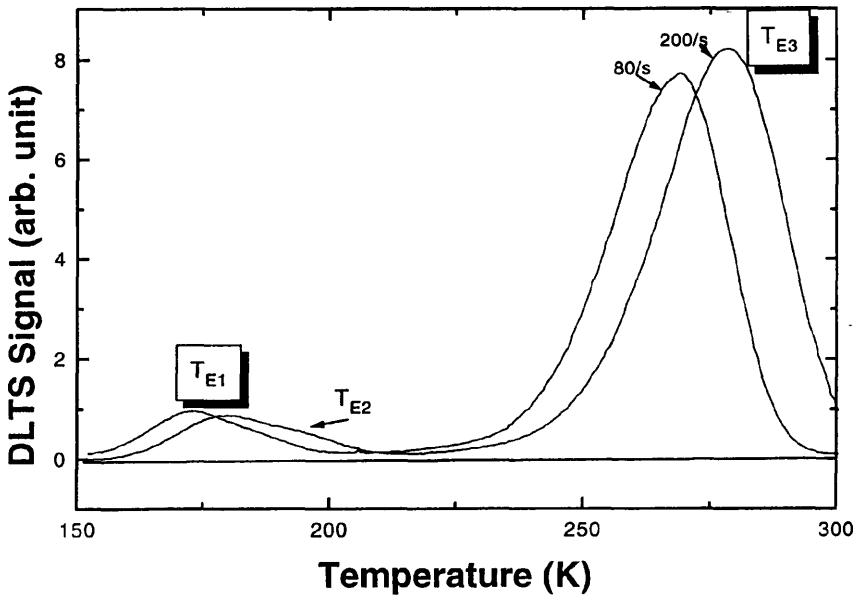

Figure 6.8 DLTS spectra (at rate windows 200/s and 80/s) showing majority traps T_{E1} T_{E2} and T_{E3}. Measurements were carried out at $V_{Reverse}$= -3 volts, $V_{Forward}$ = 0 volt and forward filling time T_{Fill}= 3 ms.

Deep Level States	Peak Temperature at 200/s (K)	Activation Energy (meV)	Capture cross section (cm^2)
T_{E1}	179	350	2.2×10^{-16}
T_{E3}	278	540	2.1×10^{-16}

Table 6.2 Activation energy and electron capture cross section of T_{E1} and T_{E3}.

6.2.2.2.2 Minority Traps

Three minority deep level states were detected which are illustrated in Figure 6.9. Table 6.3 gives the activation energy of the hole emission of the two minority deep levels (one minority deep level could not be clearly resolved hence the activation was not derived).

Deep Level States	Peak Temperature at 200/s (K)	Activation Energy (meV)
T_{H1}	165	340
T_{H2}	246	530

Table 6.3 Activation energy of T_{H1} and T_{H2}.

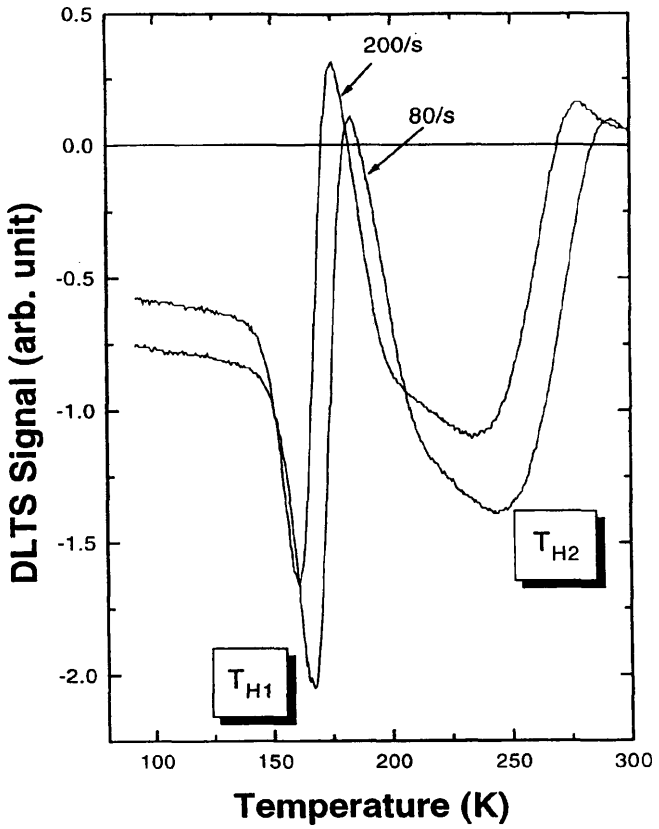

Figure 6.9 DLTS spectra (at rate windows 200/s and 80/s) of minority (hole) traps T_{H1} and T_{H2}. Measurements were carried out at $V_{Reverse}$= -3 volts, $V_{Forward}$ = +0.7 volt, and the forward filling time was T_{Fill}= 3 ms.

6.2.2.3 Discussions

Figure 6.10 are Arrehius plots of the T_{E3} and T_{H1} traps. Also plotted are "gold" acceptor and "gold" donor deep levels from the literature [Wu 82] [Sato 70][Wang 76]. From figure 6.10 it can be seen that the T_{E3} and T_{H1} traps have identical thermal emission characteristics to those of "gold" acceptor and donor levels respectively. The measured electron capture cross section of T_{E3} agreed well with that of "gold" acceptor level from the literature [Sah 70][Lang 80][Wu 82][Brotherton 78]. The temperature behaviour was also consistent with previous work (independent of temperature).

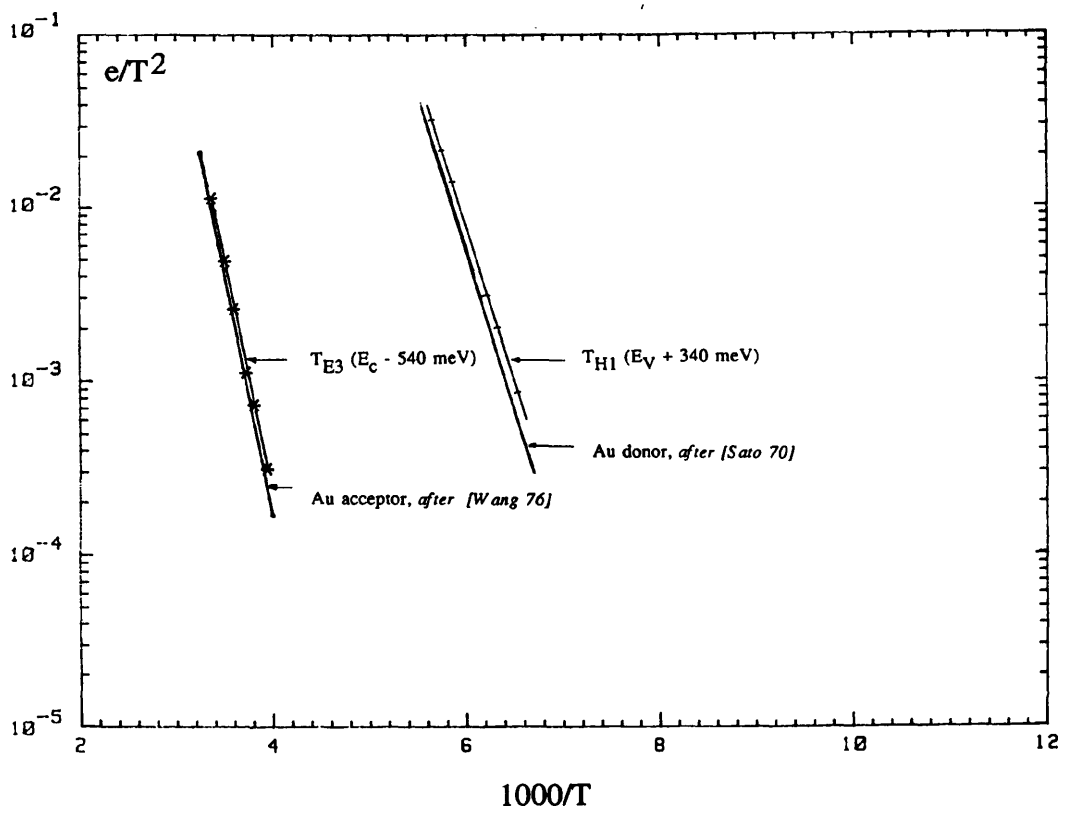

Figure 6.10 Arrehius plots of T_{E3} (electron emission activation energy is 540 meV) and T_{H1} (hole emission activation energy is 340 meV) traps. Also shown are "gold" acceptor and donor deep levels from the literature [Wang 76] [Sato 70].

The weak T_{E1} level was probably due to the fact that the sample had a slightly graded junction, this peak was therefore from the "gold" donor level in the p side, since hole emission was a majority carrier process in the p side material. This phenomena was also observed in Lang's work [Lang 80].

T_{H2} could be due to the relaxation of hole occupancy taking place at the "gold" acceptor as seen in p type material [Mesli 87]. It interacted with the conduction and the valence

band as should be expected from a neutral recombination center for which the sum of thermal activation energies for both carriers (530+540 = 1.07 eV) should be close to the silicon gap within experiment error. This was very important because if it did not interact with the valence band then the equilibrium charge state should be positive, which was not expected for the "gold" acceptor level. It was a crucial point to distinguish the "gold" acceptor level from the process-induced defect (the "gold" acceptor level and the process-induced defect have identical thermal emission characteristics, further discussion will be given in section 6.3), which was reported to be a donor type deep level state [Yau 74].

6.3 Defects in the "As Delivered" Power Device Materials After Thermal Treatments

Since power devices have undergone complex processing routines, in order to trace the origin of the deep states which had affected the electrical properties of power devices as discussed in section 6.2, it was important to examine the "as delivered" silicon materials to find out whether the deep states were impurities introduced as a result of the production process or defects inherent in the "as delivered" silicon and "activated' by defect reaction during the thermal treatments. We have simulated the segments of the processes inducing the deep states by a conventional Rapid Thermal Anneal cycle (RTA) followed by a furnace anneal at various temperatures in the "as delivered" materials. This provided a highly reproducible and clean process stage which very effectively created the deep states in question.

6.3.1 Sample Information and Preparation

Three groups of samples were investigated in section 6.3. They were wafers from three silicon manufactures named manufactures X, Y and Z in this context. Specifications of the three wafers are given in Table 6.4. For each wafer from the three manufactures the following preparations were made. A small piece (**control sample**) and a big piece were cleaved from the wafer and were chemically polished to mirror finish. Both pieces were thoroughly cleaned using the standard silicon cleaning method described in section 6.2.1.3. The big piece was then annealed in a conventional rapid thermal annealer in N_2 for 15 seconds. The maximum temperature reached was 925°C. This big piece was then cleaved into 6 smaller pieces. Among the 6 smaller pieces one was left as it was and the other 5 pieces had a further furnace annealing at temperatures 500°C, 600°C, 700°C, 800°C and 900°C respectively. The names of these samples are listed in Table 6.5. The furnace annealing was carried out in N_2 for 10 minutes after which the samples were rapidly pulled out and then quenched into silicone oil to freeze the defects. All the samples were then thoroughly cleaned and gold was evaporated on the front to form Schottky diodes and indium on the back to form Ohmic contacts. Standard DLTS measurements were carried out to detect the majority carrier traps. For reasons which will be given in the discussion section, MCTS (described in Chapter 3, section 3.1.3.1.3.3) measurements were carried out on samples which had undergone rapid thermal annealing and a subsequent furnace annealing at 900°C. There were some modifications in terms of the illumination arrangement for the MCTS measurements here.

Type of Materials (n-type <111>)	Manufacture	Resistivity (Ω-cm)	Wafer Thickness (μm)	Wafer Diameter (mm)
NTD	X	215	810	77.5
NTD	Y	242	1000	76
FZ	Z	225	940	100

Table 6.4 Specifications of wafers studied in section 6.3

Manufacture	Annealing Conditions[2]					
	RTA only	RTA+ 500°C	RTA+ 600°C	RTA+ 700°C	RTA+ 800°C	RTA+ 900°C
X	X(RTA)	X(RTA +500)	X(RTA +600)	X(RTA +700)	X(RTA +800)	X(RTA +900)
Y	Y(RTA)	Y(RTA +500)	Y(RTA +600)	Y(RTA +700)	Y(RTA +800)	Y(RTA +900)
Z	Z(RTA)	Z(RTA +500)	Z(RTA +600)	Z(RTA +700)	Z(RTA +800)	Z(RTA +900)

Table 6.5 Names of samples studied in section 6.3

[2] RTA+500°C means a rapid thermal anneal plus a furnace anneal at 500°C

6.3.2 Results

DLTS results of all the control samples showed no deep level states within detection limit ($\sim 10^{10}$ cm^{-3}). There were 11 deep level states in total in the other samples. Figure 6.11, 6.12 and 6.13 show the DLTS spectra from all these samples, i.e. the samples listed in Table 6.5 from manufactures X, Y and Z respectively. The measured concentration of each defect is given in Table 6.6. Also listed in Table 6.6 is the activation energy for each defect. Traps T_9 and T_{10} could not be resolved properly from any DLTS scans therefore the activation energy of them were not derived.

The first point to make from the observation of the three groups of spectra is that the DLTS spectra have showed identical features from the X(RTA+900), Y(RTA+900) and Z(RTA+900) samples. Actually the spectra from the modified MCTS measurements also looked the same among the three samples. The MCTS spectrum of X(RTA+900) sample will be presented in the discussion section in order to be compared with the spectra from the literature.

The second point to make is that the DLTS spectra from the samples from manufacture Y is much more simple than from the other two manufactures. This implied that many of the deep level states were manufacture dependent.

The third point to make is that the general trend of the evolution of the DLTS spectra in X-series samples is the same as in the Z-series which could suggest there exist a common basis in terms of defect formation and evolution mechanism and this common basis was closely related to the thermal treatments.

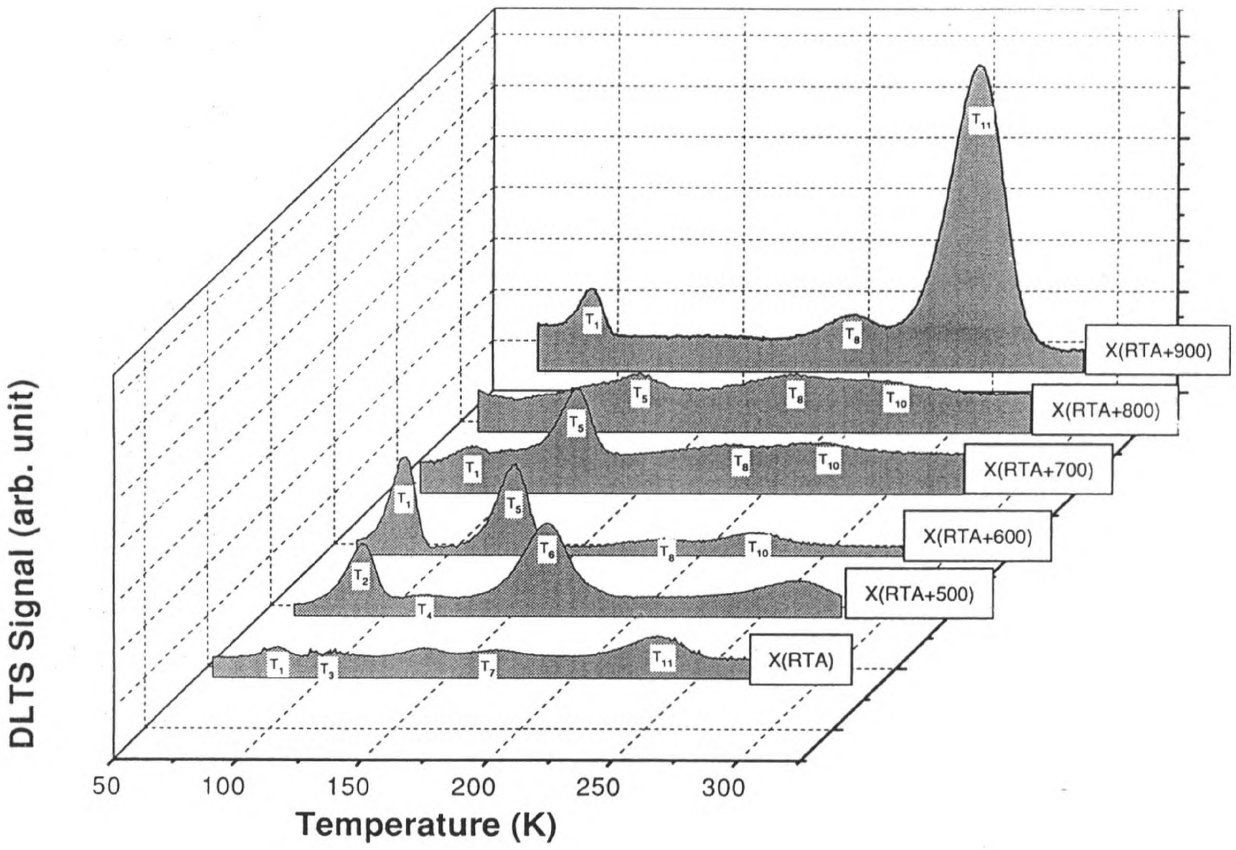

Figure 6.11 DLTS spectra from samples of manufacture X: X(RTA), X(RTA+500), X(RTA+600), X(RTA+700), X(RTA+800), X(RTA+900). DLTS measurements were carried out at $V_{Reverse}$= -6 volts, $V_{Forward}$= 0 volt, forward bias filling time T_{fill}= 8ms. All the DLTS spectra are plotted at rate window 20/s.

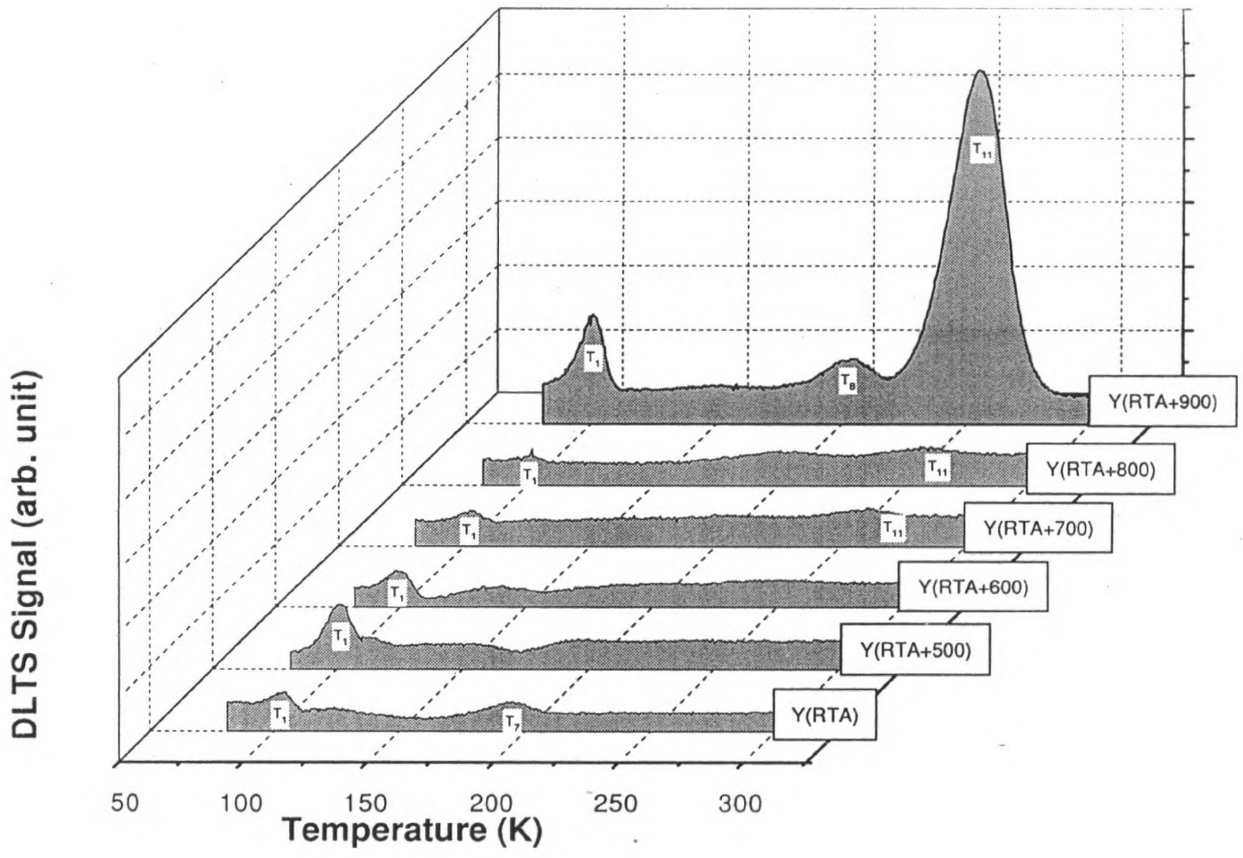

Figure 6.12 DLTS spectra from samples of manufacture Y: Y(RTA), Y(RTA+500), Y(RTA+600), Y(RTA+700), Y(RTA+800), Y(RTA+900). DLTS measurements were carried out at $V_{Reverse}$= -6 volts, $V_{Forward}$= 0 volt, forward bias filling time T_{fill}= 8ms. All the DLTS spectra are plotted at rate window 20/s.

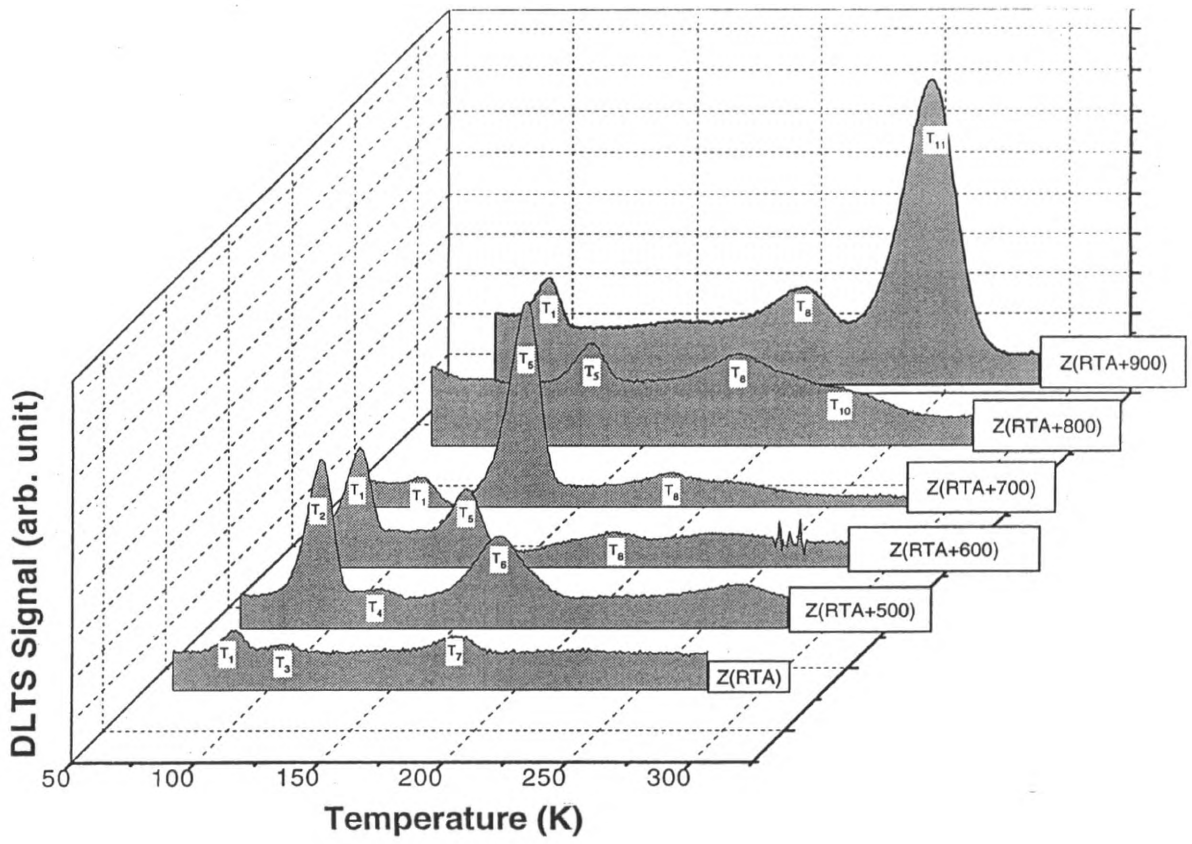

Figure 6.13 DLTS spectra from samples of manufacture Z: Z(RTA), Z(RTA+500), Z(RTA+600), Z(RTA+700), Z(RTA+800), Z(RTA+900). DLTS measurements were carried out at $V_{Reverse}$= -6 volts, $V_{Forward}$= 0 volt, forward bias filling time T_{fill}= 8ms. All the DLTS spectra are plotted at rate window 20/s.

Sample Name	T_1 178 meV	T_2 208 meV	T_3 330 meV	T_4 400 meV	T_5 275 meV	T_6 330 meV	T_7 380 meV	T_8 383 meV	T_{10} /	T_{11} 542 meV
X(RTA)	2.0		1.0				2.0			1.2
X(RTA+500)		5.1		0.2		8.0				
X(RTA+600)	5.0				4.2			1.0	2.0	
X(RTA+700)	0.6				4.0			1.2	1.2	
X(RTA+800)					1.5			1.5	0.1	
X(RTA+900)	3.0							1.7		16.5
Y(RTA)	1.1						0.8			
Y(RTA+500)	2.0									
Y(RTA+600	1.0									
Y(RTA+700)	0.4									0.45
Y(RTA+800)	0.3									0.3
Y(RTA+900)	3							1.8		15
Z(RTA)	1.5		0.53				0.95			
Z(RTA+500)		10		1.0		5.0				
Z(RTA+600)	3.4				2.2			0.8	0.7	
Z(RTA+700)	0.5				6			0.7		
Z(RTA+800)	0.2				1.25			0.75	1.0	
Z(RTA+900)	1.75							1.5		8.75

Table 6.6 Activation Energy (except T_9 and T_{10}) and concentrations (except T_9) of all the deep states detected. The unit of trap concentration is 10^{11} cm^{-3}.

6.3.3 Discussions

Comparing Figures 6.11, 6.12 and 6.13 the features of the DLTS spectra of the X(RTA+900), Y(RTA+900) and Z(RTA+900) samples are identical. The modified MCTS measurements also resulted in identical features of the spectra of these three samples. Our results are consistent with those reported by Mesli and co-workers [Mesli 87] from the study of the so called process-induced defects produced by rapid thermal annealing. For clarity their DLTS and MCTS spectra are shown in Figure 6.14 (a), (b) respectively, together with our own DLTS and MCTS results shown respectively in Figure 6.14 (c) and (d).

The deep level state at the highest temperature in the DLTS plectrum of Figure 6.14 (a) represented the process-induced defect in Mesli's work. The process-induced defect is a commonly observed defect which is believed to constitute the basic structure of a group of five chemical impurities (Au, Co, Ag, Rh, S) which has thermal emission properties indistinguishable from each other [Lang 79]. They all characterized by the midgap deep level which is the same as from the "gold" acceptor (section 6.2.2) level. Their thermal diffusion in silicon is controlled by a large complex of vacancies generated during the heat treatment, which also control the transition from the mobile interstitial site to the final state. This final state would be characterized by thermal emission properties fitted to the complex of vacancies and would be independent of the chemical impurities. This character was reflected in our results and strongly supported that our T_{11} trap was the process-induced defect.

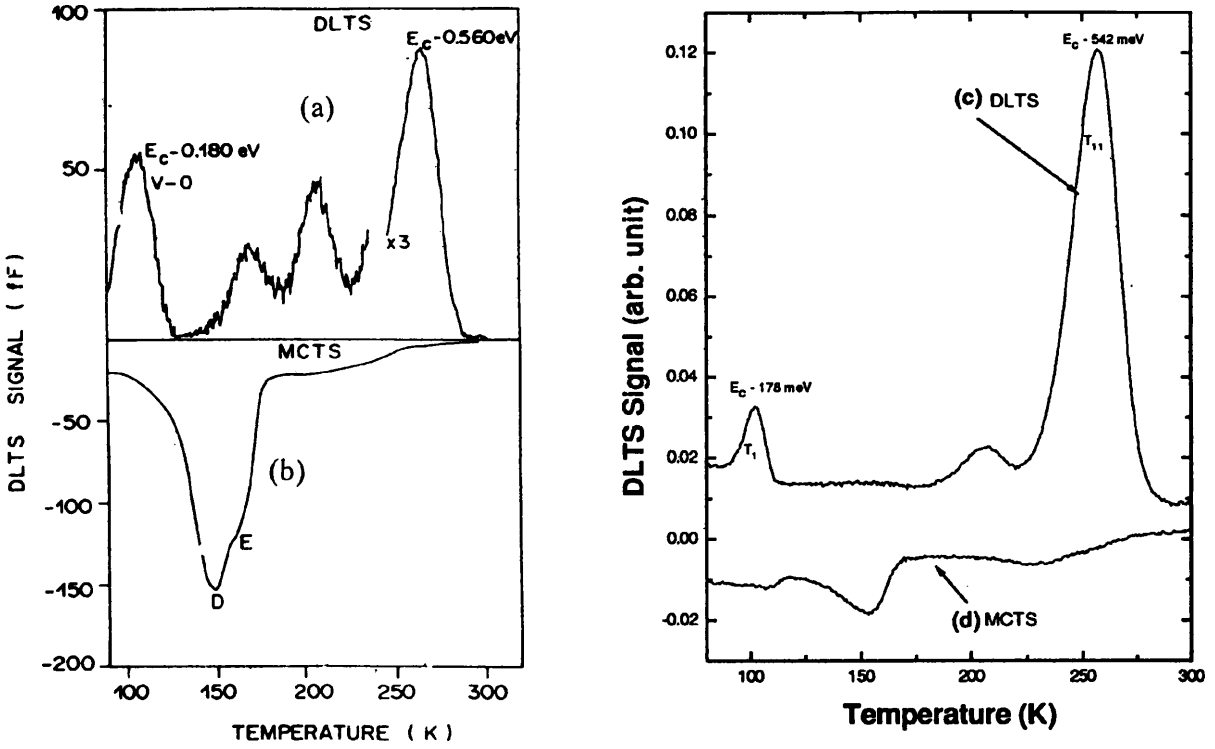

Figure 6.14 Comparison of the process-induced defect from literature with our T_{11} trap in samples rapid thermal annealed followed by a furnace anneal at 900°C and a rapid thermal quenching.
(a) DLTS and (b) MCTS spectra of process-induced defect state reported in the literature, *after Mesli [Mesli 87].*
(c) DLTS and (d) MCTS spectra from our sample X(RTA+900).

The difference between the ratio of the amplitude of the process-induced defect to that of the oxygen-vacancy (V-O) center in Mesli's work in Figure 6.14 (a) and the ratio of T_{11} to T_1 (which was identical to the V-O center) in our spectrum in Figure 6.14 (c) is caused by the fact that they used CZ materials which had a much high oxygen content than our FZ based materials. Actually they observed a reduction in the concentration of the V-O center

when they used the FZ material instead of the CZ material.

Intrinsic impurities like oxygen not only influenced the relative concentrations of some defects but also played a important role in the stability of the process-induced defect. It had been shown that at high temperatures ($\geq$1000°C) in materials containing large concentrations of oxygen ($\geq 10^{17}$ cm^{-3}), there was a increase in the concentration of the V-O centers as the temperature increased, accompanied was a decrease in the concentration of the process-induced defect. This was because the vacancies were trapped by the oxygen atoms and the V-O centers were more stable than the process-induced defects which were also vacancy complexes [Mesli 87]. Therefore there should be a higher stability of the process-induced defect in FZ materials which implies that it would be more difficult to get rid of them.

The interaction between the process-induced defects and the gold and/or transition elements further complicated the situation as was pointed out by Wu [Wu 82] that the concentration and properties of the process-induced defects were themselves modified by the presence of gold and transition elements. More importantly, on the other hand, impurities like Au, Ag, Co, Rh and S might be "driven" by the process-induced defects [Lang 80]. Therefore the more stable the process-induced defects in the material the higher the probability that the serious contamination by impurities might result. The "gold" acceptor level that we found in the GTO thyristor materials (section 6.2.2) was probably resulted from the existence of both the process-induced defects and the gold impurities. In devices that lack of either of these two elements they may escape serious degradation.

Another trap of major concern was T_5 (Figures 6.11 and 6.13). It was identical to the trap T_{L2} in section 6.2.1 which was suggested to be responsible for killing the lifetime in the thyristor materials. The concentration of T_5 was two orders of magnitude smaller than that of trap T_{L2}. The concentration of T_5 as a function of the furnace annealing temperature was plotted in Figure 6.15. This trap was not detected in samples from manufacture Y. As has been mentioned previously in section 6.2.1 this deep level had a similar thermal emission characteristics to one of the quenched-in donors first reported by Yau and believed to be some kind of vacancy complex [Yau 74]. Often its generation was related to processes which produced vacancies such as rapid thermal treatments [Barbolla 76][Paxman 80][Di Marco 89]. And often its existence was related to lifetime problems as was discussed in section 6.2.1. It should be noticed that this deep level was present in the NTD materials (from manufacture X but not Y) as well as in FZ materials (from manufacture Z) in our study. This result suggested it was not unique in NTD materials, i.e. it was not caused by neutron transmutation doping method. It was probably more sensitive to the inherent defects caused by the crystal growth process.

The complicated nature of the defect T_5 made it hard to predict when it would appear and affect the recombination lifetime of the processed materials. Actually the power device production line experienced this unpredictable yield problem as was addressed in section 6.2.1. This could be because some aspects (or some power device materials) of power device processing favoured the conditions of generating them (e.g. more vacancies) more than others.

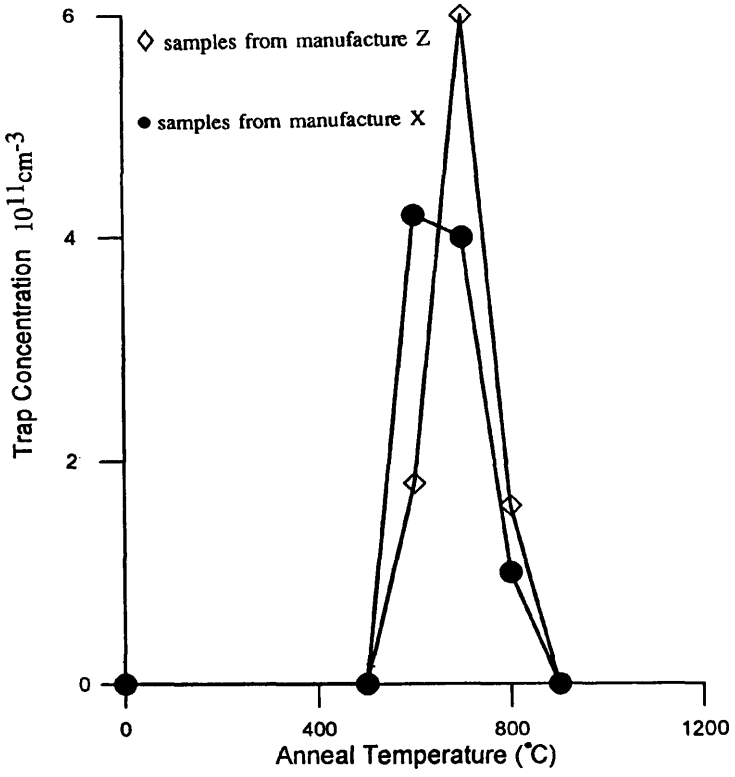

Figure 6.15 The concentration of T_5 in the X and Z series of samples as a function of furnace anneal temperature

Other deep level states observed in the samples listed in Table 6.5 had somewhat complicated origins as reported by Astrova using classical thermal quenching experiments [Astrova 85]. Much more investigation is needed before we can identify them. This is for the future study, since in this work we concentrated on the defects which related to devices degradation.

6.4 Conclusions

Studies of deep states were carried out in two types of power device materials which showed degradation of electrical properties during processing. In the power p-i-n diode materials which had abnormally short lifetimes, four deep level states were detected among which one particular deep level state demonstrated a strong correlation with the lifetime measurements. This deep level was reported in the literature and always there was a lifetime problem related.

In the GTO thyristor materials which had abnormally high leakage currents and short lifetimes, it was found there were "gold"-complex related defects. Extensive studies on the "gold"-complex defects in the literature showed the mid gap "gold" acceptor level acted as a good generation center as well as a good recombination center. This was the reason for the deterioration of the high leakage currents and short lifetimes in the GTO materials in this study.

In order to trace the origin of these deep state defects we have carried out studies in the "as delivered" materials from different manufactures of both NTD and FZ silicon. The following three major points emerged.

(1) The deep level state related to the short lifetime in the power Shockley diode materials was generated in the FZ material and the NTD material (from one of the two NTD manufactures), after rapid thermal annealing followed by a furnace

annealing at some specific temperatures and a subsequent thermal quenching treatment. According to the literature this deep level was some kind of vacancy complex and our thermal dynamic study supported this suggestion.

(2) The complication that: (a) the deep state (discussed in (1)) was present in the FZ material as well as in the NTD materials from manufacture X but not Y, (b) it only appeared in materials after certain thermal treatments, made the appearance of this deep state hard to predict. It seemed more likely that the deep level defects were inherent in the "as delivered" silicon and "activated' by defect reactions during thermal treatments than impurities introduced as a result of the production processes. This could explain the unpredictable behavior in affecting the device's electrical properties.

(3) The "as delivered" materia study revealed a commonly observed so called process-induced defect in all the materials irrespective of the types and manufactures after rapid thermal annealing followed by a furnace annealing at 900°C and a subsequent quenching treatment. This process-induced defect was known to be the basic structure of five impurity (Au, Ag, Co, Rh and S) related complex defect systems. They are all characterized by identical thermal emission characteristics fitted to the complex of vacancies and would be independent of the chemical impurities.

(4) The existence of this process-induced defect in the power device materials would tremendously increased the probability of forming the "gold"-complex (if gold was

already there). Because it could control the diffusion of the impurities like Au, Ag, Co, Rh and S. This character might have played an important role in the incorporation of the "gold"-complexes into GTO device materials (as was discovered in the GTO device) in addition to the prerequisite that the impurity was present.

References

[Ammon 92] von Ammon W. *Nucl. Inst. and Meth. in Physics Research, B63,* 1992, pp 95

[Astrova 85] Astrova E. V., Voronkov V. B., Lebedow A. A. and Urunbaev B. M., *Sov. Phys. Semicond., 19,* 1985, pp 1051

[Barbolla 76] Barbolla J., Bailon L., Brabant J. C., Pugnet M. and Brousseau M., *Revue de Physique Applique 11,* 1976, pp 403

[Bertolotti 68] Bertolotti M., in *Radiation Effects in Semiconductors*, ed. Vook F. L., Proceedings of 1967 Santa Fe Conference on Radiation Effects in Semiconductors (Plenum Press, New York), 1968, pp 311

[Gibson 56] Gibson A. F., Proc. Phys. Soc. B 69, 1956, pp 488

[Grivickas 92] Grivickas V., *Solid State Electronics, vol 35, no. 3,* 1992, pp 299

[Herzer 77] Herzer H., *Semiconductor Silicon,* 1977, pp106

[Indusekhar 86] Indusekhar H., Kumar V. and Sengupta D., *Phys. stat. sol. (a), 93,* 1986, pp 645

[Jayant 79] Jayant Baliga B. and Evwaraye A. O., *Proc. 2nd Int. Conf. Neutron Transmutation Doping,* Ed. Messe J.M.(Plenum Press), 1979, pp 317

[Kern 70] Kern W. and Puotinen, *RCA Rev. 31,* 1970, pp187

[Lang 80] Lang D. V., Grimmeiss H. G., Meijer E. and Jaros M., *Phys. Rev., B22,* 1980, pp 3917

[Maekawa 88] Maekawa T., Inoue S., Aiura M. and Usami A., *Semicond. Sci. Technol.,* 3, 1988, pp 77

[Mesli 87] Mesli A., Courcelle E., Zundel T. and Siffert P., *Physical Review B, 36,* 1987, pp 8049

[Paxman 79] Paxman D. H. and Whight K. R., *Solid State Electronics, 23,* 1979, pp 129

[Sah 70] Sah C. T., Forbes L., Rosier L. L. and Tasch S. F., Jr. Solid-St. Electron., 13, 1970, pp 759

[Schnoller 74] Schnoller M. S., *IEEE Trans. Electron. Devices ED-21*, 1974 pp 313

[Stone 81] Stone B. D., in *Impurity Doping*, ed. Wang FFY, North Holland, 1981, pp 217

[Waldmeyer 88] Waldmeyer J., *J. Appl. Phys.*, 63, 1988, pp1977

[Wu 82] Wu R. H. and Peaker A. R., *Solid State Electron, 25*, 1982, pp 64

Chapter 7 Conclusions and Suggestions for Future Work

7.1 Conclusions

In this thesis defects introduced as a result of silicon processing have been characterized and their formation and evolution mechanisms investigated.

Deep level states with activation energies of electron emission of 440 meV and 506 meV were found to be responsible for causing the excess free carrier concentrations and the high reverse leakage currents in Ge^+ preamorphized and isochronal annealed n-type silicon (CVD epitaxy Si on CZ substrate). A temperature in excess of 800°C was found to be necessary for the recovery of the quality of the materials in terms of their electrical and optical properties. The initial oxygen concentrations was an important influence on concentration of extended defects as determined from the D1/D2 photoluminescence lines in the Ge^+ preamorphized and rapid thermal annealed Czochralski (CZ) p-type silicon samples. However the overall behavior was complicated and involved other impurities such as carbon.

In the case of SiGe alloys formed by implanting high doses of Ge^+, defects introduced to relief the strain accumulated in the $Si/Si_{1-x}Ge_x/Si$ heterostructures were characterized. We have contrasted the effects of either a carbon co-implant or a silicon post-amorphization

implant in addition to the Ge^+ implant. There were no misfit dislocations apart form the EOR defects in the carbon co-implanted material. This was due to the dual roles the carbon played (a) in compensating the strain caused by the Ge atoms and (b) acting as a sink for the radiation damage related defects. We have also examined the effect of a deep Si post-amorphisation which moved the EOR defects deeper into the substrate so that they were remote from the alloy region. We found in this case that the density and extent of the defects were much reduced compared to that from the sample implanted only with Ge^+. We can explain this effect using a model involving homogenous/inhomogeneous alloy growth. Plus the fact that a reduction of nucleation centers for the strain relief defects in the alloy region resulted from this process.

In the study on process induced defects in power devices deep level states with activation energy of electron emission of 275 meV and 542 meV were detected and correlated to the abnormal short lifetimes in power p-i-n diode materials and high reverse leakage currents/short lifetimes in GTO thyristor materials respectively. The origin of them was investigated through the study of the "as delivered" materials after heat treatment. This simulated some aspects of power device processing in a clean environment. The first deep state could be directly produced by thermal treatments simulating specific process steps. The second deep state ("gold"-complex defect) could not be directly generated from the "as delivered" materials. However another deep state emerged which was known to be the basic structure of five impurity defect systems including the "gold"-complex defect which in turn would introduce the "gold"- like acceptor deep level.

7.2 Suggestions for Future Work

Direct observation of the structural evolution of the defects in Ge^+ preamorphized and isochronal annealed n-type silicon (CVD epitaxy Si on CZ substrate) should be made with TEM as a supplement to the present investigation. In this way we can monitor the evolution of the EOR defects and support (or eliminate) our speculation that the deep level defects with electron emission activation energies of 440 meV and 506 meV in the present study are related to EOR defects or defect complexes. Also in the future the samples should have a higher doping concentration ($> 10^{16}$ cm^{-3}) to overcome the limitation on the shallowest depth detected by the electrical measurements so that we can monitor the whole regrowth region. This would also resolve the other limitation namely that the defect concentration should be not more than 10% of the shallow doping level to obtain an accurate amplitude reading of the DLTS signal. On the basis of this can we then pursue the capture cross section measurements of the deep states. To separate the deep states with the electron emission activation energies of 440 meV and 506 meV is important but very difficult under the present circumstances using the conventional DLTS facility. Laplace DLTS [Dobaczewski 94] is considered a suitable technique for this purpose and should be used in the future. Regarding the optical characteristics in these samples further PL studies should be carried out and a better condition should be established to produce well resolved PL lines (not superimposed on the broad bands).

For the study concerning the influence of the initial oxygen content on the residual defects in Ge^+ preamorphized and rapid thermal annealed Czochralski (CZ) grown p-type silicon,

it is essential to use materials with a higher shallow doping concentrations (for example to dope the p-type materials with ion-implantation technique) to overcome the limitation of the shallowest depth measurable by electrical techniques. The positron annihilation technique is suggested to be applied in the future to study the state of oxygen atoms because oxygen clusters with several oxygen atoms are difficult by transmission electron microscopy or Infrared tomography techniques [Ikari 95]. The other point to make is that carbon is also a very important inherent impurity since it affects the defects either directly or via the influence on the oxygen related defects. Therefore it would be very useful to have a parallel study on the influence of the initial carbon concentrations as a complement to the oxygen content study. It is also recommended to use both n and p type materials from the same growth conditions for future study. In summary a much wider range of samples need to be investigated systematically.

Further analysis of the characteristics of the strain relieving defects in $Si/Si_{1-x}Ge_x/Si$ heterostructures formed by high dose Ge^+ implantation should be carried out using High Resolution TEM technique. This is because in addition to the effect of strain accumulation in the alloy layers the characteristics of these defects plays an important role in defect introduction and hence layer relaxation. We should also explore an implant condition that would combine the advantages brought by a carbon co-implant and silicon postamorphisation.

For power device material study, in order to confirm the speculation made in the conclusion section that the process-induced defects would enhance the probability of forming the

"gold" like acceptor level, gold impurity should be deliberately introduced into two heat treated "as delivered" power device materials one has got the process-induced defects in them and the other has not, after which, DLTS measurements should be carried out on both samples to find out if the "gold" acceptor levels are produced or not. Though the deep state with an electron emission activation energy of 275 meV correlated well with the measured lifetime values and was suggested to be the lifetime killer in those materials, numerical modeling of the resultant lifetime requires the knowledge of the minority carrier capture cross section. This could be done with MCTS technique which has been described in chapter 3.

References

[Ikari 95] Ikari A., *Appl. Surf. Sci., 85,* 1995, pp 253

[Dobaczewski 94] Dobaczewski L., Kaczor P., Hawkins I. D. and Peaker A. R., *J. Appl. Phys., 76 (1)*, 1994, pp 194